Characterization of Amorphous Silicon (a-Si) and Silicon Rich Silicon Oxide (SiO_x) Materials Produced by ECR-PECVD

Characterization of Amorphous Silicon (a-Si) and Silicon Rich Silicon Oxide (SiO_x) Materials Produced by ECR-PECVD

by

TYLER RICHARD ROSCHUK

B.Sc. (University of Saskatchewan) 2002

A Thesis
Submitted to the School of Graduate Studies
in Partial Fulfilment of the Requirements
for the Degree
Master of Applied Science

McMaster University

MASTER OF APPLIED SCIENCE (2005) McMaster University
(Engineering Physics) Hamilton, Ontario

TITLE: Characterization of Amorphous Silicon (*a*-Si) and Silicon Rich Silicon Oxide (SiO_X) Materials Produced by ECR-PECVD

AUTHOR: Tyler Richard Roschuk

SUPERVISOR: Dr. P. Mascher

NUMBER OF PAGES: xi, 120

Abstract

Silicon based materials, including silicon oxides and silicon oxynitrides, have found use in a number of areas in photonics including waveguides, antireflection and highly reflective coatings for laser facets, and detectors. For effective use of these materials in photonics it is necessary to characterize their optical properties as a function of their composition and structure. Since these characteristics are often dependent on the method used to deposit the films it is necessary to also determine the effect of deposition type and conditions on the film's properties.

Recently, silicon based materials have been seen to display luminescence due to quantum confinement effects when nanocrystals are formed. This opens up the possibility of a silicon based emitter, something that has not had previous success due to the indirect bandgap of bulk silicon. The development of a silicon based emitter in turn would open up the possibility for monolithically integrated photonic circuits that could take advantage of CMOS processing technology.

This thesis presents the results of research into the characterization of amorphous silicon and silicon oxide thin films deposited by electron cyclotron resonance plasma enhanced chemical vapor deposition. Optical properties of the films have been determined through the use of ellipsometry and correlated with the results from compositional analysis, done using Rutherford backscattering and elastic recoil detection, and bonding structure analysis, done using Fourier transform infrared spectroscopy. Nanocrystals were formed within the films by subjecting them to post-deposition thermal annealing, which induces a phase separation in silicon rich silicon oxide films. The effects of different annealing conditions on composition, structure and optical properties have also been analyzed. Finally, photoluminescence experiments were conducted on the films and correlated with the results from other characterization techniques.

Acknowledgements

I would like to begin by thanking my supervisor, Peter Mascher for providing me the opportunity to pursue this project. Not only have his guidance and knowledge been invaluable to this project, but his friendship and encouragement made my work that much more enjoyable.

Special thanks goes to Jacek Wojcik. His help and guidance have been fundamental to this project at all its stages. I am immensely grateful for all the things he has taught me and for the hours of discussion and direction he has provided me. I must also thank him for all his work in relation to the ellipsometric modeling of these films, which are a major part of the research presented in this thesis.

Thanks also to Mike Flynn, who has readily offered his advice and expertise and helped in my understanding of many aspects of this research. Since joining our group he also certainly made the office a more interesting and enjoyable environment.

Thanks to Andy Knights, who was always willing to offer his expertise in the field of silicon photonics.

Thank you to the other researchers whose help and guidance made this work possible. J. A. Davies from McMaster University and W. N. Lennard from the University of Western Ontario, for their help in obtaining and analyzing the ion beam experiment data. Othman Zalloum for all his valuable assistance in obtaining and interpreting the photoluminescence spectra. David Comedi for his ideas, advice, and the x-ray diffraction work he has done. Andy Duft and Fred Pearson for their help in obtaining the AFM and TEM images. Edward Irving and Xiaonan Tan, fellow researchers/grad students with whom I co-worked on various aspects related to this research project. All the summer students who helped with various parts of this project; Jonathan Stolle and Shyemaa Shehata, who helped set up the FTIR system and performed some initial FTIR measurements and analysis; Matt Farrar, who helped out with a number of annealing experiments and analysis; and Karleen Dudeck for her help with

the annealing experiments and TEM sample preparation.

My heartfelt thanks to my family. My wife, Roxanne, for her support and encouragement and for following me here from Saskatchewan while I pursued this research. My parents, Richard and Myra, and my brother, Travis, for the love and support they have provided me in all of my endeavors.

I would also like to thank McMaster University, particularly the Department of Engineering Physics and the School of Graduate Studies for allowing me to perform my research here and for their financial support.

Finally, I would like to thank the following organizations who generously provided the funding to make this research possible: The Natural Sciences and Engineering Research Council of Canada (NSERC), The Canadian Institute for Photonic Innovations (CIPI), and the Ontario Research and Development Challenge Fund (ORDCF, contract number 01-Mar-0927 under the Ontario Photonics Consortium (OPC)).

Contents

List of Figures

List of Tables

Chapter 1

Introduction

Silicon-based materials are found in numerous areas in the fields of electronics and photonics. In fact, silicon has long been the dominant material in microelectronics due to its high integrability, making it ideal for VLSI (Very Large Scale Integration) and ULSI (Ultra Large Scale Integration) circuits [1,2]. Dielectric silicon-based materials such as silicon oxides and silicon oxynitrides have also found applications in electronics as gate materials for transistors [3].

The photonics industry, however, has seen no one dominating, multipurpose material, preventing monolithic integration of photonic circuits. The indirect bandgap of silicon has caused it to be largely disregarded as a suitable candidate for implementation of a light emitter, a role largely reserved for III-V compounds such as GaAs. Combining silicon based photonic circuitry with III-V emission devices in hybrid integration schemes is, however, a costly and complex procedure [4]. This in turn poses a problem not only for photonics, but also for future generation electronics. As feature sizes continue to decrease interconnect delays begin to play a substantial role in speed reduction of ULSI circuits. Optical interconnects are currently one of the proposed solutions to this problem. In order to have functional optical interconnects some form of integrated emitter must exist. Because CMOS technology deals predominantly with silicon, a silicon based emitter would be the ideal solution. In fact the International Technology Roadmap for Semiconductors calls specifically for a CMOS compatible emitter, which must be implemented in Si [5].

In 1990 *L. Canham* observed luminescence from silicon films that he had subjected to an anodic etch [6]. The results were attributed to the formation of nanocrystals and nanowires as the film became porous, causing quantum confinement effects which produce results very different from those of bulk silicon. More recently luminescence from silicon nanocrystals formed within silicon oxide materials has been observed. The research group of *L. Pavesi* has been able to demonstrate optical gain from these structures [7]. Results such as these have made silicon-based light emitters a real possibility within the near future and have spurred research into the area by numerous groups across the globe.

While silicon-based light sources are certainly an interesting topic they are not the only potential application of silicon based materials in photonics, and these materials are hardly foreign to the photonics industry. Silicon oxides and silicon oxynitride thin films often find applications as highly reflective and anti-reflection coatings for laser facets [8]. For applications such as these the optical constants, index of refraction and extinction coefficient, become important parameters. In order to achieve the desired performance over a given wavelength range the optical constants and thicknesses of multiple layers must be carefully designed. To do so, however, one must know the optical constants for a given composition of the material, which in turn requires one to know the resulting composition for a given set of deposition parameters. It is also necessary to analyze the effects of post-deposition treatment on the material in order to know if the composition or structure are modified.

In addition to optical coatings silicon oxide and oxynitride materials have also found use in waveguides, detectors, modulators, and as a dielectric capping material to induce bandgap shifting in III-V quantum well laser structures [9–13]. An introduction to silicon photonics, covering the implementation of some of these devices, may be found in [14].

In this thesis properties of Electron Cyclotron Resonance Plasma Enhanced Chemical Vapor Deposition (ECR-PECVD) grown silicon-based thin films, with compositions from a-Si to SiO_2, will be discussed. The films have been grown through the use of silane, oxygen, and argon gas mixtures. The ECR-PECVD system and the deposition chemistries for these films are discussed in Chapter 2. After deposition, the films

were subjected to high temperature thermal anneals in order to analyze their effects on variations in the film composition, bonding structure, and optical properties, as well as to induce nanocrystal formation for luminescence studies.

Chapter 3 reviews some of the basic properties of silicon-based materials for their use in photonic applications. The formation of silicon nanocrystals and their properties are briefly discussed. Details of quantum confinement, as it relates to Si-nanocrystals, and its role in producing luminescent silicon are also presented.

Compositional information for these films has been obtained through the use of ion beam analysis techniques, such as Rutherford backscattering spectrometry (RBS) and elastic recoil detection analysis (ERD), which are capable of giving absolute values of atomic constituents within a film. RBS is done through analysis of backscattered high energy ions incident on a thin film-substrate sample. The backscattering is caused by elastic collisions between the ions and atoms within the film, with the energy of the backscattered ion being indicative of the mass of the atom with which it has collided. ERD was used to analyze the effects of annealing on the hydrogen content of the films. ERD is similar to RBS, however, rather than detecting backscattered ions, atoms that have undergone forward recoil after the collision are detected. The composition of the films was then related to the deposition parameters used for their growth. Details of the ion beam analysis techniques are discussed in Chapter 4.

Fourier transform infrared (FTIR) spectroscopy was used to obtain information about the bond structure within the films. Atomic bonds exhibit characteristic absorption peaks due to the resonant absorption of IR light. The position, structure, and intensity of the peaks are indicative of the bond type, structure, and quantity. Because SiO_2 has prominent absorption peaks that have been well characterized in the literature FTIR spectroscopy serves as a valuable tool to analyze modifications of the oxide structure in these films as they are annealed. Chapter 5 reviews the theory of FTIR spectroscopy and its use for characterization of film bonding structures.

Optical characterization of the thin film materials was done through ellipsometry and photoluminescence (PL) experiments. If light of a specific, known, polarization is incident on the surface of the film, analysis of the change in polarization upon reflection at the surface and at interfaces between film layers yields information on

the optical constants, refractive index and extinction coefficient, and thickness of the film. This forms the basis for ellipsometry. Perhaps the most important aspect of ellipsometry is the modeling of the results, for which is necessary to carefully design models that properly account for the film structure, in order to correctly determine the optical constants of the film from the measured ellipsometric values. The details of ellipsometry are discussed in Chapter 6.

Photoluminescent (PL) experiments are of great importance when characterizing semiconductor devices, especially those being explored for photonic emission device applications. The process is quite simple. Light with sufficient energy to excite an electron from the valence to the conduction band is incident on the sample. When the electron decays back to the valence band and recombines with a hole, the radiative emission is indicative of the electronic band structure of the film, provided the recombination is radiative. As mentioned, typically, the PL efficiency of silicon is quite poor due to its indirect bandgap, which decreases the probability of radiative emission. Quantum confinement in silicon nanocrystals, however, allows for a more efficient PL process. Luminescence and the general details of quantum confinement are also discussed in Chapter 6.

Experimental procedures and details are presented in Chapter 7, while results and discussion from the characterization of these films are presented in Chapter 8. The optical and photoluminescent properties of the films are discussed in relation to their composition and structure. In order to illustrate some of the features related to structure atomic force microscopy (AFM) and electron microscopy images are presented. Details of the microscopy methods are, however, not discussed.

Finally, conclusions and suggestions for future work are presented in Chapters 9 and 10, respectively.

Chapter 2

Silicon-based Thin Film Deposition by Electron Cyclotron Resonance Plasma Enhanced Chemical Vapor Deposition

The films discussed within this thesis were deposited through the use of electron cyclotron resonance plasma enhanced chemical vapor deposition (ECR-PECVD). ECR-PECVD allows for the deposition of dielectric thin films having a wide range of compositions, including silicon oxides with compositions from amorphous silicon (*a*-Si) to silicon dioxide (SiO_2), which are the focus of the research presented here, as well as silicon oxynitrides with compositions from silicon dioxide to silicon nitride (Si_3N_4) [15].

The advantage of using ECR-PECVD is not only that a wide range of compositions can be deposited accurately, but also that the system allows for deposition at low temperatures with good control of thickness and uniformity. Because these films find applications in a wide range of areas; including highly reflective and anti-reflective optical coatings, waveguides, passivation films, and isolation layers; control of these parameters becomes important to the overall device performance [3, 16–18].

In this chapter, the ECR-PECVD system is introduced and the deposition chemistries

and details related to film growth are discussed. Additionally, the effects of post-deposition thermal annealing of the films are discussed.

2.1 The ECR-PECVD System

ECR-PECVD functions by using ions extracted from a plasma region in order to crack a precursor gas and produce desired chemically active species, that then react via conventional pathways, for deposition onto a given substrate. Figure 2.1 shows a schematic of the ECR-PECVD system [19].

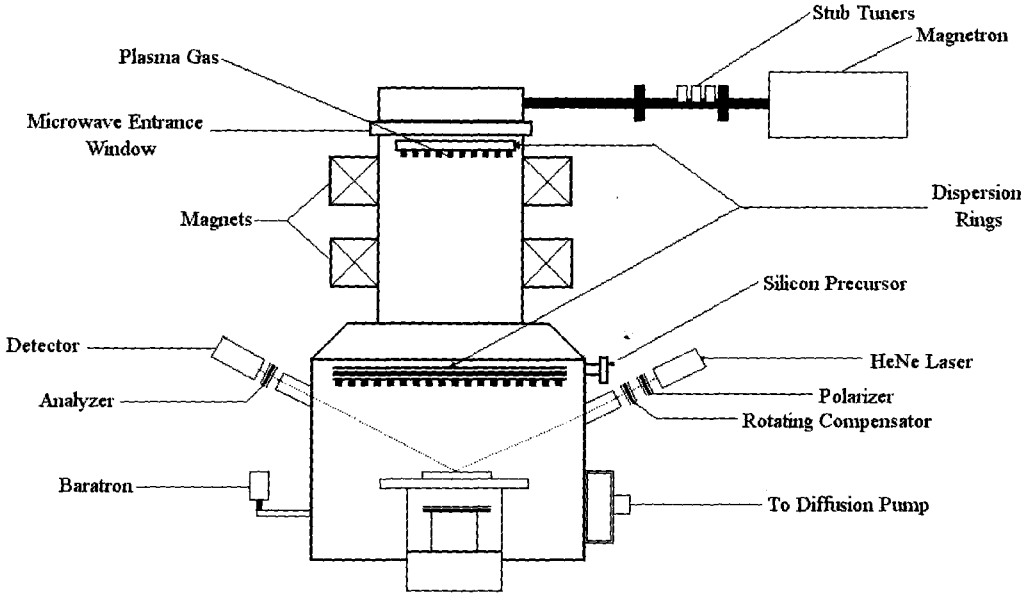

Figure 2.1: A Schematic of the ECR-PECVD System.

The plasma gases (O_2, N_2, and Ar) are introduced through the upper dispersion ring. A high frequency electric field is produced by the magnetron head and is applied across the body of the gases in order to generate the plasma. The stub tuners allow for impedance matching of the load to the microwave source in order to minimize reflected power, thus increasing the amount of power delivered to the chamber. While the magnetron source is capable of generating upwards of 1200 W of power the system

was set to produce approximately 500 W of power with a reflected power of 5 W for the depositions done here [16].

Electrons in the plasma gas are excited by the resonant absorption of the microwave energy. In order for this absorption of energy to occur a strong magnetic field, which satisfies the cyclotron resonance condition, is needed. The cyclotron resonance condition is given by:

$$\omega_c = eB/m_e \tag{2.1}$$

where ω_c is the cyclotron resonance frequency, the characteristic frequency of oscillation of the electron in a magnetic field of strength B. e and m_e are electron charge and mass, respectively. In order to satisfy the resonance condition of Equation 2.1 for a microwave frequency of 2.45 GHz, a magnetic field of 875 Gauss must be established below the microwave entrance window. This field is applied through the use of the two magnets shown in Figure 2.1 [19].

By satisfying the conditions above, an ECR region is established and the electrons experience a Lorentz force:

$$\vec{F} = q\vec{v} \times \vec{B} \tag{2.2}$$

due to the magnetic field causing the electrons to undergo a circular motion, with angular frequency ω_c, as they travel downward, producing a helical path. As the electron gains energy the radius of this path increases, thus increasing the probability of collisions between the electron and molecules within the source gas [16].

Initially only a few free electrons exist within the plasma region and the kinetic energy from the electric field is coupled entirely into them. As they gain energy, the electrons become capable of dissociating and ionizing the molecules within the source gas. This in turn produces secondary electrons that undergo the same procedure and a plasma discharge is sustained [16, 20].

The current to the upper and lower magnets for the system are set to 180 and 115 A, respectively. In addition to satisfying the cyclotron resonance condition this setup also provides control over the flow of charged particles from the ECR zone by creating a 'mirror' magnetic field distribution. This distribution favors the release of

low energy ions while high energy ions and electrons are reflected back into the ECR zone. This is advantageous as it decreases the amount of surface damage that could occur due to high energy ions impacting on the substrate or the film [16, 21].

The silicon precursor used, silane (SiH_4), is introduced through the lower dispersion ring below the plasma generation region. Ions leaving the plasma generation region collide with the silane molecules causing the molecules to disassociate and produce various radical species which then react with the plasma ions at the sample surface, causing film growth to occur. The deposition chemistry underlying these reactions is discussed in more detail in sections 2.2.1 and 2.2.2. The composition of the film is controlled by the amount of any given atomic species present in the chamber, which is in turn controlled by the gas flow of that species into the chamber.

In order to ensure uniformity of the films the silane gas dispersion ring has been carefully designed such that a flux discrepancy does not exist between the points closest to and farthest from the injection duct. In addition, film uniformity is improved through the use of a rotating sample stage.

The sample stage is located directly below the silane dispersion ring. A sample holder is mounted onto the stage via a load lock system. The stage may then be heated up to a temperature of 800 °C, although for the depositions discussed in this thesis a much lower temperature, 350 °C, was used. In fact, one of the advantages of ECR-PECVD is that a lower substrate temperature may be used for deposition than for conventional chemical vapor deposition (CVD). CVD requires that high substrate temperatures be used in order to insure that the necessary chemical reactions occur, with the deposition of silicon oxide films requiring a temperature of approximately 450 °C, while the deposition of silicon films can require temperatures in excess of 600 °C, depending on the desired quality of the film [22, 23].

Film growth may be monitored in two ways. The first is through the use of an in-situ rotating compensator ellipsometer. The details of ellipsometry are discussed in Chapter 6. For the films discussed in this thesis, however, the ellipsometer was not in working order during the depositions and growth was monitored using a quartz thickness monitor (not shown), which functions by measuring the change in oscillation frequency of a scintillator crystal as a film is deposited upon it. While the quartz

thickness monitor (QTM) does not yield perfect results due to variations in film densities which aren't accounted for in the QTM program, it does allow for the approximate determination of film thickness during the deposition. The QTM can be reprogrammed to account for these changes, however, more exact thicknesses were later determined ex-situ through ellipsometry and used to determine growth rates for the films.

In order to establish the vacuum environment necessary for thin film growth and to remove waste products produced during the deposition process the chamber is evacuated using a diffusion pump.

2.2 Silicon-based Materials Deposition

In order to explain the deposition chemistry of silicon based materials within a plasma deposition chamber, studies have previously been done which have analyzed the presence of radical and ion species produced within the chamber. In this section some of the underlying chemistry that occurs within the chamber to produce the necessary species for film growth is presented.

2.2.1 Deposition Chemistry of Amorphous Silicon Thin Films

Amorphous silicon thin films grown for this thesis were deposited using argon as the plasma gas and a silane-Ar mixture (10% SiH_4 in Ar). For this reason the growth process is discussed in terms of SiH_4. The discussion can typically be broadened to include other silicon precursors, such as $SiCl_4$ and SiF_4, simply by replacing H with the appropriate element from the precursor. The use of organic precursors such as tri(dimethylamino)silane (TDAS) is slightly more complicated and will not be discussed here. A discussion of film growth using TDAS may be found in [24].

In general the deposition of amorphous silicon can be described by:

$$SiH_4 \rightarrow a\text{-}Si{:}H \tag{2.3}$$

where the incomplete decomposition of the silane precursor and residual hydrogen in the chamber result in the deposition of a hydrogenated a-Si film [25].

The primary reactions leading to the formation of radicals, atoms, and ions which act as active species in a PECVD deposition process are as follows:

$$SiH_4 + e \rightarrow SiH_n + (4-n)H + e \tag{2.4}$$

$$SiH_4 + e \rightarrow SiH_n^+ + (4-n)H + 2e \tag{2.5}$$

$$SiH_4 + e \rightarrow SiH_n^- + (4-n)H \tag{2.6}$$

$$H + SiH_4 \rightarrow SiH_3 + H_2 \tag{2.7}$$

$$SiH_4 + SiH_n \rightarrow Si_2H_{4+n} \tag{2.8}$$

$$SiH_n^+ + SiH_4 \rightarrow Si_2H_m^+ + (4+n-m)H \tag{2.9}$$

where the first three equations, 2.4, 2.5 and 2.6, are the results of electron-molecule reactions, 2.7 and 2.8 are the result of neutral-neutral reactions, and 2.9 is the result of an ion-molecule reaction [25,26]. In addition, energetic Ar atoms, denoted Ar*, react via collisions in order to cause SiH_4 disassociation [22]. Electron impact collisions with Ar atoms in the plasma region can cause the generation of Ar ions and energetic Ar atoms through:

$$Ar + e \rightarrow Ar^+ + 2e \tag{2.10}$$

$$Ar + e \rightarrow Ar^* + e \tag{2.11}$$

The energetic Ar atoms then react with the SiH_4 via the general reactions:

$$Ar^* + SiH_4 \rightarrow SiH_x \tag{2.12}$$

and

$$Ar^* + SiH_4 \rightarrow a\text{-}Si{:}H \tag{2.13}$$

As mentioned, the incomplete dissociation of the silane precursor results in hydrogen contamination of the films. Additionally, residual hydrogen atoms within the chamber are able to incorporate into the films either interstitially or through the passivation of Si bonds. The hydrogen incorporation can be reduced through an increase in the substrate temperature. At higher temperatures there is sufficient thermal energy to break the Si-H bonds and cause the desorption of the H atoms [26, 27]. Previous

studies have also revealed that the deposition chamber exhibits a memory effect with additional hydrogen being incorporated during successive depositions. This memory effect can be reduced through an Ar plasma cleaning of the chamber prior to deposition [19].

In the above discussion only an Ar dilution gas was considered. Alternatively, other gases, such as H_2, He, and other noble gases, are often used in this role. The type of diluting gas used can have a significant effect on the properties and quality of the deposited film, as it may affect the silane dissociation and the ion bombardment of the growing surface [25]. The variation of plasma chemistry and film properties as different diluting gases are used has been studied extensively in the literature using a variety of techniques, including optical absorption and emission spectroscopies (OES and OAS) and quadrupole mass spectroscopy (QMS) [16,21,25,28,29]. Through these techniques, the types and concentrations of radicals within the deposition chamber can be determined. This process may also be used to examine not only the effects of the dilution gas, but also to analyze the effects of the variation of other deposition parameters, such as microwave power and gas flow ratios, on the presence of deposition precursor species.

The use of an Ar dilution gas results in an adverse effect, as some Ar is incorporated into the films during the deposition process. This Ar contamination has been seen to be relatively low compared to the amount of H incorporated into the film and Ar can be removed through thermal annealing. Details of this are discussed as a part of the research done for this thesis.

2.2.2 Deposition Chemistry of Silicon Rich Silicon Oxide Thin Films

As silicon dioxide is certainly the most studied of silicon oxide materials, this section begins with a discussion of silicon dioxide deposition followed by a brief discussion of the deposition of silicon rich silicon oxides (SiO_x, where $x < 2$).

Within the plasma region, oxygen molecules, O_2, are both put into excited states of O_2 and broken into individual oxygen atoms through electron impact collisions and

collisions with Ar atoms and ions [21,22]. The oxygen atoms then travel downstream and react with the SiH_4 molecules through a series of H abstraction and elimination processes:

$$O + SiH_4 \rightarrow SiH_3 + OH \tag{2.14}$$

$$O + SiH_3 \rightarrow SiH_2O + H \tag{2.15}$$

$$OH + SiH_3 \rightarrow SiH_2O + H_2 \tag{2.16}$$

$$O + SiH_2O \rightarrow HSiO + OH \tag{2.17}$$

$$O + HSiO \rightarrow SiO + OH \tag{2.18}$$

$$SiO + O_2 \rightarrow SiO_2 + O \tag{2.19}$$

In addition, the production of H and OH molecules leads to further reactions, producing silylene (SiH_3) molecules,

$$OH + SiH_4 \rightarrow SiH_3 + H_2O \tag{2.20}$$

$$H + SiH_4 \rightarrow SiH_3 + H_2 \tag{2.21}$$

The water produced by the reaction in equation 2.20 is removed from the chamber through careful design of the pumping system, preventing its incorporation into the films [21].

As with the deposition of *a*-Si films, techniques such as OES, OAS and QMS have been used to analyze the presence of the various species present in the chamber to determine their concentrations, and hence, their roles in the deposition process [30,31].

The deposition of silicon rich silicon oxide films is accomplished by a combination of the processes that are used for the deposition of *a*-Si and SiO_2 films. By decreasing the oxygen flow and increasing the argon flow into the chamber, such that the chamber pressure is maintained, there exist less oxygen molecules to undergo the processes that influence SiO_2 deposition, thus Si atoms available for film growth are in excess relative to the O atoms. It is also possible to create an excess of Si atoms by increasing the SiH_4 flow into the chamber, avoiding the need for additional Ar flow. The amount of excess Si and the relative reaction rates of SiO_2 and *a*-Si then determine the composition of the film.

2.2.3 Film Growth

Now that details of the deposition chemistry have been presented, an introduction to the processes involved in thin film growth will be given. Because the primary topic of this work is an analysis of the properties of the deposited films, this treatment will largely be done in a qualitative manner in order to provide a general understanding of the growth process. The reader is referred to the works of Lewis *et al.* [32,33] and Venables *et al.* [34] for a more thorough analysis of the topic.

Atomic species, produced through the chemical reactions outlined above, arrive at the substrate surface at a rate of

$$R = p\left(\frac{1}{2\pi mkT}\right)^{\frac{1}{2}} \qquad [cm^{-2}s^{-1}] \tag{2.22}$$

where p is the gas pressure, m is the molecular mass of the atomic species, k is the Boltzmann constant and T is the temperature (in K) [32]. After arriving at the surface atoms are adsorbed. The atoms may then either be desorbed, or undergo diffusion along the surface followed by chemisorption and nucleation processes. The growth process is completed through nuclei growth to form islands which then coalesce to form a continuous film [35].

In order to drive nucleation, and hence film growth, a high supersaturation, S, of p is required with respect to the vapor pressure of the substrate, p_s. S is therefore defined as [36]:

$$S = \frac{p}{p_s} \tag{2.23}$$

The reason for this will become apparent once the change in the chemical free energy of the system is considered.

For the discussion of thin film growth, consider Figure 2.2 which shows the basic atomic processes that occur during the growth process [23]. In the figure, γ is the interfacial tension between components and the subscripts f, s, and v refer to the film, substrate, and vapor, respectively. θ is the contact angle between the substrate and a growing film nucleus.

The relation between the three tensions is determined by considering the tensions

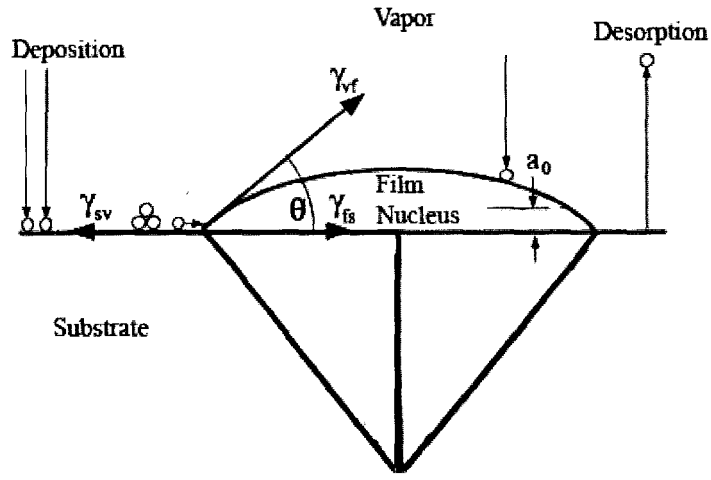

Figure 2.2: Basic atomic processes during vapor deposition [23].

under mechanical equilibrium, which yields Young's equation:

$$\gamma_{sv} = \gamma_{fs} + \gamma_{vf} \cos\theta \tag{2.24}$$

The actual growth of the film can proceed by three different modes: layer by layer (Frank-van der Merwe mode), island (Volmer-Weber mode), and layer plus island (Stranski-Krastanov mode). These processes are illustrated in Figure 2.3 [23]. The type of growth is dependent on the interaction between the substrate and film atoms. During layer by layer growth individual layers grow one atop another. The interaction between substrate and film atoms is greater than between adjacent film atoms. Layer by layer growth is a case where $\theta = 0$ and $\gamma_{sv} \geq \gamma_{fs} + \gamma_{vf}$. Island growth occurs when the interaction between adjacent atoms is greater than that between film and substrate atoms, allowing three dimensional islands to form. During island growth $\theta > 0$ and $\gamma_{sv} < \gamma_{fs} + \gamma_{vf}$. Finally, in layer plus island growth one or two monolayers form on the substrate, after which growth proceeds via island formation. In this case γ_{fs} increases with increased thickness and nuclei are able to form above the layers, causing a change in the growth mode. In addition to the surface tensions the type of growth mode is also controlled by the supersaturation of the system, with larger values of S favoring layer growth [36].

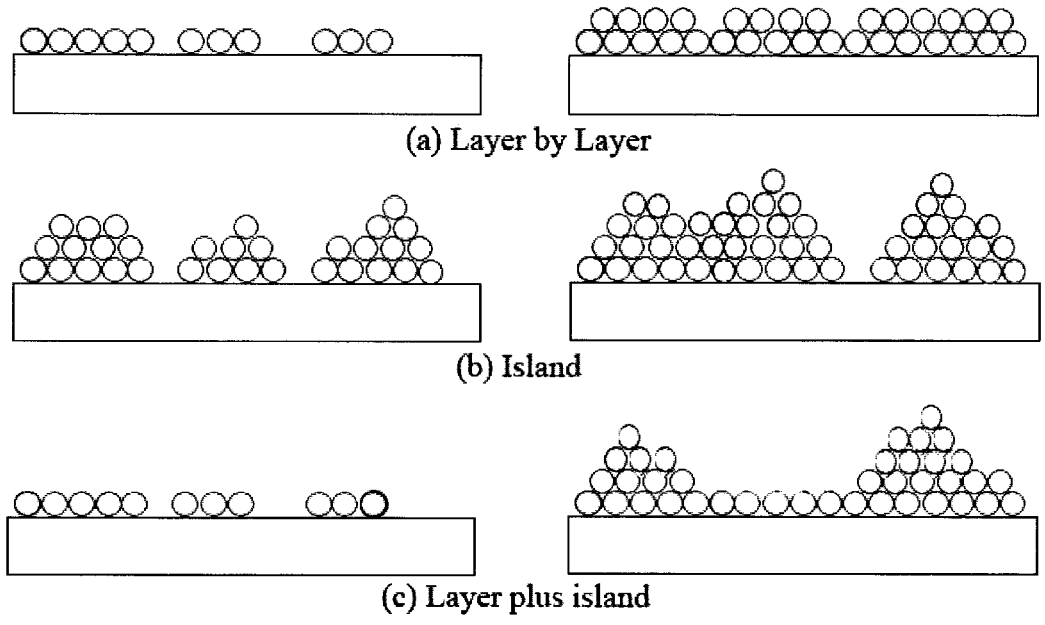

Figure 2.3: Thin film growth models

The process of nucleation involves a decrease in the chemical free energy of the system related to the change in chemical free energy per unit area, ΔG_V:

$$\Delta G_V = -\frac{kT}{\Omega} \ln S \tag{2.25}$$

where Ω is the atomic volume of the nucleus. From this equation one can see why it is necessary to have a supersaturation. If there is no supersaturation then ΔG_V is zero and nucleation can not occur. When a nucleus is formed the total free energy change of the system, for a sphere of radius r, is given by:

$$\Delta G = \frac{4}{3}\pi r^3 \Delta G_V + 4\pi r^2 \gamma \tag{2.26}$$

where the first term is the chemical free energy decrease of the system and the second is the increase in the surface free energy. Here γ represents the surface energy per unit area. By minimizing ΔG with respect to r one obtains a value:

$$r = r^* = \frac{-2\gamma}{\Delta G_V} \tag{2.27}$$

which is the critical radius for a stable nucleus. Initial nuclei form through random processes. If the nucleus has a radius less than that of the critical radius then it will be unstable and will shrink. If the radius of the nucleus is, however, larger than the critical radius then the nucleus will be stable and will continue to grow and contribute to film growth. A more accurate treatment involves factoring in the surface energy contributions of each of the γ components shown in Figure 2.2. In this case one is no longer dealing with a sphere and the proper geometric constants must be considered. Equation 2.26 then becomes:

$$\Delta G = a_3 r^3 \Delta G_V + a_1 r^2 \gamma_{vf} + a_2 r^2 \gamma_{fs} + a_2 r^2 \gamma_{sv} \tag{2.28}$$

The geometric constants are $a_1 = 2\pi(1-\cos\theta)$, $a_2 = \pi \sin^2\theta$, and $a_3 = \pi(2-3\cos\theta+\cos^3\theta)/3$. The critical nuclei radius and free energy change then become

$$r^* = \frac{-2(a_1\gamma_{vf} + a_2\gamma_{fs} - a_s\gamma_{sv})}{3a_3\Delta G_V} \tag{2.29}$$

and

$$\Delta G^* = \frac{4(a_1\gamma_{vf} + a_2\gamma_{fs} - a_s\gamma_{sv})^3}{27a_3^2\Delta G_V^2} = \left(\frac{16\pi\gamma_{vf}^3}{3\Delta G_V^2}\right)\left(\frac{2-3\cos\theta+\cos^3\theta}{4}\right) \tag{2.30}$$

respectively.

In the earliest stages of film formation nuclei are spaced far apart and the rate at which they grow is determined by the rate at which adsorbed atoms, adatoms, attach to them. When atoms arrive at the surface they typically remain there for a mean lifetime, τ_s, before desorption given by:

$$\tau_s = \frac{1}{\upsilon} exp\left(\frac{E_{des}}{kT_s}\right) \tag{2.31}$$

where υ is a vibration frequency of the adatom (typ. $\sim 10^{12}$ sec^{-1}) and E_{des} is the energy required to desorb the atom back into the vapor. Adatoms make random diffusive jumps on the surface during this lifetime and may bond with other adatoms or attach to nuclei on the surface. The value of E_{des} is increased when these atoms attach to nuclei or find areas of the substrate with high binding energies, therefore, desorption becomes less likely. The nucleation rate, $\dot{N}$, is then given as:

$$\dot{N} = N^* A^* \omega \ [nuclei/cm^2 sec] \tag{2.32}$$

where N^* is the equilibrium concentration of stable nuclei and ω is the rate at which vapor atoms impinge onto nuclei of critical area, A^* [23]. N^* is given by

$$N^* = n_s \exp\left(-\frac{\Delta G^*}{kT}\right) \tag{2.33}$$

where n_s is the total nucleation site density. Not all nucleation sites are unoccupied. The number of occupied sites is determined through the product of the adatom lifetime and the atomic arrival rate as

$$n_a = \tau_s p \left(\frac{1}{2\pi m k T}\right)^{\frac{1}{2}} \tag{2.34}$$

The critical area is given by:

$$A^* = 2\pi r^* a_0 \sin\theta \tag{2.35}$$

where a_0 is an atomic dimension. Finally, the impingement rate onto A^* is

$$\omega = \frac{\tau_s p \nu \exp(-E_s/kT)}{(2\pi m k T)^{\frac{1}{2}}} \tag{2.36}$$

where $\nu \exp(-E_s/kT)$ is the frequency of adatom diffusive jumps, and E_s is the activation energy for surface diffusion. The mean distance, X, that atoms can diffuse before desorption is:

$$X = (2D_s\tau_s)^{1/2} \tag{2.37}$$

for a surface diffusion coefficient D_s given by:

$$D_s = \frac{1}{2} a_0^2 \nu \exp(-E_s/kT) \tag{2.38}$$

After some substitution one ends up with the expression

$$\dot{N} = 2\pi r^* a_0 \sin\theta \frac{p}{(2\pi m k T)^{\frac{1}{2}}} n_s \exp\left(\frac{E_{des} - E_s - \Delta G^*}{kT}\right) \tag{2.39}$$

for the nucleation rate [23].

The above treatment of thin film growth is known as capillarity theory. The results from the theory provide a qualitative understanding of the thin film growth process. In order to obtain a more quantitative result atomistic theories must be factored into the process, but will not be considered here, as the goal of this section is only to give a general idea of how film growth proceeds.

The nucleation process eventually reaches a critical point at which no new nuclei sites form and existing sites grow to form islands and then coalesce to form a continuous film. The coalescence process involves a number of mass-transport mechanisms, including Ostwald ripening, sintering, and cluster migration. These processes are illustrated in Figure 2.4. During the coalescence process it is interesting to note that islands behave liquid-like, acting like droplets [23, 37].

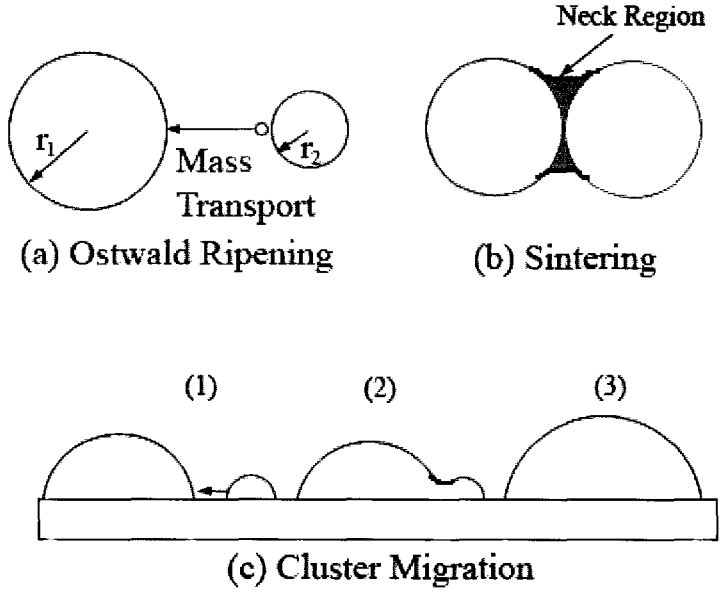

Figure 2.4: Coalescence processes involved in thin film growth.

Consider the case where there are two clusters of differing sizes but within close proximity to one another. Prior to coalescence smaller clusters will migrate and be 'absorbed' by the larger ones, allowing the larger ones to 'ripen' at the expense of the smaller ones, which is the basis of Ostwald ripening. The process serves to minimize the total surface area and hence surface free energy of the system. The actual process involves diffusion of individual adatoms from the smaller cluster to the larger until the smaller one disappears.

When two islands are in contact with each other they may undergo sintering, during which adatoms from the two islands diffuse into the region where the two

islands touch, forming a neck region. As time progresses this neck region between the two islands widens and a single island results.

Finally, clusters of atoms on the substrate surface may migrate along the surface, as shown in Figure 2.4(c1). Coalescence can occur when there is a collision between two clusters or a cluster and an island (c2), resulting in a single island (c3).

The final structure of the film is determined through a number of factors. The most important of these factors are (i)the nucleation rate, (ii)the substrate temperature, and (iii) the deposition rate.

(i)Nucleation Rate. When there is a high nucleation rate then there are many nucleation sites. This causes fine-grained or even amorphous structures to form. Low nucleation rates on the other hand, are favorable for single crystal growth as the structure of the film will typically be aligned to only a few nuclei [23].

(ii)Substrate Temperature. Low substrate temperatures result in the formation of amorphous films. For CVD Si it has been observed that the films display little or no detectable structure below 600°C, while at deposition temperatures in excess of 1200°C it is possible to achieve single crystal growth. The temperature range in between results in the formation of polycrystalline films. The influence of substrate temperature can be considered in two ways. First, one considers the effects of the substrate temperature on the nuclei formation. Higher temperatures favor the formation of larger but fewer nuclei, which logically, from the arguments of (i), is favorable for the formation of structured films [23]. The other effect of low substrate temperatures is the reduction of the surface mobility of adatoms. This causes adatoms to be incorporated into the film prior to reaching the most energetically favorable sites, corresponding to crystallographic structure, resulting in a disordered film [37].

(iii) Deposition Rate. The effect of the deposition rate can also be associated with nuclei formation. Higher deposition rates result in higher nuclei formation rates which was previously associated in (i) with amorphous or fine-grained film formation [23].

2.3 Post-Deposition Thermal Annealing

Following their deposition films may be subjected to thermal annealing. This process can serve a few important roles in modifying the deposited film composition and structure through atomic diffusion and crystallization processes, which will be discussed in the following subsections. This section will be primarily qualitative as the details of diffusion go beyond the focus of this project.

2.3.1 Atomic Diffusion

High temperature annealing can provide sufficient thermal energy for interstitially incorporated species such as Ar and H to out-diffuse from the film. Additionally, Si-H bonds may be broken if the anneal temperature is sufficiently high. H atoms incorporated during the deposition process may then also out-diffuse from the films. Annealing also allows for interdiffusion within the films which can modify the film structure. Hence the process can play a significant role in modifying thin film properties.

The fundamental equations of diffusion are given by Fick's first and second laws:

$$J = -D\frac{\partial C}{\partial x} \tag{2.40}$$

and

$$\frac{\partial C}{\partial t} = D\frac{\partial^2 C}{\partial x^2} \tag{2.41}$$

where J is the flux, or the number of particles passing through a unit area per unit time, C is the concentration, and D is the diffusion coefficient. The equations are simplified here for the case of isotropic media, anisotropic media require an expansion of these equations using diffusion coefficients which may vary based on direction and partial derivatives for these directions. Typically D is given through the equation:

$$D = D_0 e^{-E_a/RT} \tag{2.42}$$

where D_0 is a temperature independent constant, E_a is the activation energy for diffusion, R is the gas constant, and T is the temperature [38]. Fick's laws are mass transport laws that relate the rate of flow of matter to its concentration gradient.

The physics of the diffusion process are contained in the diffusion coefficient, which is a characteristic of given species within a given system.

Diffusion can typically be considered a random-walk process. The key point for out-diffusion is that once an Ar or H atom has reached the surface of the film it can escape into the anneal environment, at which point it is lost to the film. Ar is unbound and, therefore, must be located interstitially, or within voids within the film and diffuses interstitially until escape. H, however, is bonded and its removal from the film is expected to be slightly more complex. H must diffuse out of the film by first breaking its bond and then migrating to the surface. Along the way the atom may become rebound to dangling bonds within the film, however, sufficiently high anneal temperatures and long times will make it favorable for the H atom to continue its migration to the surface. It is also possible that the H atoms may encounter each other and form H_2 molecules, which could then diffuse in a similar manner to Ar.

Interdiffusion of Si and O atoms may also be considered a random walk type process, however, now one considers atomic species migrating only within the film, with a decreased probability of escape, as Si and O atoms will be more strongly bound within the films. The interdiffusion process therefore causes a structural reordering of the film.

In a similar manner one can consider the random formation of critical nuclei within the film as a diffusion process. This serves as the basis of nanocluster formation within SRSO films. Si nuclei form within the films and grow in size. A random distribution of precipitates will form in the film with a size distribution related to the amount of excess Si and the anneal temperature and time. Eventually most of the excess Si will be contained in these clusters. Further growth can then occur through the process of Ostwald ripening discussed above, where larger nanoclusters assimilate smaller ones within their vicinity, allowing for a minimization of the surface free energy of the system.

Nanocluster formation is also accompanied by a reordering of SiO_2 within the film, as bonds that were distorted in order to accommodate the excess Si can now reorder.

The diffusion process thus results in a phase separation within these films, where the resulting phases formed after the anneal process are SiO_2 and Si. This phase

separation may be described using the equation [39]:

$$SiO_x \rightarrow \frac{x}{2} SiO_2 + \left(1 - \frac{x}{2}\right) Si \tag{2.43}$$

2.3.2 Thermally Induced Crystallization

In terms of structure, sufficiently high anneal temperatures can allow for a modification of the atomic bonding arrangements within the film and cause crystallization to occur, which can produce nano, micro, and poly-crystalline phases within Si-based films.

By carrying on from the previous section one can obtain a qualitative idea of how nano- and poly-crystallinity arise. By annealing at sufficiently high temperatures certain nuclei will obtain sufficient thermal energy to reorder themselves to the more energetically favorable crystalline orientation. It is simple enough to conceptually understand how this gives rise to nanocrystals in SRSO films. Clusters of excess silicon rearrange in a crystalline formation. With increased anneal temperature and time diffusion allows these clusters to grow in size. As discussed above the formation of nano-clusters and crystals is additionally accompanied by a reordering of the oxide host in SRSO films.

Chapter 3

Optical and Luminescent Properties of Silicon-based Materials

This chapter reviews some of the properties of silicon and silicon oxide materials. Of course, a large amount of literature exists on the topic, especially in relation to the electronic properties of Si, due to its prominence in microelectronics. A complete review would be difficult and the focus will be primarily on properties that are specifically related to the use of silicon as a photonic material and which are relevant to the work presented in this thesis. Specifically, this includes a review of optical and photoluminescent properties of Si, with a discussion of how these depend on the composition and structure of Si-based films.

It is important to note that some of these properties, such as the optical constants of the materials, are not absolutely universal and can often vary based on factors such as the method of film growth, and the quality and density of the film. These properties are therefore outlined in order to serve as a general reference on the topic and to serve as a basis for comparison with the films grown for this work.

While PECVD grown films are typically amorphous in nature (variation of the deposition parameters can produce films with varying levels of crystallinity) a discussion of crystalline silicon is also in order in this section, as it provides the necessary

background to understand the problem with achieving luminescence in Si and the unique luminescent properties of nanoscale Si crystals.

3.1 Silicon

Silicon can be amorphous, crystalline, or in an intermediate state of crystallinity between the two, depending on the method of fabrication and the type of processing treatment the material is subjected to, as discussed in the previous chapter. The resultant optical behavior of the material is dependent upon the degree of crystallinity in the material. Crystalline Si bonds in the diamond structure, which is produced by interpenetrating two FCC lattices along the body diagonal of a cubic cell by one quarter of the length of the diagonal. The diamond crystal structure is shown in Figure 3.1.

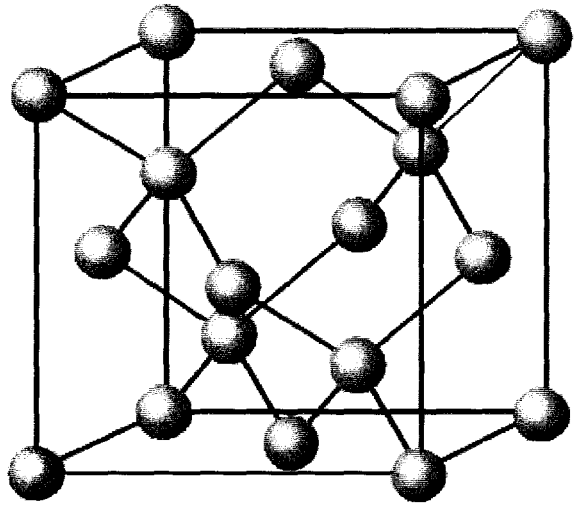

Figure 3.1: The diamond crystal structure of Si.

Amorphous Si, by definition, bonds with no long range order, as shown in Figure 3.2 [40]. This lack of order results in dangling bonds and hydrogen may be incorporated into the films through their passivation.

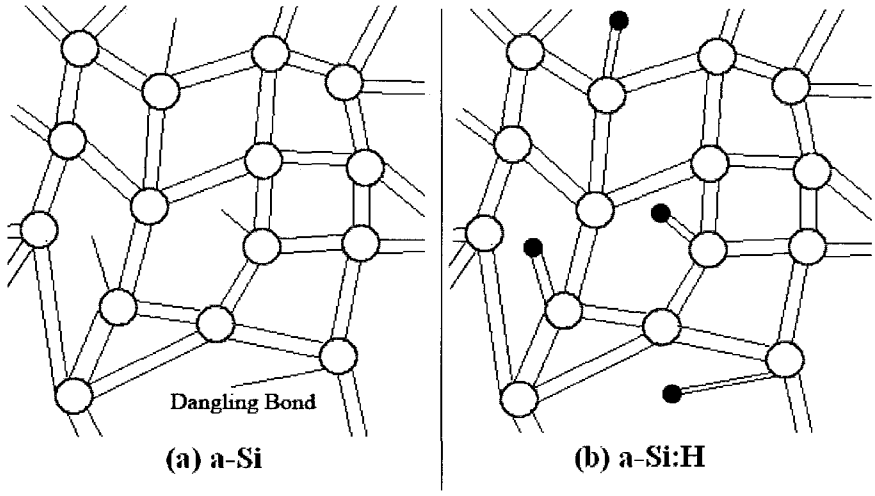

Figure 3.2: (a) A 2D schematic illustrating the structure of amorphous silicon. The structure leads to the formation of dangling bonds which allow for hydrogen incorporation within the film, producing hydrogenated a-Si, as shown in (b) [40].

3.1.1 Band Structure

Many of the characteristics of Si, including its electronic and optical properties, are related to the electronic band structure. The band structure of a material arises as a result of the atomic bonding structure and the interaction of atomic wavefunctions as atoms come together to form a solid structure. This interaction leads to a forbidden region of energies, producing a bandgap, E_G, in semiconducting materials. The details may be found in any solid state textbook. Silicon is an indirect bandgap structure, as compared to GaAs which has a direct bandgap. This concept is illustrated in Figure 3.3 which shows the bandgaps from both materials derived from pseudopotential calculations [41].

In GaAs the minimum of the conduction band and the maximum of the valence band lie at the same point (Γ) on the reciprocal lattice, which is why GaAs is a direct bandgap semiconductor ($E_G = 1.42\ eV$). Si, however, has its conduction band minimum located near the **X** point, while its valence band maximum is at the Γ point, making Si an indirect bandgap semiconductor ($E_G = 1.12\ eV$). In GaAs the transition of an electron from the valence to the conduction band can proceed through

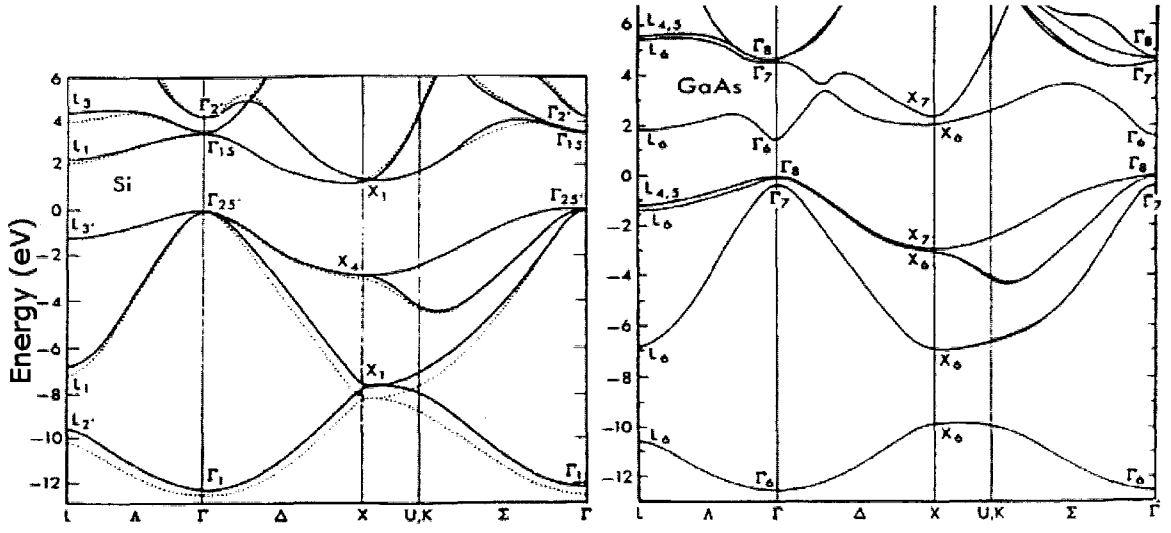

Figure 3.3: The electronic band structure of (a) Si and (b) GaAs. In the case of (a) the band structure was determined through both nonlocal (solid lines) and local (dashed lines) pseudopotential calculations [41].

the simple absorption of a photon to raise its energy. In Si the transition requires some phonon interaction in order to change the momentum of the electron such that it can be excited to the **X** point. The same holds true for a luminescent decay to occur in Si. The need for phonon interactions decreases the probability of emission in Si, causing the spontaneous recombination lifetime of Si to be in the msec range. Additionally, the luminescence of Si is limited by fast non-radiative decay processes such as the Auger process and free-carrier absorption [7, 42].

3.1.2 The Optical Properties of Silicon

A thorough analysis of the dielectric function and refractive indices of Si, as well as other semiconducting materials, was given by Aspnes and Studna [43]. In this analysis the optical characterization of the materials was done through spectroscopic ellipsometry. The details of ellipsometry are discussed in Chapter 6. Figure 3.4 is a reproduction of their results from the data provided in the above reference.

The optical properties of a-Si vary slightly from those of crystalline silicon. Figure

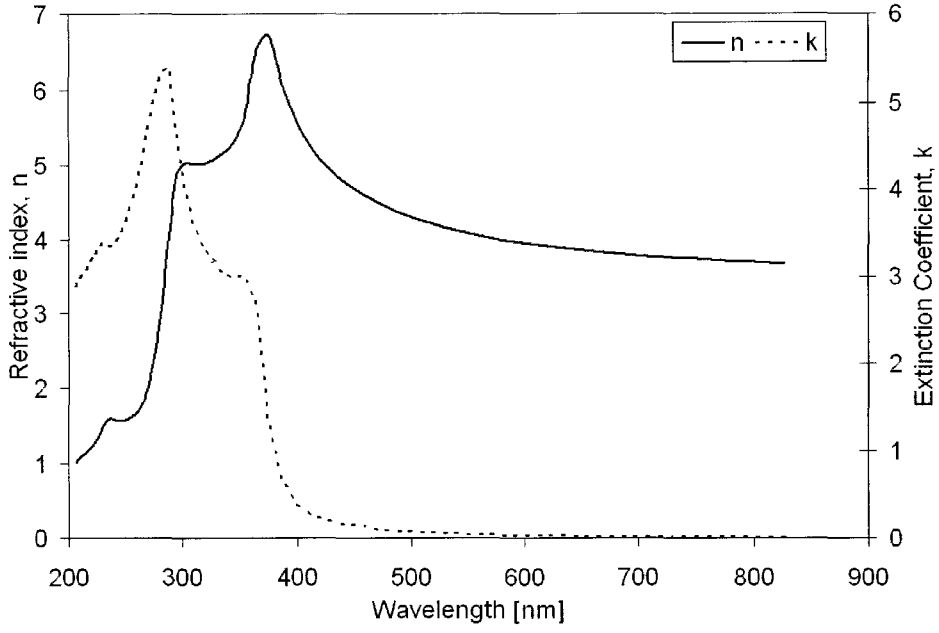

Figure 3.4: The optical constants, n and k, of crystalline silicon [43].

3.5 shows the optical constants for two different a-Si films, with one of the films being hydrogenated [44]. The amount of deviation in the optical constants of a-Si:H films from those of a-Si is dependent on the amount of hydrogen incorporated in the films.

In addition to the hydrogen content playing a role in the observed optical properties of a-Si films, the method of preparation can also play a significant role. Sputtered a-Si:H films have been found to have lower extinction coefficients than glow discharge a-Si:H films having the same amount of hydrogen [45].

When comparing the optical properties of a-Si to those of crystalline Si one notes the loss of fine structure, which, in crystalline Si arises as a result of singularities in the band structure, such as the direct band transition at Γ with energy $E = 3.4eV$, which leads to the absorption edge around 365 nm. Features such as these are sensitive to the order of the system and broaden rapidly as this order is decreased [46].

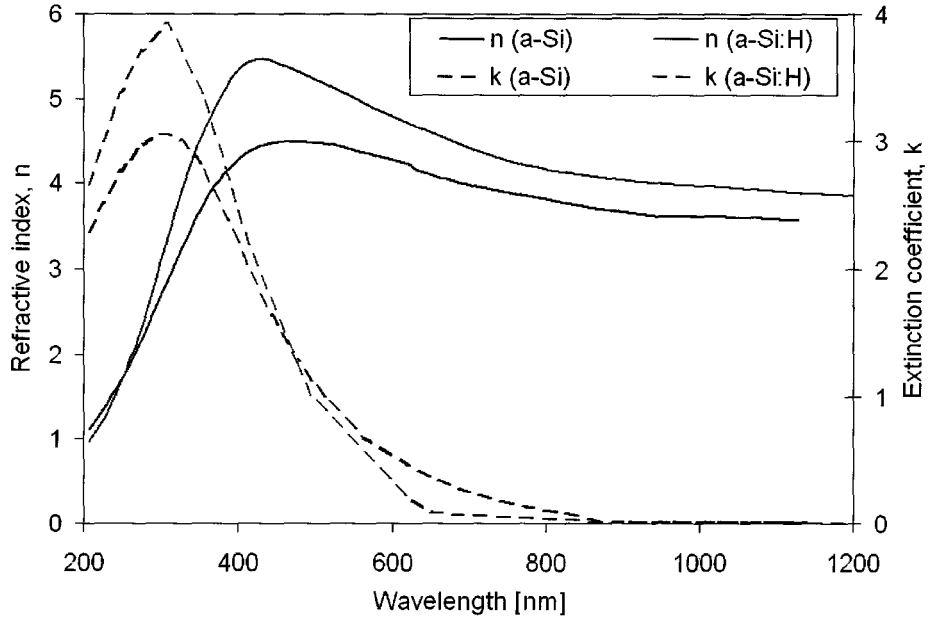

Figure 3.5: The optical constants, n and k, of amorphous silicon. The data plotted in black is for a-Si while the data plotted in blue is for a-Si:H [44].

3.2 Silicon Dioxide

The optical properties of amorphous SiO_2 are shown in Figure 3.6 [44]. Note that over the region discussed here SiO_2 is transparent and hence $k = 0$. SiO_2 also has a crystalline phase. The refractive index of crystalline SiO_2, quartz, is larger than that of amorphous SiO_2 ($n_{Quartz} = 1.55$, $n_{a-SiO_2} = 1.46$, at 633 nm) due largely to the increased density of the crystalline structure which results in less void space within the film [23]. The details of crystalline SiO_2 are not relevant to this work and are not considered any further.

In addition to having optical properties suitable for waveguide design, SiO_2 can also play a vital role in the quantum confined luminescence process. While silicon is a semiconducting material, SiO_2 is a dielectric material and can serve as a large bandgap barrier to aid in the confinement process with silicon nanocrystals, discussed later in this chapter [47].

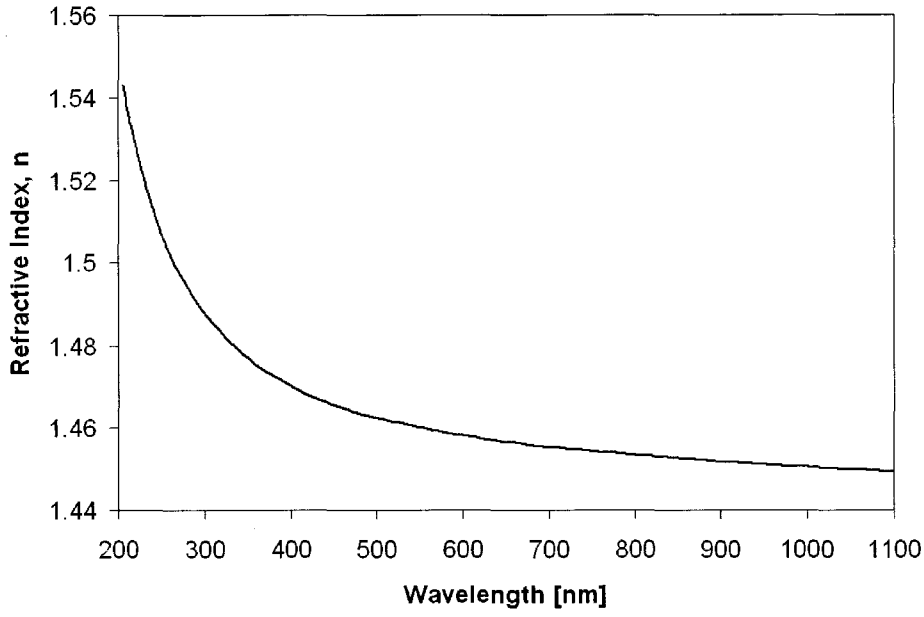

Figure 3.6: The refractive index, n, of SiO_2 [44].

3.3 Silicon Rich Silicon Oxides

Silicon rich silicon oxides can be thought of as an intermediate combination of two compositions, amorphous silicon and silicon dioxide. In fact, under thermal annealing conditions it is possible to phase separate the film into Si and SiO_2 states. The effect of mixing these two constituents on the optical properties is an increase in both the refractive index and extinction coefficients of the films with increased Si content. While a comprehensive data set of optical properties of films with varying SRSO compositions is not readily available, Figure 3.7 shows the refractive index and extinction coefficient of silicon monoxide, SiO, as a function of wavelength [44].

3.4 Silicon Nanocrystals

Si nanocrystals are a case of crystalline Si, in which the dimensions of the crystal are on the order of a few nm. The significance of these nanocrystals is that they lead

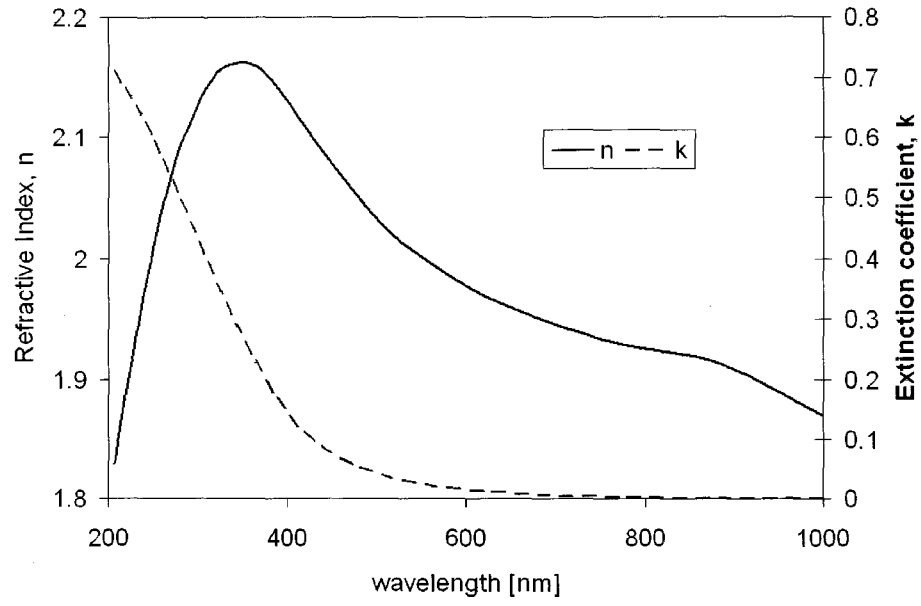

Figure 3.7: The optical constants, n and k, of SiO [44].

to quantum confined states, which allow for luminescent recombinations to occur in Si, which, as discussed above, is difficult to achieve in bulk Si.

Silicon nanocrystals may be produced by: (i) deposition of silicon rich silicon oxide thin films, followed by a post deposition thermal anneal to produce phase separation, as is the method explored in this research; (ii) Ion implantation of Si into SiO_2 films, followed by an anneal to repair implantation damage and cause nanocrystal nucleation; (iii) Deposition of SiO/SiO_2 superlattices and subjecting them to a thermal anneal. The latter method appears quite advantageous, as reports indicate that by controlling the width and location of the SiO layer, better control is obtained over the size and spatial distribution of the nanocrystals [39].

3.4.1 Luminescence from Silicon Nanocrystals

This section will deal with how luminescence is produced through quantum confinement in Si. In order to minimize overlap with Chapter 6, this section will focus on

the basic mechanisms related to quantum confinement in Si nanocrystals, reviewing some of the more important results and details within the literature related to the subject, necessary to understand how the process occurs. Chapter 6 will review the more general case of quantum confinement in structures with reduced dimensions and its effect on luminescence.

As crystallite sizes decrease to a few nanometers, quantum confinement causes discrete electronic states to be present within the nanocrystal, when the nanocrystal is surrounded by a high energy barrier material. Electrons and holes then become confined within the nanocrystal, with energies related to these discrete states. The process can be considered to be similar to a particle confined in three dimensions and described through quantum mechanics. One important factor in the recombination process arises from the uncertainty principle, where, as the electrons and holes are confined, their wavefunctions become delocalized over the nanocrystals and may overlap, causing a relaxation in the k-selection rule. Therefore, the need for phonon interaction in the recombination process is relaxed. The confinement process leads to a widening of the bandgap which causes visible luminescence to be observed [48]. This process only becomes possible when the size of the nanocrystals decreases sufficiently to cause strong confinement, which occurs when the radius of the nanocrystal is less than the Bohr free exciton radius of the material ($a_0 = 4.3nm$ in c-Si) [47].

While quantum confinement is generally accepted to play a dominant role in the luminescence of nc-Si, the full mechanisms of the luminescence are still a subject of much debate. In addition to quantum confinement one must consider the role of the host matrix, as well as defect and surface states in the luminescence process. A study of porous Si quantum dots by Wolkin *et al.* examined the role of oxygen in this process [49]. In their work they found that Si=O bonds produce localized levels that lead to electron and exciton trapping for small crystallites. The formation of localized states causes a stabilization of the PL emission wavelength, even as quantum confinement suggests that further blueshifting should be observed. In the case of H passivated nanocrystals it has been found that this effect is absent and blue luminescence can be obtained with small enough crystal sizes [49,50]. Further review of some of the shortcomings of the quantum confinement model and an analysis of

other luminescence mechanisms was presented for porous Si structures and may be found in [51].

Further details about luminescence from Si can be found in [52–55]. In these references some additional mechanisms related to the process are discussed. The details provided above, combined with the discussion of quantum confinement in Chapter 6 should be sufficient to understand the basic factors influencing the luminescence process.

One final note regarding luminescence from Si nanocrystals: Using a variable stripe length method, through which amplified spontaneous emission can be examined by varying the excitation length of the sample, gain has been observed in Si-ncs embedded within an SiO_2 host [7]. This observation of gain is an important feature as light amplification is a necessity in the development of any laser.

3.4.2 Other Approaches to Luminescent Silicon

Silicon nanocrystals have not been the only method of obtaining luminescence from Si. The first observation of bright luminescence was made with porous Si by L. Canham [6]. In that work Si was subjected to an anodic etch resulting in a highly porous structure, which can be considered a skeleton of silicon nanowires, leading to quantum confinement in a similar manner to that discussed for Si nanocrystals. While bright luminescence is observed from these structures they suffer from a frailty due to their porosity, and age rapidly, which causes a variation in their performance [49]. Porous silicon has, however, been used to fabricate LEDs in spite of its drawbacks [56].

Another method of producing luminescent Si was derived from reversing some of the leading work in Si solar cells. By taking very pure Si with a high quality thermal oxide grown on the surface, free carrier effects, non-radiative processes, and surface recombinations are reduced, reducing the amount of reabsorption of emitted photons within the device. The surface of the device is then patterned in order enhance the extraction efficiency of light. Unfortunately, the need for high-quality Si and surface texturing make the process incompatible with CMOS processing and has drawbacks in terms of integrability [10].

Additional details of silicon nanocrystals, porous silicon, and other methods used to increase the luminescence of Si for applications in integrated photonics are reviewed and discussed in [57].

It should be noted that during the course of writing this thesis the first implementation of a Si laser was demonstrated based on amplification of an optical input through the Raman effect [58]. Their method of causing lasing in Si is not one that would be suitable for integrated photonics, but the results do serve as a milestone in gaining light from Si.

Chapter 4

Compositional Characterization Using Ion Beam Analysis

The composition of the films was determined using two methods of ion beam analysis, Rutherford backscattering spectrometry (RBS), and elastic recoil detection (ERD). Ion beam analysis techniques examine the various reactions that occur when an energetic beam of charged particles (such as α particles, which are often used) is incident on a solid target as shown in Figure 4.1. In addition to RBS and ERD, the figure also illustrates other possible ion beam analysis techniques, including nuclear reaction analysis (NRA), secondary ion mass spectroscopy (SIMS), and particle induced x-ray emission (PIXE) [59].

This chapter discusses the underlying theory of RBS and ERD and their use for quantitatively determining the areal densities of silicon, oxygen, argon, and hydrogen within the films.

4.1 Rutherford Backscattering Spectrometry

RBS experiments are done using light ions with energies in the range of a few MeV and allows for an accurate determination of elemental areal densities and stoichiometry of the films. RBS works by detecting ions backscattered, or scattered at large angles (typically $\geq 150°$), from atoms within the films being analyzed. Through

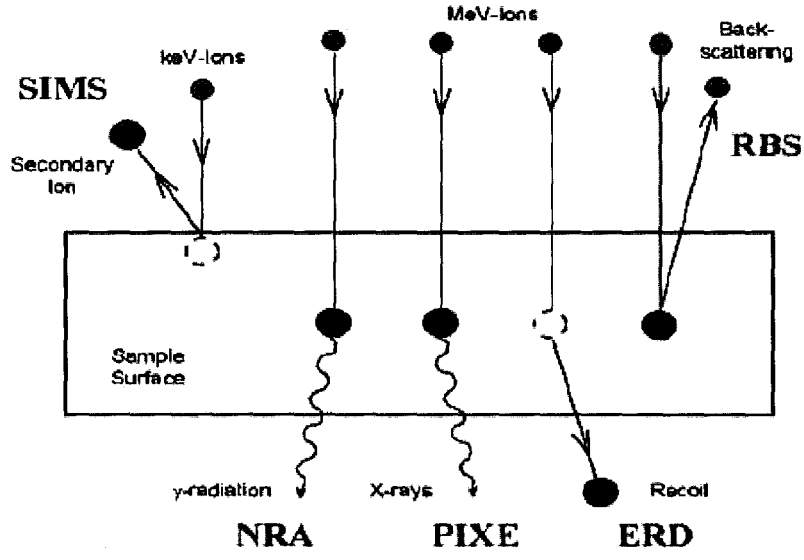

Figure 4.1: Possible reactions when energetic ions are incident on a solid sample [59].

analysis of the number and energies of the backscattered ions it is possible to determine the type of atom that caused the backscattering as well as its concentration and distribution below the film surface.

Consider Figure 4.2 [60]. The left portion of the figure illustrates a typical backscattering experimental setup, while the right portion shows a typical RBS spectrum for a film with composition A_mB_n.

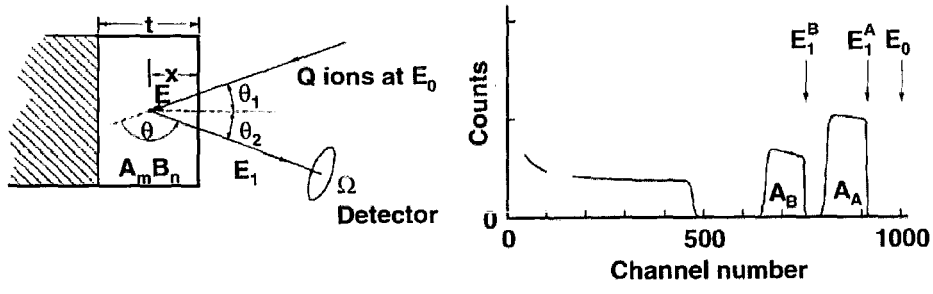

Figure 4.2: A typical RBS experimental setup and spectrum [60].

An understanding of RBS and interpretation of this figure requires an analysis of the kinematics of elastic scattering. Figure 4.3 illustrates the geometry of the scattering process that occurs during an RBS experiment [61].

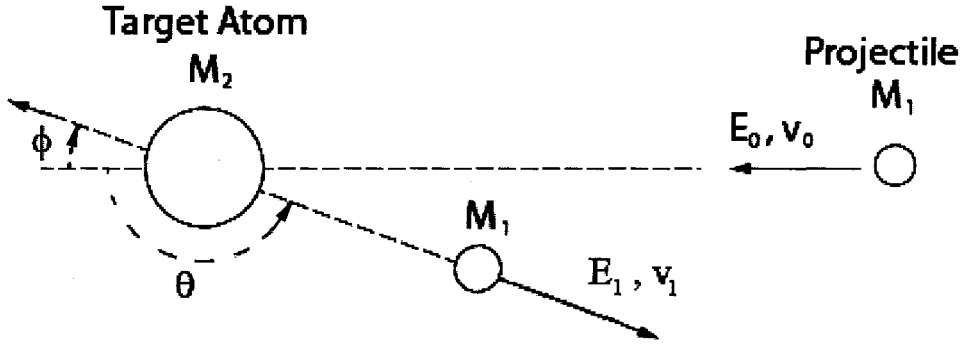

Figure 4.3: RBS backscattering geometry [61].

An ion of mass M_1, and having energy E_0 and velocity v_0, is incident on an atom of mass M_2, where $M_2 > M_1$. After the collision the ion is backscattered at an angle θ and has energy E_1 and velocity v_1, while the atom recoils at an angle ϕ with an energy E_2. Because momentum must be conserved during the process, E_1 is determined by the mass of the atom off which it has scattered, with the count rate of ions from a collision with an atom being determined by the scattering cross-section, σ, of that atom [61].

From application of the conservation of momentum and energy one obtains the ratio of energies of the scattered ion to the incident ion as:

$$\frac{E_1}{E_0} = K \tag{4.1}$$

where K is the kinematic factor defined by:

$$K = \left[\frac{(M_2^2 - M_1^2 \sin^2\theta)^{1/2} + M_1 \cos\theta}{M_1 + M_2}\right]^2 \tag{4.2}$$

Therefore, once E_1 has been measured M_2 may be determined since E_0 and M_1

are known quantities. For different atoms K is often denoted as K_i, where i is used to denote the i^{th} element in a compound material.

Because the particles are charged they will interact according to Coulomb's law where the force between the incident ion with atomic number Z_1 and the target atom with atomic number Z_2 is given by:

$$F = \frac{Z_1 Z_2}{R^2} \tag{4.3}$$

and Rutherford scattering will occur. The differential scattering cross-section, $\frac{d\sigma}{d\Omega}$, which is a measure of the probability of scattering at an angle θ within the differential solid angle of the detector, $d\Omega$, is given, in the laboratory frame of reference here, by Rutherford's Law (in cgs units):

$$\frac{d\sigma}{d\Omega} = \left(\frac{Z_1 Z_2 e^2}{4E}\right)^2 \frac{4}{\sin^4\theta} \frac{\{[1-((M_1/M_2)sin\theta)^2]^{1/2} + \cos\theta\}^2}{[1-((M_1/M_2)sin\theta)^2]^{1/2}} \tag{4.4}$$

The average scattering cross section, often just called the scattering cross section, is then:

$$\sigma = \frac{1}{\Omega}\int_\Omega \left(\frac{d\sigma}{d\Omega}\right) d\Omega \tag{4.5}$$

The total yield of detected particles, A (sometimes denoted as Y in the literature), is then given by:

$$A = \sigma\Omega \cdot Q \cdot Nt \tag{4.6}$$

where Ω is the solid angle of the detector, Q is the total number of incident particles, and Nt is the number of target atoms per unit area. It should be noted that equation 4.6 assumes that a detector with 100% efficiency is used, which is the case for charged particle detectors. In the event that a detector with a lower efficiency were used an additional multiplicative factor, ϵ_d $(0 < \epsilon_d < 1)$, should be included [60].

If the sample spectrum of Figure 4.2 is now considered it is possible to see how the composition of the films is determined although there is one other consideration that should be addressed. The energy, $E_1^A = K_i^A E_0$, after scattering from an atom, A, is actually only the energy after scattering from a surface atom. Scattered ions that penetrate into the film lose some energy as they traverse to and from a depth, x, into and out of the film, which results in an energy spread for the yielded number

of counted ions. From Figure 4.2 let us consider the back edge of the yield for either of the atoms as E_2. The energy difference between an ion scattered from a depth x and one scattered from the surface is then:

$$\Delta E = E_1 - E_2 = KE_0 - E_2 \tag{4.7}$$

The energy loss factor, S, is then defined through:

$$\Delta E = [S]x \tag{4.8}$$

so

$$[S] = \left[\frac{K}{\cos\theta_1}\frac{dE}{dx}\bigg|_{in} + \frac{1}{\cos\theta_2}\frac{dE}{dx}\bigg|_{out}\right] \tag{4.9}$$

The energy loss is often expressed in terms of the stopping cross section of the material where:

$$\Delta E = [\varepsilon]Nx \tag{4.10}$$

with the stopping cross-section, $[\varepsilon]$, defined as:

$$[\varepsilon] = \left[\frac{K}{\cos\theta_1}\varepsilon_{in} + \frac{1}{\cos\theta_2}\varepsilon_{out}\right] \tag{4.11}$$

If one knew the stopping power or stopping cross sections as a function of projectile energy the energy spread could be used to determine atomic concentrations as a function of depth as well as film thicknesses. For films with compound structures Bragg's Rule says that the stopping cross section of the film is simply the sum of the stopping cross sections for each element multiplied by their molar concentration [62]. So for a film A_mB_n the stopping cross section is:

$$\varepsilon_{A_mB_n} = m\varepsilon_A + n\varepsilon_B \tag{4.12}$$

Unfortunately determination of the stopping power of a sample is complex and difficult to do accurately, especially in films such as those discussed in this thesis where densities can vary largely. Because of this energy loss one should be aware that if a film is composed of separate layers then the measured energy edge of the buried layer will be observed at lower energies than those calculated using the kinematic factor.

Once the kinematic factor is known for atoms of a given mass, E_1 is easily determined for that atom and the constituent species of a film may be identified by determining what atoms correspond with the high end energies of the RBS yield spectra. The yield for that species is easily determined from the spectrum. The number of ions incident on the film is a controlled, known, parameter, and Equation 4.6 may be used to determine the areal concentration, Nt, for that species provided the scattering cross section and the solid angle of the detector are known.

From the above derivations one practical aspect of RBS analysis must be considered. Increased mass of an atom results in an increased kinematic factor and hence higher scattering energies for ions scattered from that atom. The width of the yield spectrum for an atom is related to the thickness of the sample. If a layer containing light atoms is deposited onto a sufficiently thick layer or substrate of heavier atoms the width of the peak due to the heavier atoms will extend significantly to lower energies. The peak due to the lighter atoms will then be superimposed upon that of the heavier atoms. For this reason RBS experiments work best when using a heavy on light system which allows for the clear resolution of peaks [60, 61].

4.2 Elastic Recoil Detection

Like RBS, elastic recoil detection is done through the analysis of the scattered particles when an energetic beam of charged ions is incident on a sample. However, in lieu of backscattered ions, ERD experiments detect light atoms that have undergone a forward recoil motion and have been "knocked out" of the film. This occurs when the mass of the incident particle is greater than or equal to that of a target atom. Figure 4.4(a) illustrates a typical ERD experimental setup, while 4.4(b) illustrates the geometry of the elastic scattering process involved for a kinematic analysis [60].

Typical geometries place the target film at a glancing angle, typically 15°, with respect to the ion beam direction while the detector is placed a forward angle of 30°.

The RBS equations 4.1 and 4.2 discussed previously are still valid for describing the scattered ion, however the scattering angle, θ, is typically not large enough for the ion to be backscattered. θ, however, is not really the angle of interest to us, instead

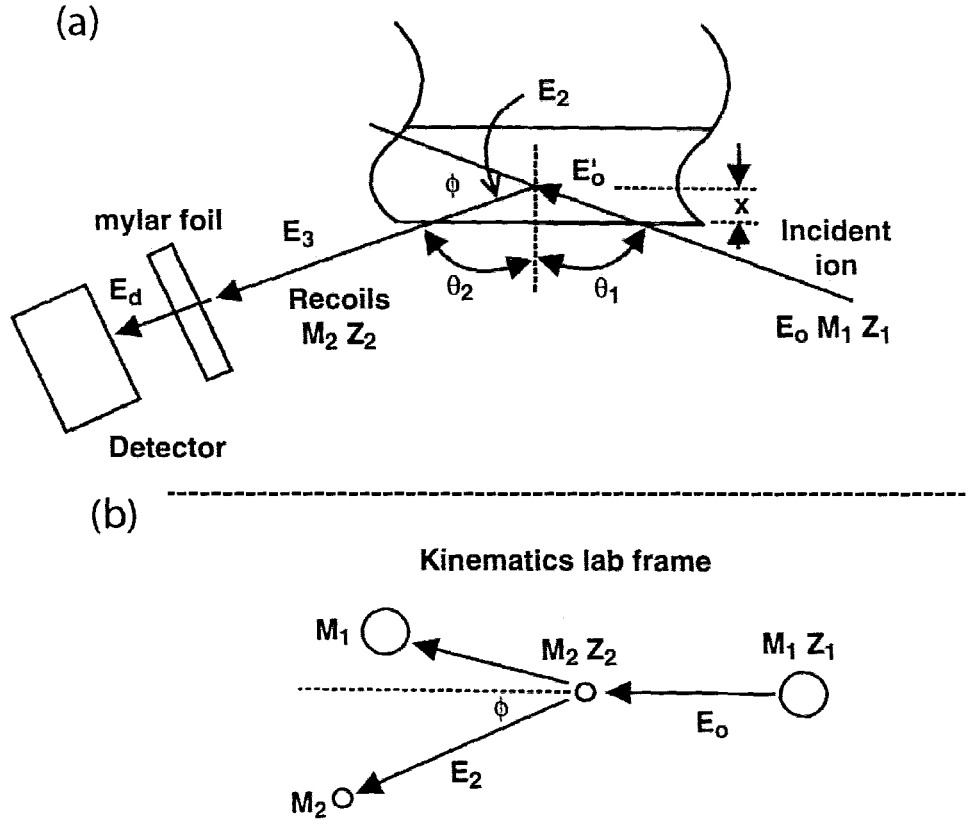

Figure 4.4: (a) The experimental setup of an ERD experiment for Thin Film Analysis. (b) A schematic representation of the elastic collision that occurs in ERD [60].

we focus on the recoiled nucleus, which must undergo a forward motion after the collision due to momentum considerations. The atom recoils at an angle ϕ as shown. Its energy, E_2 is obtained through the conservation of energy and Equation 4.2 as:

$$\frac{E_2}{E_0} = 1 - \frac{E_1}{E_0} = \frac{4M_1M_2}{(M_1+M_2)^2}\cos^2\phi \tag{4.13}$$

As with RBS the atom will lose some energy as it travels through the film and exits the film with an energy E_3. Because the ions may also undergo scattering from heavier atoms within the film and strike the detector a mylar range foil, which acts as a particle filter, is used. Based on the type and energy of the incident ions the foil thickness is chosen such that the ions are stopped by the range foil, while the lighter recoil atoms, such as H, are able to pass through. During the analysis one must factor

in the energy loss of the recoil atoms as they pass through this foil. Recoil atoms therefore arrive at the detector with an energy E_d = E_3-δE, where δE is the energy lost while passing through the foil. This process is related to the stopping power of the foil for the ions and the scattered atoms [60, 63].

In essence the physical principals of ERD are the same as those for RBS. The yield of recoiled atoms at an energy E_d will be:

$$Y_r(E_d) = \frac{QN_r(x)\sigma_r(E_0', \phi)\Omega\delta E_d}{\cos\theta_1(dE_d/dx)} \tag{4.14}$$

where $N_r(x)$ is the atomic number density of the recoiled atom at a depth x, $\sigma_r(E_0', \phi)$ is the recoil differential scattering cross section, E_0' is the energy at which the ion strikes the atom after traversing into the film to a depth x, and δE_d is the channel width of the detector.

As with RBS the scattering is coulombic in nature and may be modeled as:

$$\sigma_r(E_0', \phi) = \frac{[Z_1 Z_2 e^2(M_1 + M_2)]^2}{[2M_2 E_0']^2 \cos^3\phi} \tag{4.15}$$

For example, the areal density of hydrogen, AD_H, in a film is obtained from the integrated concentration of hydrogen, N_H, over a layer thickness, t.

$$AD_H = \int_0^t N_H(x)dx = \frac{\cos\theta_1}{Q\Omega}\int_0^t \frac{S^{eff}}{\sigma\delta E_d}Y(E_d)dx, \tag{4.16}$$

where S^{eff} is the effective stopping power of the recoil atoms in the foil layer. Substituting $S^{eff} = dE_d/dx|_x$ into Equation 4.16 the resulting expression for AD_H becomes

$$AD_H = \frac{\cos\theta_1}{Q\Omega}\int_{E_d(0)}^{E_d(x)} \frac{Y(E_d)dE_d}{\sigma\delta E_d} \tag{4.17}$$

In practice the integral is approximated as a summation and the areal density of hydrogen is determined, for thin films, through:

$$AD_H = \frac{\cos\theta_1}{Q\Omega\sigma_0}\sum_{Channel[E_d]}^{Channel[E_d(x)]} Y(Channel) \tag{4.18}$$

For thick films it often necessary to approach the problem using a slab analysis technique, the details of which will be left to literature, which is not necessary for the analysis of the films discussed within this thesis [60].

Chapter 5

Characterization of Bonding Structure Using Fourier Transform Infrared Spectroscopy

Fourier transform infrared spectroscopy is a non-destructive, optical measurement technique that allows for the determination of the bonding structure within the films through analysis of absorption or transmission spectra. In this chapter the principles and experimental setup of FTIR analysis are discussed.

5.1 Fundamentals of Fourier Transform Infrared Spectroscopy

When atoms bond they exhibit resonant absorption of infrared light by their vibrational and rotational modes. The wavelength, or, as is often the method of reference in the literature, the optical frequency (wavenumber) at which the light is absorbed and the bond resonates is characteristic to the bonding atoms, type, as well as the local environment of the bond. Different constituent atoms and molecules can therefore be identified to be present within thin films through analysis of IR absorption spectra.

Figure 5.1 illustrates the setup of an FTIR spectrometer. The setup is based on the principles of a Michelson interferometer. Light from a broadband IR source is incident on a beam splitter (BS), causing the light to travel down two paths. Part of the light travels through the BS and is reflected by a fixed mirror while the other part is reflected by the BS and then reflected again by a movable mirror. The two beams recombine and interfere at the BS producing an interferogram with intensity dependent on the difference in path length, Δ, between the two beams after reflection from the fixed and moving mirrors.

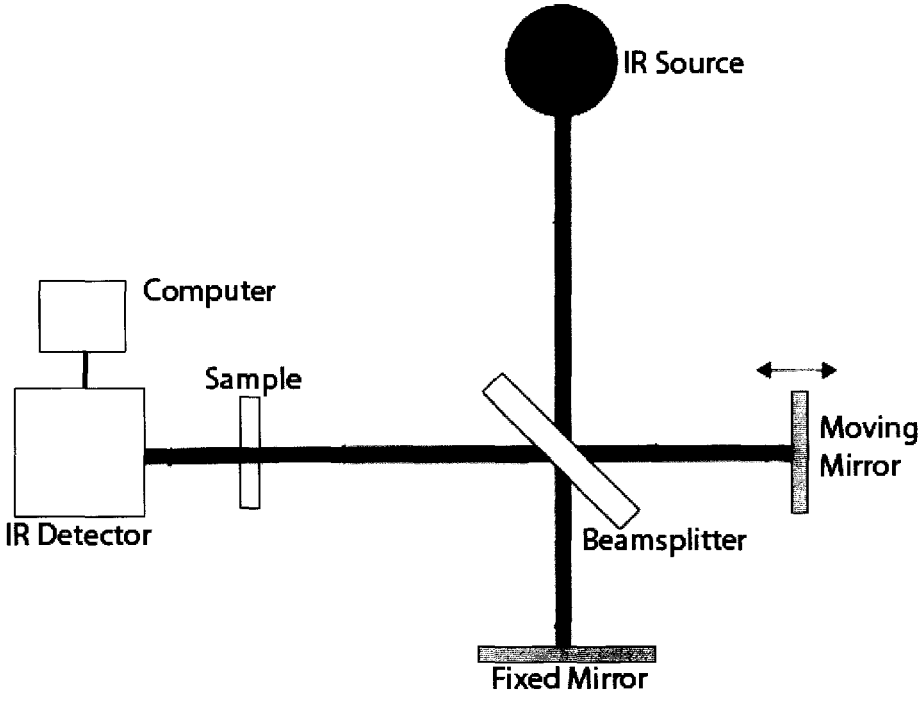

Figure 5.1: A Schematic of a Basic FTIR Spectroscopy Setup.

The intensity of the interferogram, I(Δ), is given by:

$$I(\Delta) = \int_{-\infty}^{+\infty} S(f)[1 + \cos(2\pi f\Delta)]df = \frac{1}{2}I(0) + \int_{-\infty}^{+\infty} S(f)\cos(2\pi f\Delta)df \qquad (5.1)$$

where $S(f)$is the intensity of the source spectrum, f is the optical frequency (in cm^{-1}),

and $I(0)$ is the intensity of the interferogram at zero path length difference.

This intensity is measured by the detector as a function of the optical path difference. Equation 5.1 is, however, simply the cosine Fourier transform of the source spectrum. $S(f)$ can therefore be recovered by taking the inverse Fourier transform of the intensity:

$$S(f) = \int_{-\infty}^{+\infty} [I(\Delta) - \frac{1}{2}I(0)] \cos(2\pi f \Delta) d\Delta \tag{5.2}$$

The recovery of the input signal is made easier by modern computers which are able to apply the fast Fourier transform, an algorithm for implementing a discrete Fourier transform in a short amount of time. It should be noted that Equations 5.1 and 5.2 ignore the presence of a constant multiplicative factor. In practice the signal to noise ratio is improved by obtaining several hundred interferogram spectra, averaging, and then applying the inverse Fourier transform. It should also be noted that in real world applications the limits of the integrals in equations 5.1 and 5.2 are never actually $-\infty$ to $+\infty$, but are rather -L to +L, where L may be taken as the limit of mirror movement. This limitation imposes a limitation on the wavenumber resolution of the system [64].

Of course the recovery of the source signal is really of little interest. Initially this spectrum is obtained only to provide a background spectrum to account for instrumental and environmental effects. When a sample is mounted as shown in Figure 5.1 the signal that is recovered through Equation 5.2 is the product of the wavenumber dependent film transmission coefficient, T(f), and the source spectrum, T(f)S(f). Therefore, the ratio of the spectrum with the sample in place and the source spectrum yields the transmission spectrum of the film alone. Note that the film spectrum is actually the product of the film and the substrate. Therefore, in order to remove substrate effects the transmission of the substrate should also be measured.

From the transmission spectrum an absorbance spectrum, A, may be obtained using:

$$A(f) = \log(1/T(f)) \tag{5.3}$$

Table 5.1: Silicon Related FTIR Peaks

Peak	Peak Position [cm^{-1}]
Si-O Stretching	1050-1080
Si-O Bending	800-815
Si-O Rocking	450-465
Si-OH	3640
Si-H Stretching	2160
Si-H Bending	$\sim$ 880
Si-H Wagging	$\sim$ 640
H_2O	3400

Ideally, the background spectrum remains constant during the period of experimentation and environmental effects, such as atmospheric water vapor and carbon dioxide, have their effects completely removed when the sample transmission spectrum is processed. In reality the concentrations of these species varies with time and may cause variations in the FTIR spectra. In order to reduce their effects the system is purged using a dry nitrogen line.

Another factor of which a user should be aware but which will not be discussed in detail is the sensitivity of the detector which limits the range over which a reliable signal may be obtained.

5.2 Analysis of FTIR Spectra

The simplest method for the interpretation of FTIR spectra is through analysis of strong absorbance bands and patterns in the spectrum and by comparing them with known reference spectra. This of course requires some information be known about the composition of the films so that the appropriate spectra can be used for comparison.

Common peaks associated with silicon oxide based materials are given in Table 5.1 [20, 21, 65, 66]. Note that no peaks related to Si-Si bonding are given, this is because silicon is transparent in the IR and no resonant absorption occurs for these bonds.

Of these peaks the Si-O stretching bond shows the strongest IR response and is

the most evident in the analysis of the FTIR spectra. An analysis of this peak by *Finch et al.* found that the position of the peak is related to the angle, 2θ, between two Si atoms bridged by an oxygen atom. The peak position is given by:

$$\nu = \nu_0 \sin\theta \tag{5.4}$$

where $\nu_0 = 1117\ \mathrm{cm}^{-1}$ [67]. In the case of good quality thermally grown SiO_2 this peak appears at $1080\ \mathrm{cm}^{-1}$, while its position is slightly lower for silicon rich silicon oxide materials. The full width at half maximum (FWHM) of the peak is an indication of the average spread of bond angles around the abridging atom.

The intensity of a given peak is related to the strength of IR absorption of that peak and to the number of bonds of the given peak type present within the films [65].

Chapter 6

Optical Characterization

Optical constants, refractive index and extinction coefficient, of the films were determined through the use of both single wavelength and spectroscopic ellipsometry. Ellipsometry is a powerful tool that allows for determination of the optical constants and thicknesses of thin films through analysis of the change in the polarization of light after reflection by or transmission through a material. In addition, based on the modeling technique used and the results obtained, ellipsometry is capable of determining thin film properties related to composition, and surface and interfacial roughnesses. The first few sections of this chapter deal with the physics of ellipsometry, experimental ellipsometric setups, and techniques for modeling results from ellipsometry measurements.

In order to analyze the emission wavelength of materials, which relates to the bandgap and recombination mechanisms of the material being considered for light emitting applications, photoluminescence is often used. The second half of this chapter focuses on the physics of the photoluminescence process, with an emphasis on how the process relates to quantum confinement effects in Si nanocrystals as discussed in Chapter 3, and the experimental PL setup.

6.1 Optical Characterization using Ellipsometry

Figure 6.1 shows the reflection of light at the surface of a sample showing the s (TE) and p (TM) components of polarized light incident upon and reflected from the sample. This figure illustrates the physical geometry used for ellipsometric measurement. In addition, Figure 6.2 shows the reflection and transmission of light incident on a thin film and substrate with refractive indices, n, where the subscripts 0, 1, and 2 refer to air, the thin film, and the substrate, respectively. For simplicity a single layer film on a substrate is considered, however, the arguments presented in this section can easily be expanded for multilayered films.

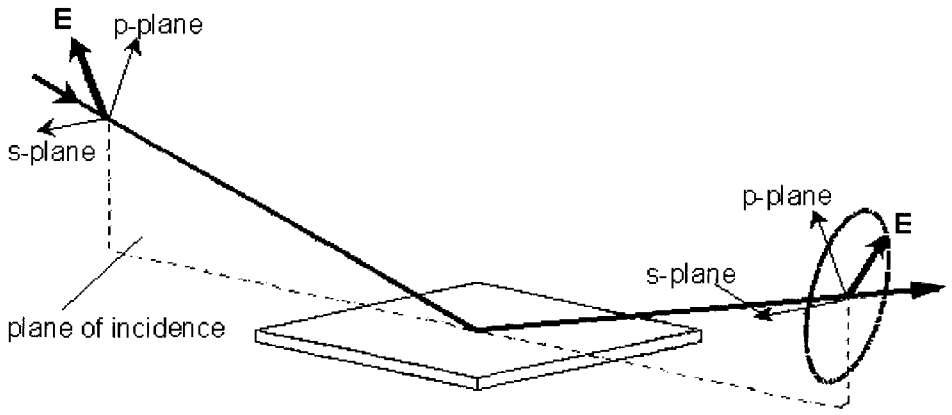

Figure 6.1: Interaction of polarized light with a sample.

More accurately the refractive index should be written as N, the complex index of refraction, where

$$N = n + ik \tag{6.1}$$

and k is the extinction coefficient of the material. From this point on N will be used in lieu of n.

The reflection, r, and transmission, t, coefficients of s and p polarized light at any interface between materials with refractive indices N_0 and N_1, which correspond to

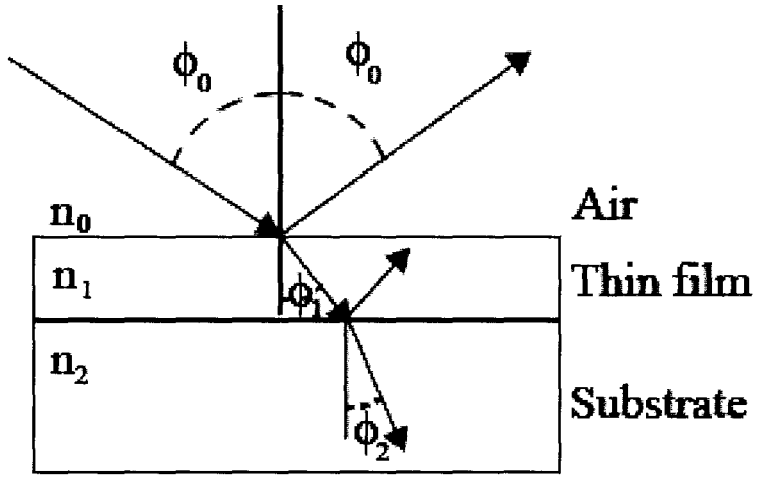

Figure 6.2: Reflection and transmission of light at a thin film interface.

the air-film interface in figure 6.2, are determined through the Fresnel coefficients:

$$r_{01}^s = \frac{N_0 \cos\phi_0 - N_1 \cos\phi_1}{N_0 \cos\phi_0 + N_1 \cos\phi_1} \tag{6.2}$$

$$t_{01}^s = \frac{2N_1 \cos\phi_1}{N_0 \cos\phi_0 + N_1 \cos\phi_1} \tag{6.3}$$

$$r_{01}^p = \frac{N_1 \cos\phi_0 - N_0 \cos\phi_1}{N_1 \cos\phi_0 + N_0 \cos\phi_1} \tag{6.4}$$

$$t_{01}^p = \frac{2N_1 \cos\phi_1}{N_1 \cos\phi_0 + N_0 \cos\phi_1} \tag{6.5}$$

The angles ϕ_0, ϕ_1, and ϕ_2 are related through Snell's law:

$$n_0 \sin\phi_0 = n_1 \sin\phi_1 = n_2 \sin\phi_2 \tag{6.6}$$

For ellipsometry the quantities of interest are the total resultant reflection coefficients, which arise from multiple reflections and transmissions of light within the thin film layer. To distinguish the resultant reflection coefficients from the Fresnel reflection coefficients for a single interface, they will be denoted as R. For a single film the reflection coefficients become:

$$R^s = \frac{r_{01}^s + r_{12}^s e^{-i2\beta}}{1 + r_{01}^s r_{12}^s e^{-i2\beta}} \tag{6.7}$$

$$R^p = \frac{r_{01}^p + r_{12}^p e^{-i2\beta}}{1 + r_{01}^p r_{12}^p e^{-i\beta}} \tag{6.8}$$

where β is defined as:

$$\beta = \frac{2\pi d N_1 \cos\phi_1}{\lambda}, \tag{6.9}$$

d is the thickness of the thin film layer, and λ is the wavelength of light in free space.

For dielectric films, k = 0 (i.e. the refractive index is real) and the reflection coefficients are real. Figure 6.3 shows the reflection coefficients for a dielectric film, shown here for TiO_2, evaluated as a function of the angle of incidence. The second plot is the reflectance of the material, where reflectance is the ratio of total outgoing intensity to the total incoming intensity of light and is related to the reflection coefficient through $\Re = |R|^2$, where R may be that of either the p or s wave.

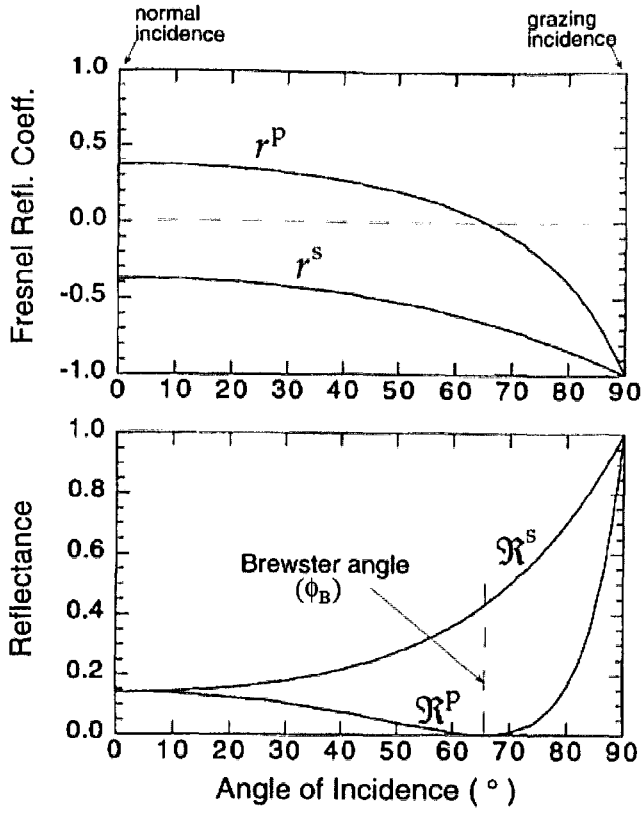

Figure 6.3: The Fresnel reflection coefficients for a dielectric film (top) and the resulting reflectance of the material (bottom) [68].

One notes that there is an angle of incidence where r^p passes through zero and $\Re^p$ goes to zero. The angle at which this occurs is known as the Brewster angle. At a dielectric interface it may be determined through:

$$\tan \phi_B = n_1/n_0 \tag{6.10}$$

Physically this angle is important to ellipsometry because it is the angle at which the phase shift of the p-wave on reflection goes abruptly from 0 to 180°. In non-dielectric materials the value of k is non-zero, and hence the Fresnel coefficients are complex and there is no case where the reflectance goes to zero. However, at the Brewster angle the reflectance will go through a minimum. In addition the phase shift of the p-wave is not abrupt but rather gradual at this angle. The value of the phase shift at this angle is 90°. In multiple layer materials a different quantity known as the pseudo-Brewster angle is used. It is analogous to the Brewster angle, however, it is related to the total reflection coefficient of the multilayer stack. The importance of the Brewster angle in ellipsometry will be discussed shortly.

Light incident on a sample may be arbitrarily polarized, with the s and p waves typically not being in phase (although in a typical ellipsometry experiment this polarization is known). After reflection each of the waves may undergo a phase change which is not necessarily the same for both waves. The fundamental equation of ellipsometry is given by the ratio of the of the total reflection coefficients as

$$\rho = \frac{R^p}{R^s} = \tan \Psi e^{i\Delta} \tag{6.11}$$

where $\tan \Psi$ is defined as the ratio of the amplitudes of R^p and R^s, and Δ is defined as the phase shift induced by reflection, or as the difference between the difference of the phases of the s and p-waves before and after reflection. Ψ and Δ are often referred to as the ellipsometric angles and are the values measured by an ellipsometer.

Figure 6.4 shows a plot of Ψ and Δ values for a glass film as a function of the angle of incidence [69]. The value of delta goes from 180 to 0° at the Brewster angle of the material. At the Brewster angle ellipsometry is most sensitive to the material properties. In practice the angle of incidence is typically fixed at an angle slightly above the Brewster angle.

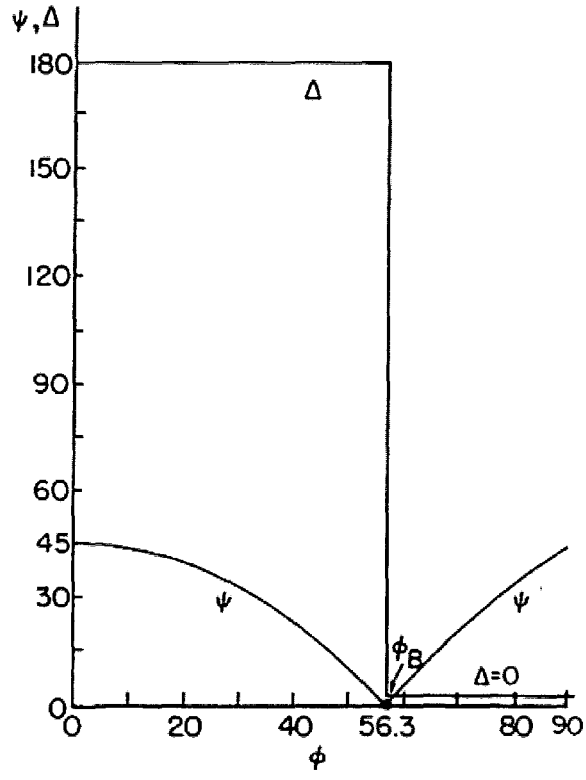

Figure 6.4: The ellipsometric angles, Ψ and Δ, for an air-glass interface at $\lambda = 546nm$ [69].

This treatment provides the necessary basis to understand ellipsometry [68, 70]. For the keen reader a more rigorous review of the fundamentals of ellipsometry and polarized light is given by Azzam and Bashara [69].

6.1.1 Ellipsometers

Figure 6.5 illustrates a basic ellipsometry configuration. Depending on the ellipsometer a compensator may or may not be used in the setup and the arrangement of the components often varies, but the basic operation principles all revolve around an arrangement of this sort.

In the following subsections some of the more common types of ellipsometers and

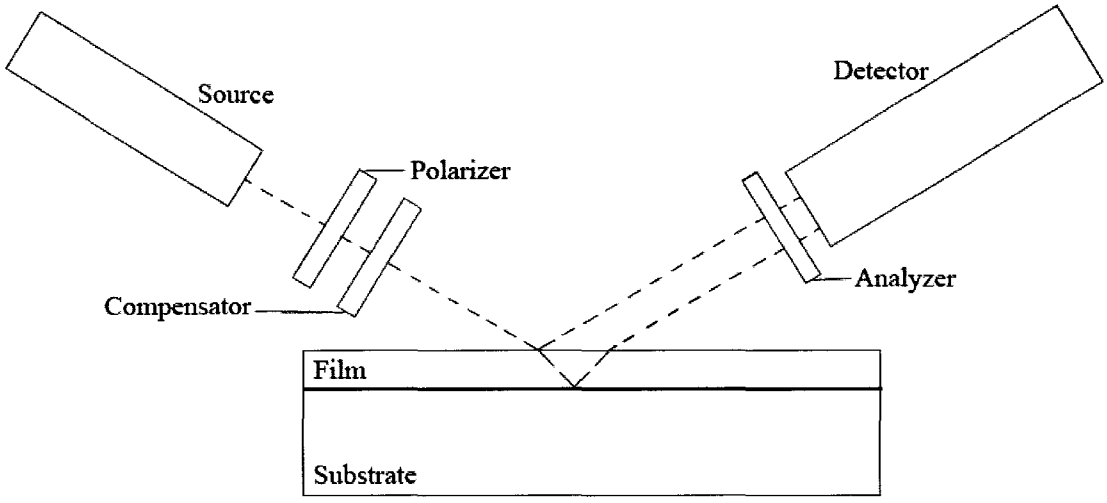

Figure 6.5: Basic schematic of an ellipsometer.

the details of their operation will be reviewed.

The Null Ellipsometer

The most basic ellipsometer type is a null ellipsometer, which uses the setup shown in Figure 6.5. In a null ellipsometer light from the source passes through the polarizer and compensator, strikes the sample, and then passes through the analyzer to the detector. The position of the polarizer and the analyzer are adjusted in order to completely eliminate any signal detection, that is to "null" the signal, hence the name null ellipsometer. This occurs when light reflected from the sample is linearly polarized at an angle perpendicular to that of the analyzer. To achieve a linear polarization at the analyzer, the compensator must provide a phase delay between the s and p waves that exactly compensates for the optical retardation that occurs from the combined reflections within the film, resulting in s and p polarizations that are in phase (linear polarization). In order to simplify the analysis the compensator is typically fixed at an angle of 45°, and the polarizer and analyzer angles, P and A, respectively, are restricted to two zones:

$$Zone\ 1 : -45° < P_1 < 135°, 0° < A_1 < 90° \tag{6.12}$$

$$Zone\ 2 : -135° < P_2 < 45°, -90° < A_2 < 0°. \tag{6.13}$$

In practice an average of the two measurements yields better results. In order to determine the ellipsometric angles from these measurements one first considers that the amplitudes of both polarizations are equal prior to reflection, therefore the ratio of amplitudes, $\tan\Psi$, after reflection is related to the tangent of the analyzer angle. The value of Δ is related to the angle of the polarizer. The angles P and A then allow for determination of the ellipsometric angles through the relations [70]:

$$Zone\ 1 : \Delta_1 = 270° - P_1;\ \Psi_1 = A_1 \tag{6.14}$$

and

$$Zone\ 2 : \Delta_2 = 90° - 2P_2;\ \Psi_2 = -A_2 \tag{6.15}$$

Rotating Component Ellipsometers

Another form of ellipsometry is to use a rotating component scheme which allows someone to exploit the advantages of microprocessors in order to speed up the measurement process. The rotating component is typically either the polarizer or analyzer, and rotates continuously throughout the entire measurement process. In a rotating null ellipsometer the polarizer and analyzer alternate their rotations until the actual null point, and not just a local minimum, is found.

Another rotating scheme fixes the polarizer and rotates the analyzer. The detector measures the output intensity as a function of time as the analyzer rotates as:

$$I(t) = I_0[1 + \alpha\cos 2\omega t + \beta\sin 2\omega t] \tag{6.16}$$

where I_0 is the average intensity of the detected signal, which is typically the DC offset of the detector, α and β are the Fourier coefficients of the signal, and ω is the angular

frequency of the analyzer. The Fourier coefficients are related to the ellipsometric angles through:

$$\alpha = -\cos 2\Psi \tag{6.17}$$

and

$$\beta = \sin 2\Psi \cos \Delta, \tag{6.18}$$

assuming that the polarizer was fixed at an angle of 45° with respect to the azimuth, which is typical for most rotating analyzer single wavelength ellipsometers [68]. These relations are then inverted to give:

$$\cos \Delta = \pm \sqrt{\frac{\beta^2}{1-\alpha^2}} \tag{6.19}$$

$$\tan \Psi = \sqrt{\frac{1+\alpha}{1-\alpha}} \tag{6.20}$$

Depending on whether or not a quarter wavelength plate compensator was used the value of Δ may have to be adjusted by $+90°$. Often a removable quarter wave plate is used to provide two measurements, improving accuracy and resolving the $\pm$ in Equation 6.19 [70].

Spectroscopic Ellipsometers

Spectroscopic ellipsometers (SEs) allow for the determination of optical constants over a range of wavelengths. One type of spectroscopic ellipsometer makes use of the rotating analyzer scheme, however, a broadband light source is used along with a monochromator in order to switch the wavelength of measurement. For a SE the polarizer angle is not set at a single value. Rather a calibration sample is measured and the polarizer adjusts in order to minimize the signal to noise ratio [68]. When the polarizer angle, P, is varied Equations 6.17 and 6.18 become

$$\alpha = \frac{\tan^2 \Psi - \tan^2 P}{\tan^2 \Psi + \tan^2 P} \tag{6.21}$$

and

$$\beta = \frac{2 \tan \Psi \cos \Delta \tan P}{\tan^2 \Psi + \tan^2 P} \tag{6.22}$$

respectively [71].

6.1.2 Ellipsometric Modeling

Ellipsometers measure the values of Ψ and Δ. In order to obtain the desired materials properties and information such as thickness these parameters must be used along with an assumed model. In order to properly extract the optical constants of a film it is necessary to develop ellipsometric models that account for the effects of multiple layers and structures which may be present within the film, as the measured ellipsometric angles will be affected by their presence. In this section two ellipsometric models, which were used in this work, are discussed. Additionally, the Kramers-Kronig relations, which relate the real and imaginary parts of the refractive index, are introduced.

Typically, ellipsometric models are evaluated based on a goodness of fit parameter. The structure of the model is initially defined to mimic the sample structure to the best of the modeler's knowledge. Based on the model the program then generates a set of data points which are compared to the experimentally measured points and evaluated using the goodness of fit parameter. One such method of evaluating the goodness of fit is the mean-squared error, MSE, which is determined through:

$$MSE = \frac{1}{2N-M}\sum_{i=1}^{N}\left[\left(\frac{\Psi_i^{mod}-\Psi_i^{exp}}{\sigma_{\Psi,i}^{exp}}\right)^2+\left(\frac{\Delta_i^{mod}-\Delta_i^{exp}}{\sigma_{\Delta,i}^{exp}}\right)^2\right]=\frac{1}{2N-M}\chi^2 \quad (6.23)$$

where Ψ and Δ are the ellipsometric angles, σ is the standard deviation of the experimental data points, N is the number of (Ψ, Δ) pairs, and M is the number of variable parameters in the model. During the modeling process the software may be set to fit various parameters of the model, such as the thickness of the film. The program will then recursively adjust the fit parameters in order to reduce the MSE [20, 72, 73].

It is important to note that a good MSE value is not always indicative that a good set of data has been obtained through the fitting process. When the software adjusts the model fit parameters to obtain results that agree with the experimental data, it will do so regardless of whether the model is good or not. One should therefore examine the results obtained from the fitting process. If one parameter, such as thickness, has been greatly modified this can serve as an indicator that the model being used is a poor one. It is therefore necessary to that one have some

basic knowledge about the films being measured in order to determine the actual film properties. Additionally, by fitting the model parameters to a series of data sets, each obtained at a different angle of incidence, the accuracy of the Ψ and Δ values determined from modeling can be improved, and the probability of obtaining erroneous data decreases.

The Cauchy Dispersion Model

The Cauchy dispersion model is typically applied to dielectric materials, where the bandgap of the material is large and the resonant frequency of the material is deep into the UV range. The model is only valid in the visible and NIR range where the refractive index of the material decreases slightly with increased wavelength. The Cauchy dispersion relation is given by:

$$n = n_0 + \frac{n_1}{\lambda^2} + \frac{n_2}{\lambda^4} \tag{6.24}$$

where n_0, n_1, and n_2 are the Cauchy parameters. For dielectrics the value of k is assumed to be zero. For semiconducting materials the value of k is typically nonzero and a similar treatment can be used for the extinction coefficient over a similar range. That is to say,

$$k = k_0 + \frac{k_1}{\lambda^2} + \frac{k_2}{\lambda^4} \tag{6.25}$$

where k_0, k_1, and k_2 are the Cauchy extinction parameters [68].

The Sellmeier Model

The Sellmeier model is another dispersion relation similar to the Cauchy model. The Sellmeier relations for n and k are given through the equations

$$n^2 = 1 + \frac{A}{1 + B^2/\lambda^2} \tag{6.26}$$

and

$$k = \frac{C}{nD\lambda + E/\lambda + 1/\lambda^3} \tag{6.27}$$

where A, B, C, D, and E are the Sellmeier parameters [74]. As with the Cauchy model the range of applicability of this model is limited to the visible and NIR.

6.1.3 Kramers-Kronig Relations and Ellipsometric Modeling

The refractive index and extinction coefficient of a material are in fact not independent of each other. The two values are related through the Kramers-Kronig relations. The relationship between n and k, as a function of energy, is given by:

$$n(E) - 1 = \frac{2}{\pi} P \int_0^\infty \frac{E' k(E')}{E'^2 - E^2} dE' \tag{6.28}$$

where P is the Cauchy principal value of the integral taken at $E' = E$ [68]. An alternate from of the equation is typically presented in terms of the dielectric constant, ϵ ($\epsilon = \epsilon' + i\epsilon''$), of the material, where:

$$\epsilon = N^2 \tag{6.29}$$

and

$$\epsilon' = n^2 + k^2 \tag{6.30}$$

$$\epsilon'' = 2nk \tag{6.31}$$

The Kramers-Kronig relations then become:

$$\epsilon'(E) = 1 + \frac{2}{\pi} P \int_0^\infty \frac{E' \epsilon''(E')}{E'^2 - E^2} dE' \tag{6.32}$$

and its inverse

$$\epsilon''(E) = -\frac{2E}{\pi} P \int_0^\infty \frac{\epsilon'(E')}{E'^2 - E^2} dE' \tag{6.33}$$

An inverse relation for Equation 6.28 does not automatically follow as it does for Equation 6.32 [75].

From the above equations when the imaginary part of N is known or either of the real and imaginary parts of ϵ are known over the entire energy range their counterparts may be determined. Note that unless a suitably large energy range is used these integrals are not accurate.

In spectroscopic ellipsometry there exist many physical models to derive the values of n and k from the measured ellipsometric values. While many of these models provide a good determination of the optical constants within a given, finite, range they

are not Kramers-Kronig consistent unless the above relations are satisfied. However, because only a finite energy, or wavelength, range is measured the models typically provide satisfactory results. The models used in this work, the Cauchy and Sellmeier models, are not Kramers-Kronig consistent. The development of models that are both Kramers-Kronig consistent and account for the presence of different phases within the films through effective medium theories are the subject of current research efforts [20]. The Lorentz oscillator, an example of a Kramers-Kronig consistent model, may be found in Tompkins and McGahan [68].

6.2 Photoluminescence Characterization

Photoluminescence is a relatively simple technique where a laser is used to excite electrons to higher energy states, creating electron-hole pairs which then recombine, releasing a photon with a wavelength characteristic of the band structure of the film. Figure 6.6 illustrates the PL setup used to analyze the films discussed in this thesis.

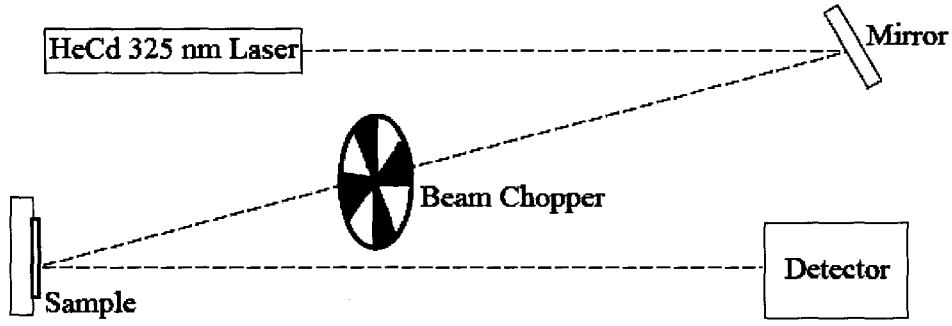

Figure 6.6: A schematic illustrating the PL measurement setup at McMaster.

Photon emission during PL processes is characteristic of the intrinsic electronic structure of the material. In addition, electronic transitions may occur at impurities or defects within the material. In impure materials these defects can serve as the primary source of emission.

6.2.1 Principles of Photoluminescence in Semiconductor Materials

The technique of photoluminescence is not one typically applied to Si-based materials due its inefficiency in terms of emission, an issue that has been discussed in previous chapters. In order for this chapter to stand alone it is necessary to review some of the concepts of Chapter 3 before going into more detail. Figure 6.7, which shows a less detailed version of the band structure of Si and GaAs materials than those previously shown, will be used to give a brief review of the properties of semiconductors necessary to understand the PL process [64].

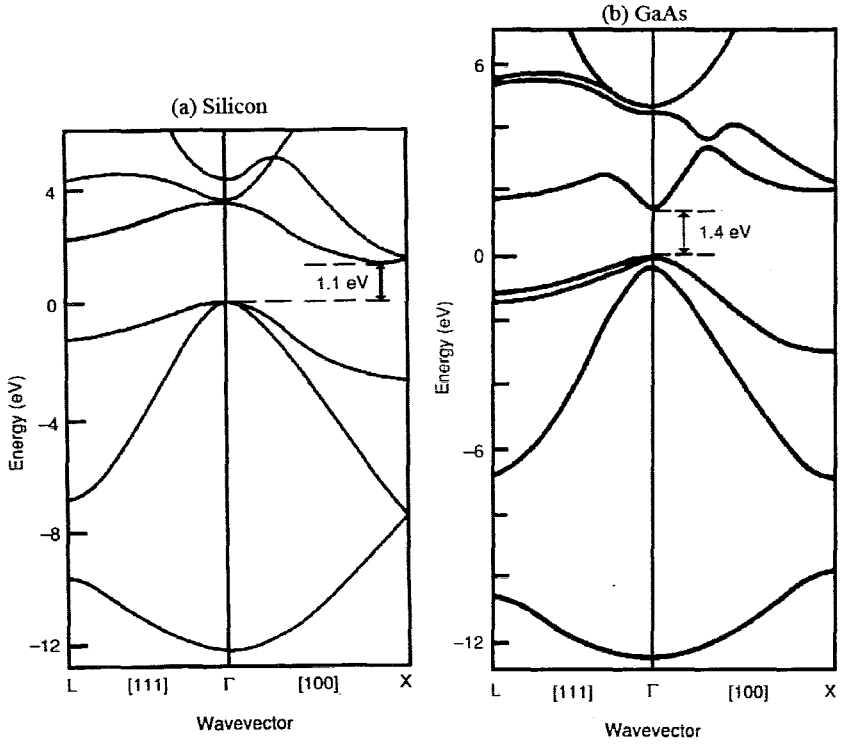

Figure 6.7: Examples of the electronic structure of semiconductor materials: (a) the indirect bandgap of silicon and (b) the direct bandgap of GaAs [64].

The bandgap of a material, E_G, is defined as the difference in energy between the lowest point of the conduction band and the highest point of the valence band. As discussed in Chapter 3, in GaAs both these points lie at the Γ point, making GaAs

a direct gap material. Si, as stated a number of times, is an indirect gap material, with its valence band edge lying at the Γ point, while its conduction band edge lies near the **X** point.

A photon with energy equal to or exceeding that of the bandgap is able to excite a valence electron across the bandgap. Impurities in the material may have energy levels within the bandgap and the absorption process can also excite transitions to and from impurity centers. In an indirect bandgap material such as Si an additional factor must be considered in the excitation process related to the change in momentum required for the excited electron to move from the Γ point to the **X** point. Momentum changes, such as this, are obtained through electron-phonon interactions.

Information on the material is actually obtained when this excited electron decays back to its initial state. This return process will cause the emission of a photon with energy equal to the difference between the excited and initial states, provided that the decay process is radiative. Measuring the emission spectrum with a spectrometer will show the presence of many emission peaks, as radiative transitions related to decay from the bandgap as well as other excited states (which may be related to defects, impurities, and dopants) present in the film will occur. These emission peaks then serve as a characteristic identifier of the types of structures and impurities that produced them [75, 76].

The need for phonon interactions is the first limiting factor in Si luminescence, as it makes both the absorption and emission process less probable. Because of this decreased probability of transition the excitation lifetime is typically quite long in indirect gap semiconductors, and in the case of Si competing non-radiative recombination methods, such as the Auger process and free-carrier effects, limit the probability of a radiative decay.

6.2.2 Quantum Confined Luminescence

Luminescence from Si nanocrystals is a result of quantum confinement effects, similar in nature to the enhanced luminescence of quantum wells, wires and dots in III-V structures. In Chapter 3 the basic details of quantum confinement related to

silicon nanocrystals were considered, here the general effects of reduced dimensions and quantum confinement on luminescence are presented.

Consider the case of confinement in one dimension, the quantum well, which is a commonly employed scheme in III-V based laser structures. Because of this, the AlGaAs-GaAs quantum well will be considered. By having a thin layer of a material, GaAs, sandwiched between two materials with larger energy gaps, AlGaAs, a quantum well is created as shown in Figure 6.8 [77].

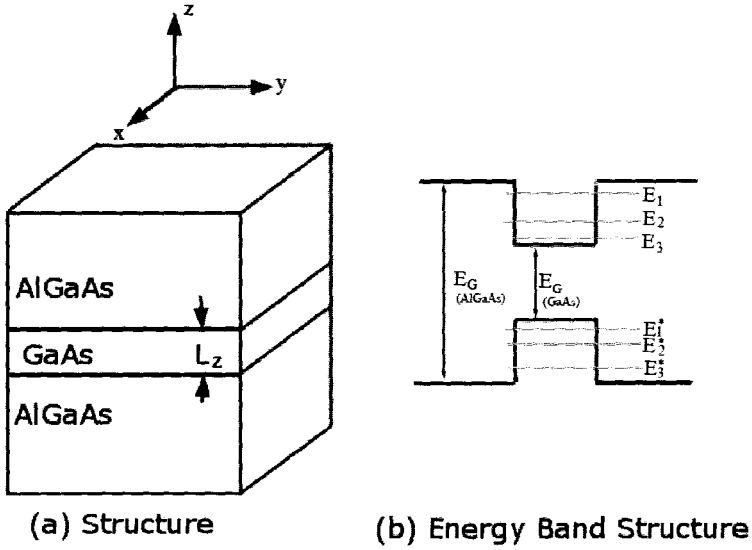

Figure 6.8: An example of a quantum well. (a) The structure of the well. (b) The bandgap structure of the well. Confinement leads to quantized energy levels in the confined region. The * is used to distinguish the quantized energy levels for holes in the valence band from those of electrons in the conduction band [77].

Solving for the energy levels within this well can be done by considering the problem in an equivalent manner to the potential well, which is treated in introductory quantum mechanics courses. The AlGaAs layers serve to confine the electron within the well and the energy states that the electron can occupy become quantized, with energies given by:

$$E_n = \frac{\hbar^2 \pi^2}{2m_e^*} \left(\frac{n_z}{L_Z} \right)^2 \tag{6.34}$$

where m_e^* is the effective mass of the electron, L is the width of the well, and n is an

In quantum confinement the bandgap is not the only consideration, one must also consider how the density of states, $\rho(E)$, is modified by confinement, as this is an equally important factor in the confinement process. Simply put the density of states is the number of available states per unit volume per unit energy. For structures with confinement in 0(bulk), 1(quantum well), 2(quantum wire), and 3(quantum dot) dimensions the densities of states are given by:

$$\rho_{Bulk}(E) = \frac{1}{2\pi^2}\left(\frac{2m_e^*}{\hbar^2}\right)^{3/2} E^{1/2} \tag{6.37}$$

$$\rho_{QWell}(E) = \frac{m_e^*}{\pi\hbar^2}\Sigma_{n_z}\Theta(E - E_{n_z}) \tag{6.38}$$

$$\rho_{QWire}(E) = \frac{1}{\pi}\left(\frac{m_e^*}{\hbar^2}\right)^{1/2}\Sigma_{n_y n_z}\frac{1}{E^{1/2}}\Theta(E - E_{n_y n_z}) \tag{6.39}$$

and

$$\rho_{QDot}(E) = \delta(E - E_{n_x n_y n_z}) \tag{6.40}$$

where Θ is the Heavyside function and E_i, where i represents the confinement that may result in 1, 2, or 3 dimensions, is the confinement energy of the given discrete state specified by the indicated subscripts. For simplicity the introduction of degeneracy has been avoided in this discussion. Figure 6.10 shows how the density of states, $\rho(E)$, varies as the dimensions of the material go from 3 to 0, or equivalently go from bulk to confinement in 3 dimensions [78, 79].

The reduction in the density of states as one goes from bulk to 0D materials leads to single energy atomic-like levels, which can be used to produce higher gain for laser operation. Because of the atomic-like nature of the 0D density of states, quantum dots are often called artificial atoms.

integer ($n_z = 1, 2, 3 \ldots$). Equivalently, the energy levels for holes within the valence band also become quantized, as shown in Figure 6.8(b), where the quantized energy levels of the holes are indicated by the *. This quantization of the energy levels leads to an effective widening of the bandgap in the material, causing radiative emissions to be blueshifted from that of the bulk material bandgap.

If the structure is confined in two dimensions, say z and y, a quantum wire is produced. The energy levels within this 1-dimensional system are given by:

$$E_{n_x n_y} = \frac{\hbar^2 \pi^2}{2m_e^*} \left(\frac{n_y}{L_y} + \frac{n_z}{L_z} \right)^2 \tag{6.35}$$

Carrying this one step further, the energies for a quantum dot, which is confined in three dimensions become:

$$E_{n_x n_y n_z} = \frac{\hbar^2 \pi^2}{2m_e^*} \left(\frac{n_x}{L_x} + \frac{n_y}{L_y} + \frac{n_z}{L_z} \right)^2 \tag{6.36}$$

Figure 6.9 illustrates the structure of quantum wires and dots.

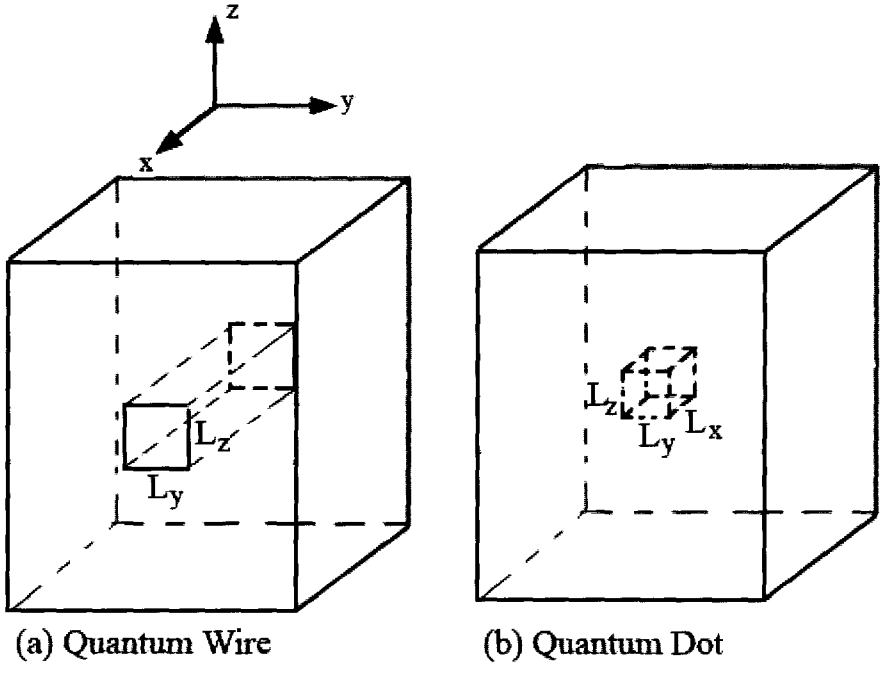

Figure 6.9: The structure of (a) a quantum wire and (b) a quantum dot.

In quantum confinement the bandgap is not the only consideration, one must also consider how the density of states, $\rho(E)$, is modified by confinement, as this is an equally important factor in the confinement process. Simply put the density of states is the number of available states per unit volume per unit energy. For structures with confinement in 0(bulk), 1(quantum well), 2(quantum wire), and 3(quantum dot) dimensions the densities of states are given by:

$$\rho_{Bulk}(E) = \frac{1}{2\pi^2}\left(\frac{2m_e^*}{\hbar^2}\right)^{3/2} E^{1/2} \tag{6.37}$$

$$\rho_{QWell}(E) = \frac{m_e^*}{\pi\hbar^2}\Sigma_{n_z}\Theta(E - E_{n_z}) \tag{6.38}$$

$$\rho_{QWire}(E) = \frac{1}{\pi}\left(\frac{m_e^*}{\hbar^2}\right)^{1/2} \Sigma_{n_y n_z}\frac{1}{E^{1/2}}\Theta(E - E_{n_y n_z}) \tag{6.39}$$

and

$$\rho_{QDot}(E) = \delta(E - E_{n_x n_y n_z}) \tag{6.40}$$

where Θ is the Heavyside function and E_i, where i represents the confinement that may result in 1, 2, or 3 dimensions, is the confinement energy of the given discrete state specified by the indicated subscripts. For simplicity the introduction of degeneracy has been avoided in this discussion. Figure 6.10 shows how the density of states, $\rho(E)$, varies as the dimensions of the material go from 3 to 0, or equivalently go from bulk to confinement in 3 dimensions [78, 79].

The reduction in the density of states as one goes from bulk to 0D materials leads to single energy atomic-like levels, which can be used to produce higher gain for laser operation. Because of the atomic-like nature of the 0D density of states, quantum dots are often called artificial atoms.

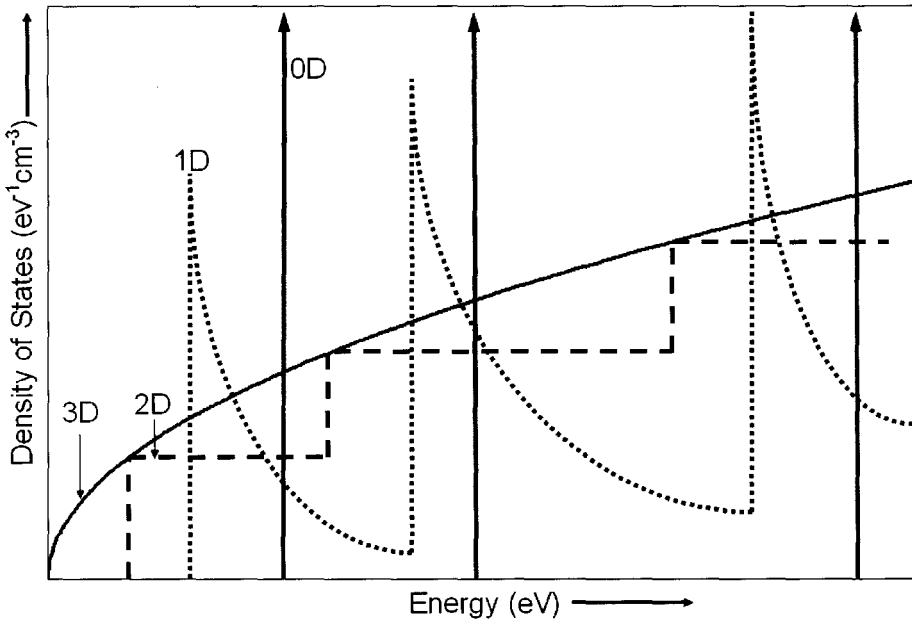

Figure 6.10: The effects of confinement on the density of states

Chapter 7

Experimental Details

The following sections outline the details of the major experimental parts of this research, including the calibration of the deposition system, ion beam analysis experiments, FTIR spectroscopy, ellipsometry, and photoluminescence. In addition to these experiments some analysis of the films was done through the use of atomic force microscopy, scanning electron microscopy and transmission electron microscopy. The results from these imaging techniques are used primarily to clearly illustrate some of the concepts described in the results section. Details of the experimental setups for these systems will not be discussed here.

7.1 Experimental Deposition Conditions

The films were deposited using the ECR-PECVD system that has been discussed. A constant chamber pressure of 2.4 mTorr was maintained for the initial depositions. The currents in the upper and lower magnets were set to 180A and 115A, respectively. A microwave power of 500 $\pm$ 5 W with a reflected power of 5-7 W was used to excite the plasma. The substrate heater was set to a temperature of 350 °C, resulting in a substrate surface temperature of 120 °C.

The plasma gas precursors were 10% O_2 in Ar and Ar gases. The silicon precursor, silane, was delivered in a mixture of 30% SiH_4 in Ar. Table 7.1 gives the deposition parameters for a set of samples used to determine a calibration curve for the system.

Sample	O_2+Ar Flow Rate [sccm]	Ar Flow Rate [sccm]	Deposition Time [min]
C9	34.6	14.4	16:30
C10	34.5	14.7	12:00
C11	31.0	17.9	12:00
C12	27.6	19.1	12:00
C13	24.2	23.1	12:15
C14	20.7	25.4	12:00
C15	17.3	28.6	12:00
C16	13.8	30.7	12:00
C17	10.4	34.3	16:00
C18	6.9	37.1	17:00
C19	3.5	40.0	18:00
C20	0.0	44.3	13:00

Table 7.1: Deposition parameters for a set of silicon oxide samples used to establish a calibration curve for the system.

The silane flow was kept constant at 6.9 sccm during these depositions. During the deposition process the gas flow settings used by the system must be corrected by precursor specific calibration factors in order to present the data in units of sccm, as has been done here. For reproducibility purposes the experimental settings may be retrieved by noting that the gas flow rates have been corrected by factors of 0.62, 0.69, and 1.428 for the SiH_4 in Ar, 10% O_2 in Ar, and Ar gases, respectively. Following the determination of the calibration curve, samples were deposited to achieve specific compositions which will be referenced in terms of the percent of silicon contained within the sample.

Three types of substrates were used during the depositions in order to facilitate the various characterization methods; single side polished silicon, double side polished silicon, and carbon.

Additionally, a set of samples was deposited without the addition of Ar to maintain chamber pressure. This set of depositions was done using an increased silane flow of 15.5 sccm (16.7 sccm for sample SRSO8). It is important to note that in the absence of an Ar flow *a*-Si films cannot be deposited, therefore, the full range of compositions from SiO_2 to *a*-Si cannot be achieved. The deposition parameters for this set of films

Sample	O_2/Ar Flow Rate [sccm]	Deposition Time [min]
SRSO1	34.6	5:30
SRSO2	38.0	5:30
SRSO3	41.5	5:30
SRSO4	44.9	5:30
SRSO5	48.3	5:30
SRSO6	51.8	5:30
SRSO7	55.3	5:30
SRSO8	55.3	5:30

Table 7.2: Deposition parameters for a set of silicon oxide samples deposited without Ar.

is given in Table 7.2.

7.2 Annealing Studies

Films were annealed in a quartz tube furnace at temperatures from 400 to 1200°C for times up to 120 minutes in an Ar ambient environment. The setup contains an elastomer seal with a slide in/slide out quartz boat, within which the samples are situated. Additionally, a bubbler is used in the setup to prevent air from backstreaming into the annealing area.

7.3 RBS and ERD Experiments

RBS experiments were done at the University of Western Ontario (UWO) using a $^4He^+$ ion beam. Beam energies of 1.5-2.0 MeV were used. A reference sample containing a known concentration of Bi implanted in Si was measured allowing for determination of the solid angle of the detector.

ERD experiments were also conducted at the UWO for some samples. A reference sample of mylar was used to calibrate the system for each ERD run.

7.4 FTIR Experiments

FTIR experiments were done using an ABBomen Work*IR* 100 FTIR spectrometer. Scans were done from 400 to 4000 cm^{-1} with a resolution of 8 cm^{-1}.

Samples were deposited onto high resistivity, low impurity, double side polished silicon substrates. The use of said substrates minimizes the effects of impurity artifacts and free carrier absorption in the FTIR spectra.

In order to resolve FTIR features related to the films and not the substrates a reference sample was cleaved from each substrate prior to deposition and the reference spectra were subtracted from the measured absorbance spectra.

Peaks were identified through comparison with known peaks related to Si-based bonds.

7.5 Ellipsometric Experiments

Ellipsometry was done using two different ellipsometers. The first was a single wavelength Philips PZ2000 ellipsometer operating using a HeNe laser at 632.8 nm. The second was a J. A. Woollam M-44 NIR variable angle spectroscopic ellipsometer operating from 600 to 1100 nm. Modeling of the films was done using the Sellmeier and Cauchy models discussed in section 6.1.2. The actual setup of the model is discussed further in the following chapter.

7.6 PL Experiments

PL experiments were done at room temperature using the setup shown in Figure 6.6. For each sample a dark, or background, spectrum was obtained by taking a measurement with the laser off, after which the PL spectrum of the sample was measured. The actual PL spectrum of the sample alone is then determined by subtracting the dark spectrum from the measured spectrum. An Ocean Optics fibre optic spectrometer was used to collect the spectrum. Second order laser lines were eliminated from the spectrum through the use of a long pass filter.

Chapter 8

Results and Discussion

8.1 Film Compositions and SWE Measurements of the As-Deposited Films

8.1.1 System Calibration and Film Compositions

Figure 8.1 shows a sample RBS spectrum for films deposited on C substrates. Quantitative analysis of the RBS data and the determination of atomic concentrations has previously been described by Irving [35] and Tan [20]. The atomic concentrations of Si, O and Ar in these films, as determined through the RBS experiments, are shown in Figure 8.2 as a function of the molar ratio of oxygen to silicon (x in SiO_x).

Table 8.1 shows the indices of refraction and thicknesses of the calibration samples, as determined by SWE, as well as the growth rates.

The refractive index of sample C18 could not be determined through single wavelength ellipsometry. This was attributed to a difficulty in ellipsometry that arises when Δ and Ψ have values that fall on ellipsometric trajectory points where multiple curves overlap. In this case any small variations in either value cause large fluctuations in the values of the refractive index and thickness and reliable results are difficult to obtain. The trend of the refractive index with increased Si content is readily apparent even without this data point and one sees that a large range of optical constants can be covered, corresponding to a large range of compositions. It

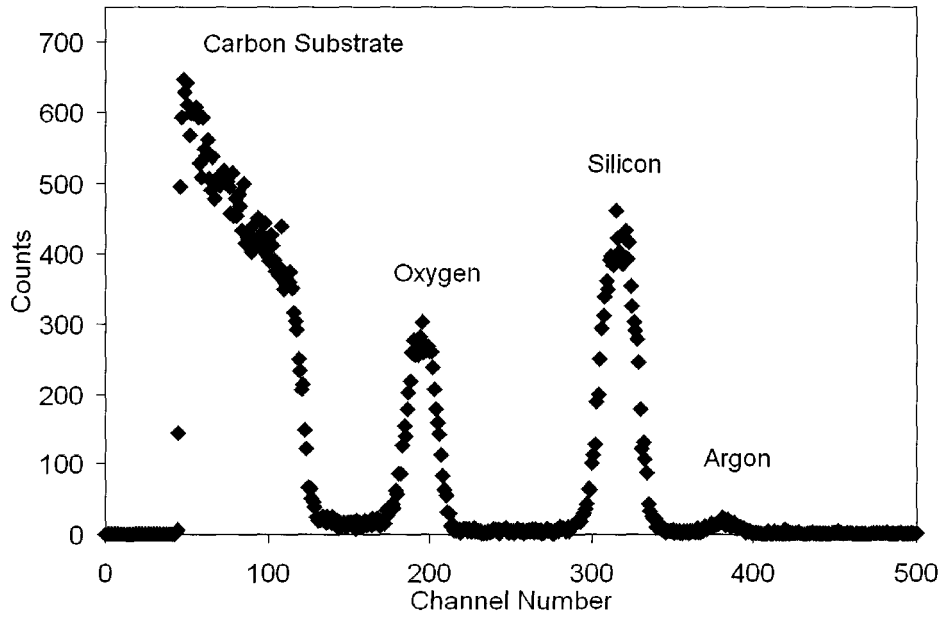

Figure 8.1: The RBS spectrum for sample C13, deposited unto a carbon substrate. The carbon substrate allows for the resolution of the Si and O peaks.

is noted that even in the absence of an O source gas flow some O was detected in the deposited film. This is likely the result of oxidation of the sample after removal from the deposition chamber. The O related peak for this film was near the detection limits of the system and only a small O signal was seen. Because this signal may arise from surface oxidation and not O within the film quantification of this O related peak overestimates the actual O concentration of the film. For films deposited under these conditions the bulk is considered to be *a*-Si for results presented later in this section.

The Ar concentration in these films is approximately constant with the exception of films with compositions near *a*-Si and SiO_2. In the case of films with compositions near SiO_2 it can be seen that multiple settings lead to films having approximately the same compositions, meaning that there is an overpressure of O relative to Si compared to that needed in order to cause SiO_2 growth. This overpressure of oxygen at the film surface may result in the formation of excess void space as film growth proceeds. When films with compositions near *a*-Si are grown one can see that the

Sample	x in SiO_x	Index of Refraction	Thickness [Å]	Growth Rate [Å/min]
C9	1.96	1.48	721	44
C10	1.94	1.47	698	58
C11	1.94	1.48	671	56
C12	1.95	1.48	675	56
C13	1.80	1.55	712	58
C14	1.19	1.80	675	56
C15	1.04	1.91	705	59
C16	0.80	2.07	709	59
C17	0.57	2.32	965	60
C18	0.32	N/A	N/A	N/A
C19	0.16	2.96	1198	67
C20	0.13	4.18	875	67

Table 8.1: Refractive indices, thicknesses, and growth rates of the calibration set of samples deposited at a constant chamber pressure, obtained by ellipsometric measurements.

growth rate increases. This is easily explained by considering that more Ar is available to disassociate the silane molecules without bonding to the Si, producing excess Si which can readily bond to the surface. The increased growth rate at a low temperature causes a more disordered structure, where an increased concentration of Ar can easily be incorporated into void space and interstitially.

When the films were deposited without a constant chamber pressure, i.e. with no additional Ar flow, the atomic concentrations shown in Figure 8.3 were achieved. The refractive index, thicknesses, and growth rates for these films are given in Table 8.2.

In this run of samples, the highest Si content achieved, for film SRSO1, was only 58% Si. In later depositions we were able to overcome this limit by increasing the microwave power during the deposition process. The optical properties of this subsequent set of films are discussed later in this chapter. Details of the variation of microwave power and its effects on the properties of the films are discussed in [80].

Comparing the two sets of samples the concentrations of Si and O within the films are approximately the same for a given composition, as opposed to both being reduced proportionally which would be indicative of decreased film densities. The

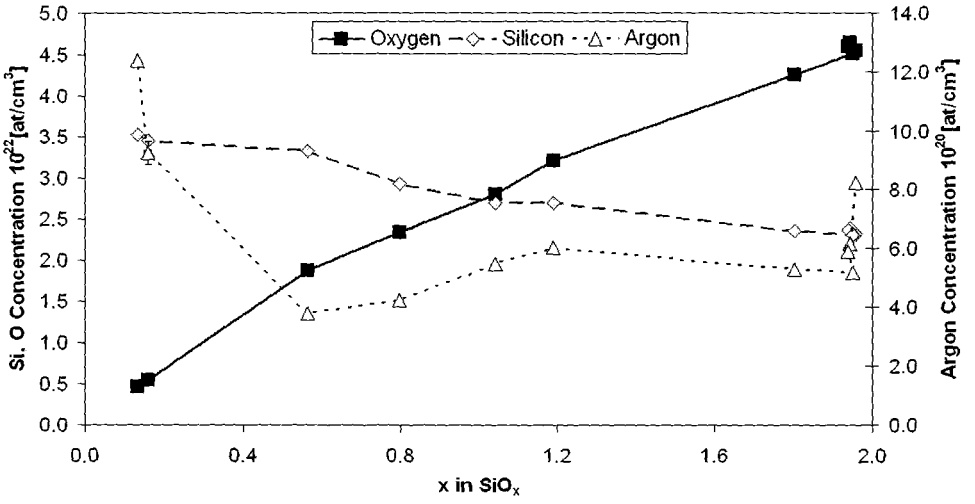

Figure 8.2: Atomic concentrations of Si, O, and Ar within films deposited at a constant chamber pressure, maintained using an Ar flow. The lines are provided as a guide to the eye only.

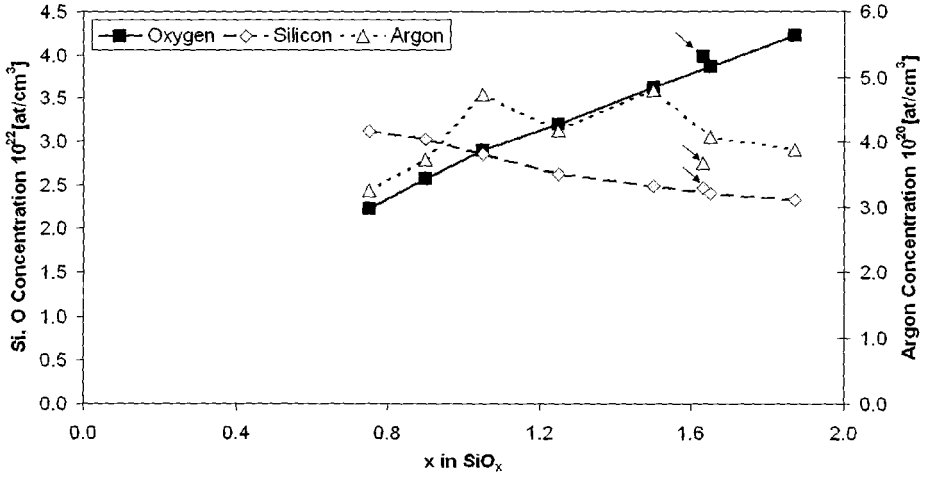

Figure 8.3: Atomic concentrations of Si, O, and Ar within films deposited without the use of an Ar gas to maintain chamber pressure. The Ar within the films comes from the O_2 + Ar and SiH_4 + Ar source gas mixtures. The arrows are used to distinguish sample SRSO8, which was deposited with an increased silane flow. The lines are provided as a guide to the eye only.

Sample	x in SiO_x	Index of Refraction	Thickness [Å]	Growth Rate [Å/min]
SRSO1	0.71	2.15	835	152
SRSO2	0.85	2.01	850	155
SRSO3	1.02	1.89	775	141
SRSO4	1.22	1.80	770	140
SRSO5	1.46	1.69	745	136
SRSO6	1.61	1.54	756	138
SRSO7	1.82	1.51	765	139
SRSO8	1.61	1.60	787	143

Table 8.2: Refractive indices, thicknesses, and growth rates of the calibration set of samples grown without an Ar gas flow to maintain chamber pressure, obtained by ellipsometric measurements.

Ar concentration is, however, seen to be significantly reduced for the films deposited without Ar. These films also do not show an increased Ar concentration as the composition approaches SiO_2, as was seen in for films deposited with Ar (Fig. 8.1). No evidence of Ar bonding was seen in any of these films (through FTIR analysis, discussed later in this chapter), although it is possible to produce Ar ions in the plasma region which could, in theory, be bound. Ar is therefore expected to be situated interstitially or within void space in these films. Because the Si and O concentrations did not show any change in the absence of Ar it is likely that a comparable amount of void space exists in both sets of films, with additional Ar being deposited into these spaces when an Ar gas is used.

A good agreement is seen for the refractive indices between the two sets of samples, with films having the same compositions having approximately the same refractive index, meaning that the densities of the films must be comparable and the use or absence of an Ar gas flow does not result in a change in the amount of void space in these films, which agrees with the discussion presented based on atomic concentrations of Si, O, and Ar. In the case of these measurements there is some margin of error, as only SWE was used. Spectroscopic ellipsometry has revealed that there is, in fact, some deviation in the refractive indices as films deposited without Ar show a slightly lower refractive index than those deposited with Ar, meaning there may be some variation in the densities of the films. Whether the presence of Ar in the films

influences the refractive index was not examined for this work.

The most significant differing feature is seen for the growth rates. For films deposited without Ar the silane flow was increased significantly in order to increase the collision probability between plasma and SiH_4 species. So long as there is sufficient gas flow and power within the plasma region to generate a good quality plasma the increased probability of collisions will rapidly increase the growth rates as more Si atoms will be available.

8.1.2 Effects of Annealing on Film Composition

For the calibration samples, the films were deposited onto C substrates, which allowed the Si and O peaks to be resolved (Fig. 8.1). For the samples that were subjected to annealing studies Si substrates were used. An RBS spectrum for one of these samples is shown in Figure 8.4. It is evident that the Si and O related peaks are situated upon a background Si signal resulting from the substrate, making the quantification of their concentrations difficult, as discussed in Chapter 4. Heavy Ion ERD analysis (HIERDA) would be an alternative ion beam analysis method which would allow one to avoid this problem in resolving the Si and O peaks in these films.

While the Si and O concentrations were not experimentally determined because of the aforementioned difficulties, the RBS spectra did allow for the analysis of the Ar concentration of these films, as the Ar scattering peak is located beyond the substrate signal. In addition to determining the Ar concentrations of the annealed films, ERD allowed for the analysis of the hydrogen content of said films.

Figure 8.5 shows the effects of annealing temperature for 60 minute anneals on the concentrations of Ar and H within these films. Concentrations for anneals above 1000°C approached the detection limits for the RBS and ERD systems, meaning that very little Ar and H remain in the films after high temperature annealing.

While the Si and O concentrations were not determined for the annealed films a comparison of the size and shape of the RBS peaks did not show significant changes. In the absence of more accurate experimental results, such as would be obtained by HIERDA, it has been assumed that the concentrations of Si and O remain constant

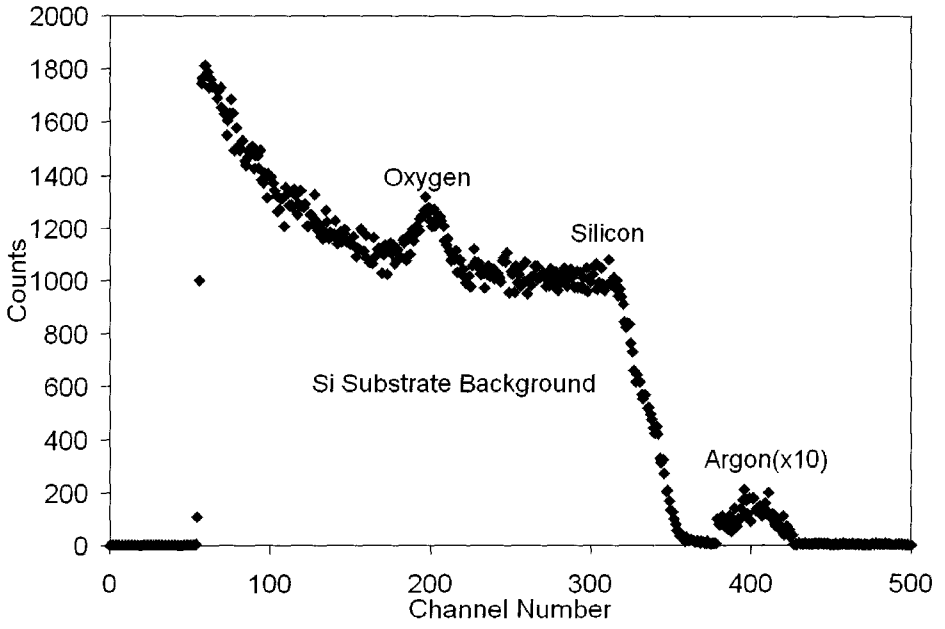

Figure 8.4: The RBS spectrum for an annealed sample deposited unto a silicon substrate. The Si and O peaks are situated upon the background spectrum of the Si substrate and are not clearly resolved. The Ar peak, however, lies beyond the Si substrate high energy end and is easily analyzed (recalling that increasing channel numbers correspond to increasing scattered atom energies).

after annealing treatments.

8.2 Film Bonding Structure

The FTIR spectra for a set of as-deposited samples having compositions of 34, 47, and 88% Si are shown in Figure 8.6, illustrating the variation in the IR signal as the films change in composition from near SiO_2 to *a*-Si:H.

The IR absorption peaks related to the Si-O based modes are clearly present in the films with 34 and 47% Si and the change in their shape and intensity as the films become more Si-rich is readily apparent, with the peaks being almost non-existent for the film with 88% Si. The relationship between film composition and the FTIR spectra is, therefore, readily apparent. The H related peaks show the opposite trend,

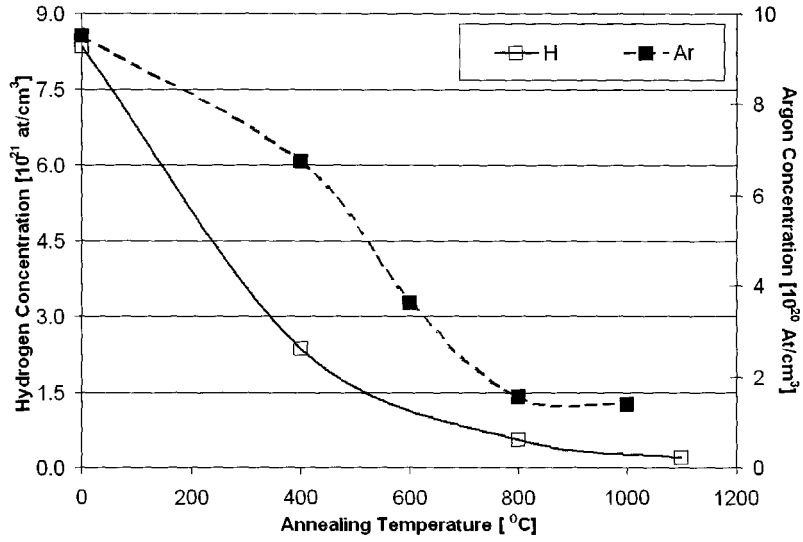

Figure 8.5: The variation of the concentrations of Ar and H in the films with increased anneal temperature. At high anneal temperatures the concentrations approached the detection limits of the RBS and ERD systems and only trace amounts of the elements are assumed to remain in the films.

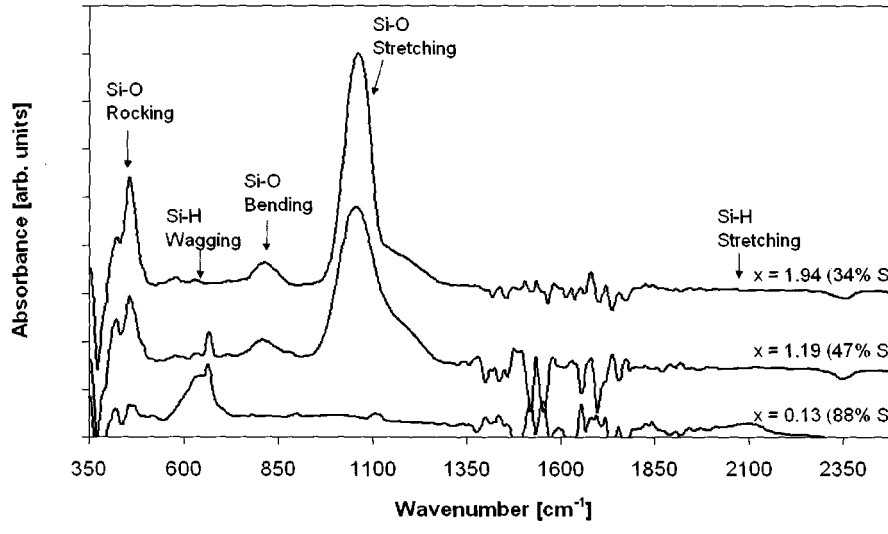

Figure 8.6: FTIR spectra of as-deposited samples having 34, 47, and 88% Si. The spectra have been shifted vertically for clarity.

with the peaks increasing in intensity as the films approach compositions of a-Si(:H). No significant OH peaks were observed, therefore, hydrogen is presumed to bond primarily with Si in these films. As discussed in Chapter 2 this bonding may occur either due to incomplete disassociation of the silane or through passivation of Si dangling bonds.

Samples with 42, 48, 51, and 67% Si were deposited and the effects of annealing on the FTIR peaks was analyzed. The evolution of the FTIR spectrum of a film with 42% Si with anneal temperature is shown in Figure 8.7. As the anneal temperature is increased the Si-O-Si stretching mode peak can be seen to increase in intensity and shift in position towards a value of 1080 cm^{-1}, the peak position commonly seen for high quality thermally grown SiO_2. The width of the peak can also be seen to decrease, indicating a more uniform bonding angle between the Si and O atoms, and by extension more uniformity of the SiO_2 phase throughout the film. There is therefore a structural reordering occurring within the film, this serves as the initial evidence of phase separation within these films, although only indirectly. The RBS data showed no significant variation of the Si and O peaks, so if a more uniform SiO_2 phase is forming then the excess Si within these films must be separating, else its presence would continue to strain the Si-O bonds throughout the film and cause a broadening of the IR signal of said bonds. The resulting phase separation forms Si-clusters embedded within an SiO_2 host. By phase separating the Si-clusters will only strain these bonds in the vicinity near the cluster, meaning that these strained bonds contribute less to the measured IR signal.

Similar trends are observed for all of the films analyzed through FTIR spectroscopy. Consider Figure 8.8 which shows the spectra for a film having 67% Si. The O concentration of this film is not sufficient to enable the formation of an oxide host with Si embedded within, but the FTIR spectra still show the evolution of an SiO_2 phase. In this case the phase separation may be producing SiO_2 clusters within an a-Si host.

After annealing no significant evidence of Si-H bonding remains in either of these films. Even in the as-deposited films little evidence of Si-H bonding was seen, especially when compared to the results from the initial FTIR analysis shown in Figure

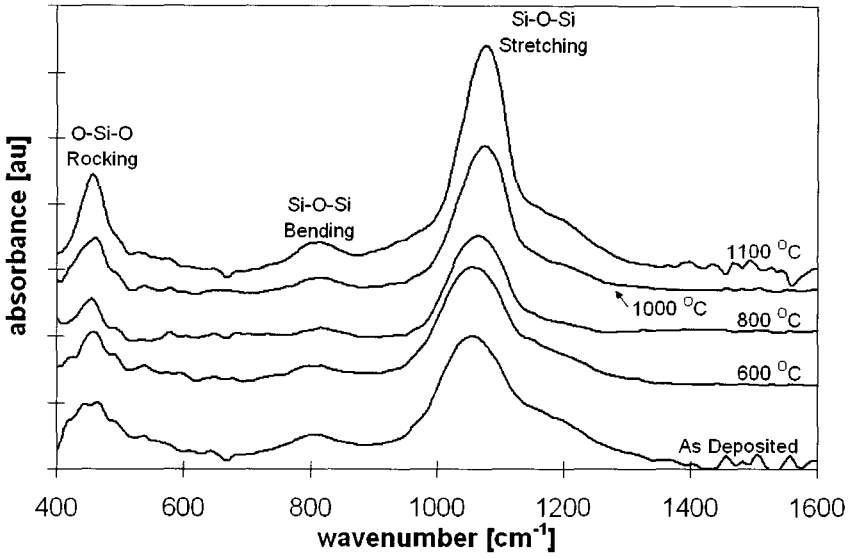

Figure 8.7: FTIR spectra for a sample containing 42% Si annealed for 60 minutes at the temperatures shown. With increasing anneal temperature the appearance of the Si-O related peak shows evidence of an SiO_2 phase forming within the films. The spectra have been shifted vertically for clarity.

8.6, which showed a significant Si-H wagging mode absorption peak. Some evidence of the Si-H bending mode, at approximately 880 cm^{-1}, can be seen in the spectrum of the sample having 67% Si (Fig. 8.8), however, the peak is not of significant intensity. The nature of this variation was not explored, although it may be related to a memory effect that has been observed in the ECR-PECVD chamber, with increased H being incorporated from run to run unless the chamber is subjected to an Ar plasma cleaning. It is therefore difficult to analyze trends of the H data within these films.

8.3 Optical Properties of the Films

8.3.1 Spectroscopic Ellipsometry Analysis

We now consider the results of spectroscopic ellipsometric modeling of these films. Figure 8.9 shows the model that was constructed in order to obtain information on the SiO_x layer. Notice that a 10$\mathring{A}$ SiO_2 layer is included because the native oxide is

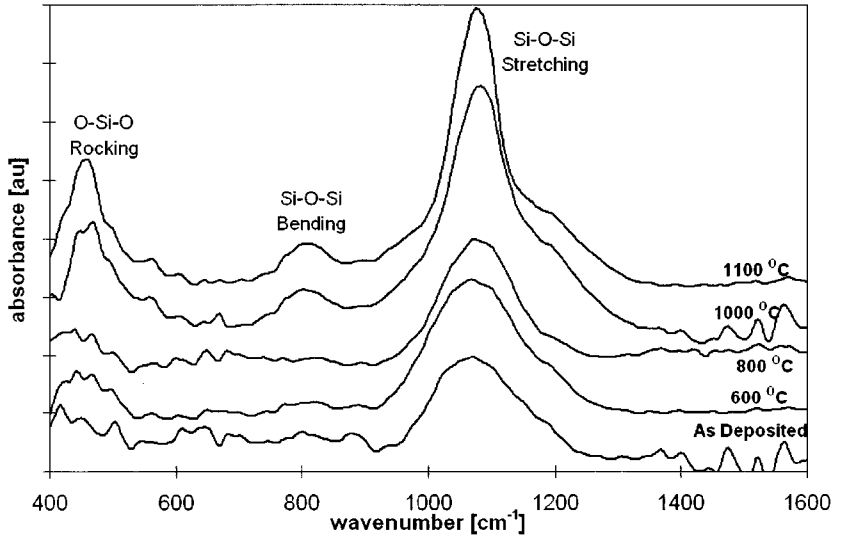

Figure 8.8: FTIR spectra for a sample containing 67% Si annealed for 60 minutes at the temperatures shown. Even with a high Si content there is evidence of the formation of an SiO_2 phase within the films. The spectra have been shifted vertically for clarity.

not removed prior to deposition.

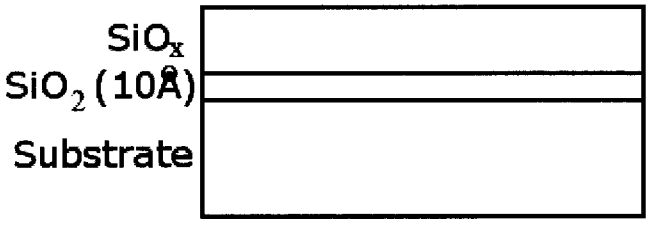

Figure 8.9: The model of the film structure assumed for ellipsometric modeling of the measured Ψ and Δ parameters.

Initial modeling efforts were directed at extracting the refractive indices of these films, not the extinction coefficient. Results for a set of samples deposited both with and without Ar in the source gas mixture are shown in Figures 8.10 and 8.11,

respectively. The spectrum shown for a-Si was taken from Palik for comparison [44]. Modeling of a-Si films was not successful for reasons that will be discussed later in this chapter.

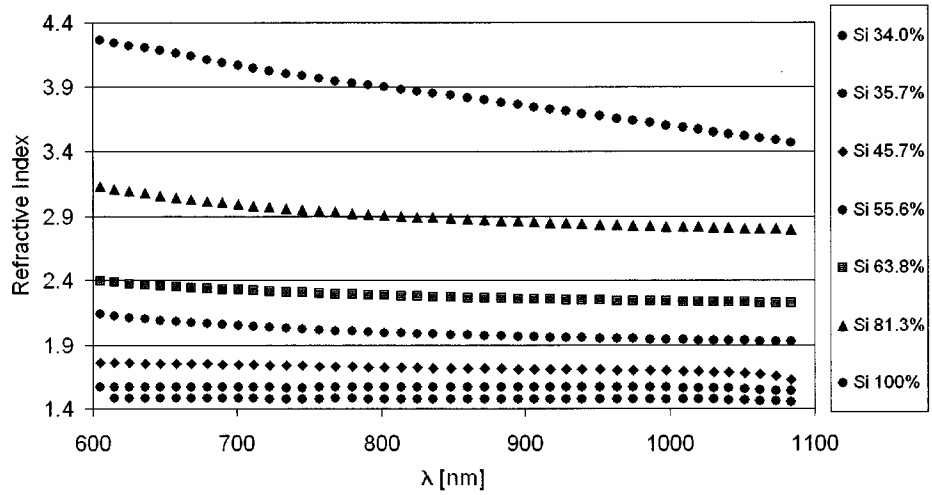

Figure 8.10: The refractive indices derived from ellipsometric measurements for a set of films deposited with an Ar flow to maintain chamber pressure. The values shown for a-Si (Si 100%) are from Palik [44].

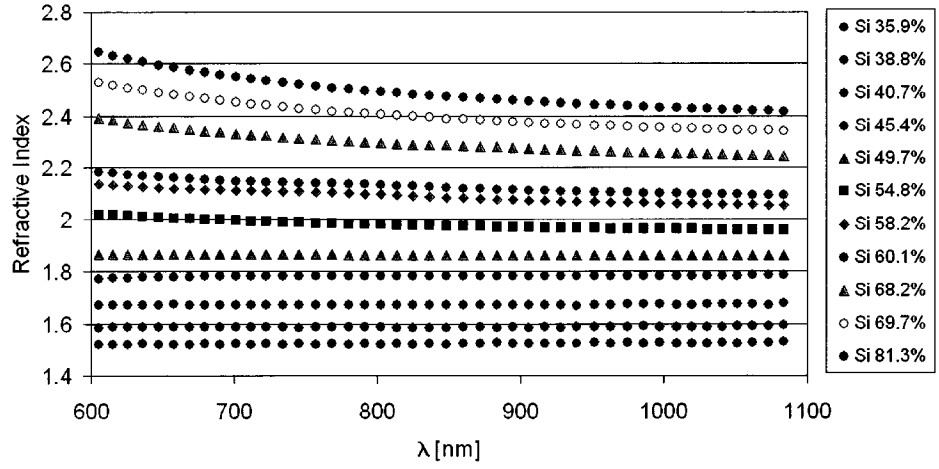

Figure 8.11: The refractive indices derived from ellipsometric measurements for a set of films deposited without an Ar flow to maintain chamber pressure. Note that without Ar a-Si thin films cannot be deposited.

From the two plots it is apparent that the refractive indices of those films deposited without Ar are lower than those deposited with an Ar flow, with the greatest difference observed for the two films deposited with approximately 81% Si. As mentioned earlier this differs slightly from the SWE results seen in the initial film characterization stage, where no significant difference was seen in the two curves. However, during the initial calibration run a lower microwave power was used than for this set of samples. Under these conditions the deposition rates for the films are changed and properties of the deposited films, such as density and hydrogen content, are modified.

Figure 8.12 compares these results to the optical constants of Si-based materials found in the literature that were presented in Chapter 3 [44]. One can see that there is good agreement between the values, with small deviations being easily attributed first to the fact that the compositions of the films are not exactly SiO_2 and SiO, and secondly to variations in film densities, hydrogen incorporation levels, and the use of differing growth method.

During the initial modeling stage it was found that the dispersion relations used were not always suitable for modeling of the extinction coefficient, producing non-realistic data sets, particularly as the films became more Si rich. By carefully analyzing the fitting process of the dispersion relation during the modeling it was possible to extract a more reasonable extinction coefficient spectrum. This process was only done for a limited number of films which are discussed in the next section. Current research efforts are being invested into developing Kramers-Kronig consistent models in order to more accurately determine the values of k.

8.3.2 The Effects of Annealing on the Optical Constants of the Films

The effects of annealing on the optical properties of these films show continued evidence of the phase separation discussed in the analysis of the FTIR spectra. Figure 8.13 shows the results from spectroscopic ellipsometric analysis of the film containing 42% Si, annealed for 60 minutes at the temperatures shown. As the anneal temperature is increased the refractive index is seen to decrease. This is a result of the

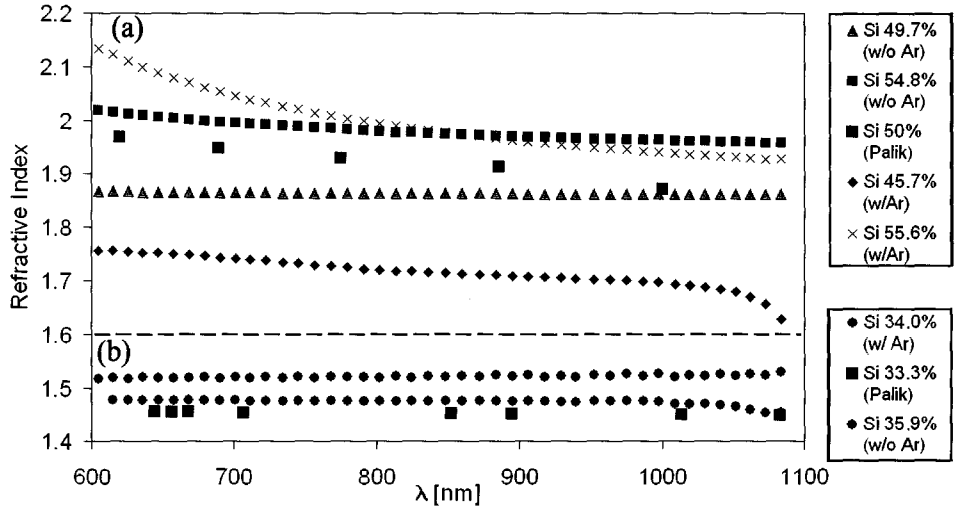

Figure 8.12: A comparison of the refractive index of the deposited films with compositions near (a) SiO and (b) SiO_2 with those found in the literature [44]

formation of the SiO_2 phase with nanoclusters embedded within, causing a lower effective refractive index for the film. This effect is discussed further after examining the results of annealing on the optical constants of films with varying compositions.

Figure 8.14 shows the refractive indices and extinction coefficients of films containing 42, 48 and 51% Si, derived from SWE measurements. Some deviation is seen between these results and those from spectroscopic ellipsometric analysis, specifically in regards to the behavior of the extinction coefficient after anneals of 1000°C and higher, which can be attributed to modeling aspects. Spectroscopic ellipsometry provides a large data set which can be fit using a developed model, while SWE provides measurements at only a single wavelength. Because of this limitations of SWE the accuracy of measurements for complex films is slightly diminished. The trend of the data remains the same.

The effect of annealing on the refractive indices can be correlated with the results obtained from compositional and FTIR analysis. As the anneal temperature of the film is increased phase separation begins to occur, and the effective refractive index of the SRSO layer is lowered towards that of SiO_2. The nucleation and crystallization of nanocrystals also contributes to this decrease, as crystalline Si has a lower refractive

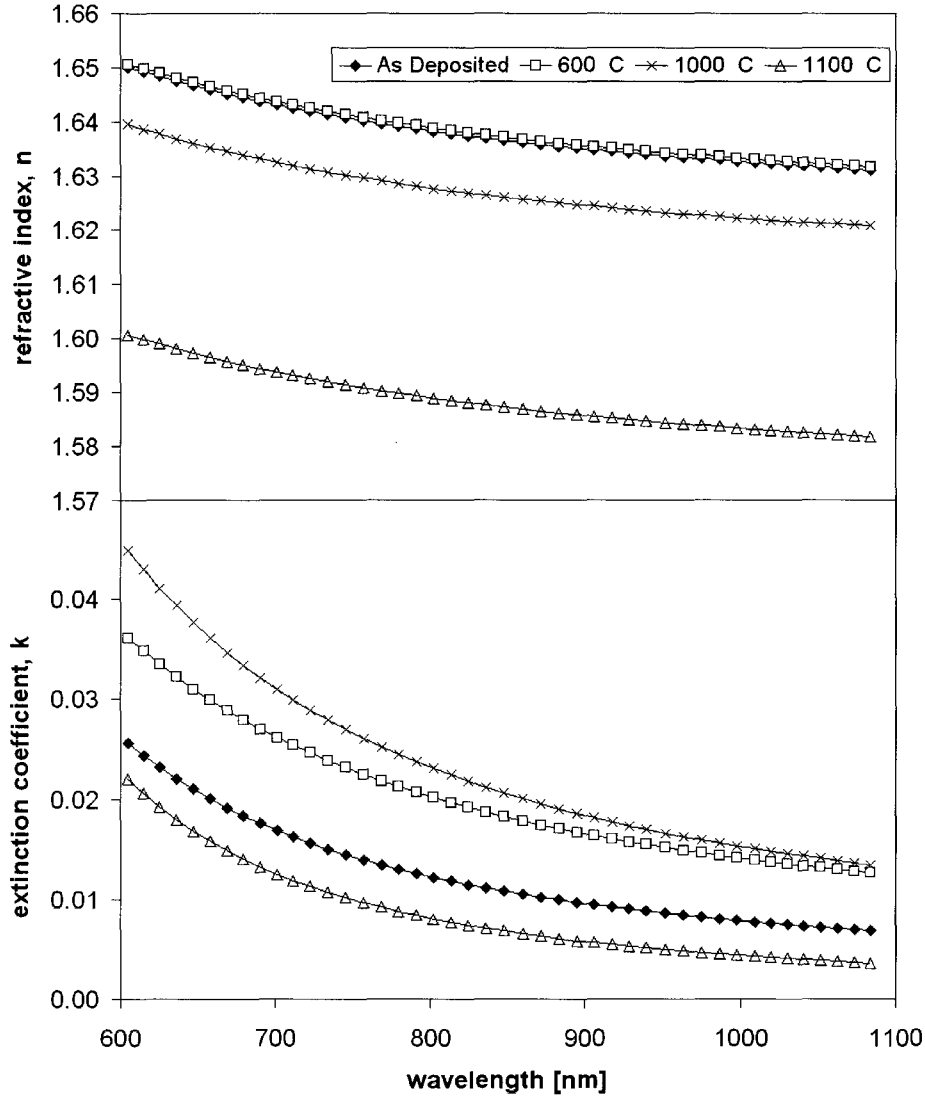

Figure 8.13: Refractive indices and extinction coefficients derived from spectroscopic ellipsometry analysis of the optical properties of a film containing 42% Si and annealed for 60 minutes at the temperatures shown.

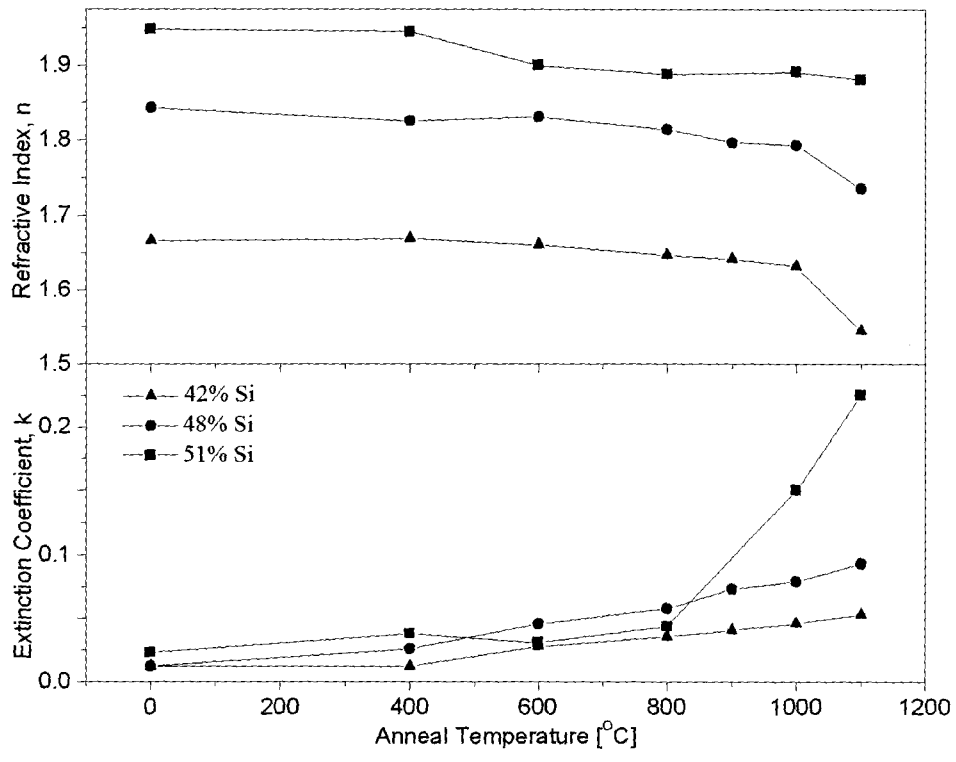

Figure 8.14: The effects of annealing temperature on the refractive index and extinction coefficient for films containing 42, 48, and 51% Si.

index than *a*-Si. The presence of the Si nanocrystals sets a limit to how far the refractive index can decrease as they will still contribute a higher value of n to the layer than the SiO_2 phase. As the Si precipitates and *a*-Si clusters and Si-ncs form there is a trend of the extinction coefficients of the films to increase. For a film with 51% Si a large increase in k is seen, which must be the result of the phase separation of an *a*-Si phase which does not fully crystallize. At an anneal temperature of 1100°C the extinction coefficient determined through spectroscopic ellipsometry shows a decrease (Fig. 8.13). Two effects may produce this, one is the formation of Si-ncs, causing a large decrease in k if the majority of *a*-Si clusters have crystallized. The second is the potential formation of voids within the film as a result of the crystallization process, lowering the effective refractive index and extinction coefficient of the film. This formation of voids may be related to the formation of pits in *a*-Si films discussed later in

this chapter. The results of SWE measurements showed an increase in the extinction coefficient as the anneal temperature increased, particularly in the film having 51%Si. This is to be expected, as in films with high Si concentrations there is sufficient Si to produce an *a*-Si/Si-nc phase that is not embedded within an SiO_2 phase, but rather "co-exists" with it. The clustering of large amounts of Si in these films would significantly influence the trend of the extinction coefficient towards that of *a*-Si, while at approximately 50% Si the development of both phases has little influence on the refractive index. If the Si content was increased significantly more above 50% the opposite trends would be expected, with the films having characteristics dominated by *a*-Si, but being modified by the formation of SiO_2 clusters formed within this *a*-Si host (or polycrystalline Si host depending on the anneal conditions). With the development of better models it is expected that the behavior of the extinction coefficient will become clearer.

For this work, only the effective refractive index and extinction coefficient of the layer were analyzed. In theory it is possible to model a layer as consisting of a two separate media, Si and SiO_2, and by properly determining the contributions of both to the effective refractive index the properties of both phases could be extracted. This could be particularly interesting in analyzing the properties of films with Si-ncs. Amans *et al.* have done a study similar to this in order to analyze the properties of Si-ncs [81]. In their analysis the Bruggerman effective medium approximation and Tauc-Lorentz models were compared and optical constants for a Si-nc layer were determined. They found that the optical constants of Si-nc were not a complete match to those of crystalline Si, and did not display the detailed features seen in c-Si. The shape of the refractive index curve that they determined for Si-ncs bore more resemblance to that of *a*-Si, however, the value of the refractive index from the Si-nc layer is lower than that of c-Si, and therefore the results shown above remain consistent with nanocrystal formation.

8.4 Photoluminescence Analysis

A set of films containing 36, 39, and 42% Si were deposited for the purposes of PL analysis. Figures 8.15, 8.16, and 8.17 show the PL spectra for these films after annealing for 60 minutes at the indicated temperatures.

For comparison the spectra of all three films annealed at 1100°C are shown in Figure 8.18.

With the exception of the sharp line emissions seen in Figure 8.17 the trends of the PL seen in these films can be discussed in terms of nanocrystal nucleation and quantum confinement effects. Let us consider first the effects of varying the composition of the films. If initially there is only a little excess silicon in the film, as is the case for the 36% Si film, then there is only sufficient Si to form a small quantity of small nanocrystals. Because of their small size blueshifting of the emission wavelength is greatest in these films. As the silicon content is increased the emission wavelength is redshifted and an increase in the PL intensity occurs as larger and more nanocrystals can form. If the anneal temperature or time is increased this will also allow more and larger nanocrystals to form. As some nanocrystals grow and new nanocrystals form a broader distribution in sizes leads to a widening of PL peaks. In cases where the Si content of the films is high, the nanocrystals may grow beyond the confinement regime, causing a decrease in the PL intensity, as is seen for the film with 42% Si annealed at 1100°C. In principle the PL emission wavelength should allow for the determination of the size of the nanocrystals. However, due to the presence of various interface states, which play a significant role in the recombination process and are discussed momentarily, determination of nanocrystal size is not so simple. In order to determine nanocrystal size from the PL spectra of these films it would be necessary to develop models which account for the influence of these various possible interface states on the PL process.

The presence of two emission regions, one at approximately 540 nm and the other at 750 nm, may be caused by the presence of different interface states present for recombination. As discussed in Chapter 3, the Si-O interface plays a critical role in the recombination process, and produces the PL observed around 750 nm through

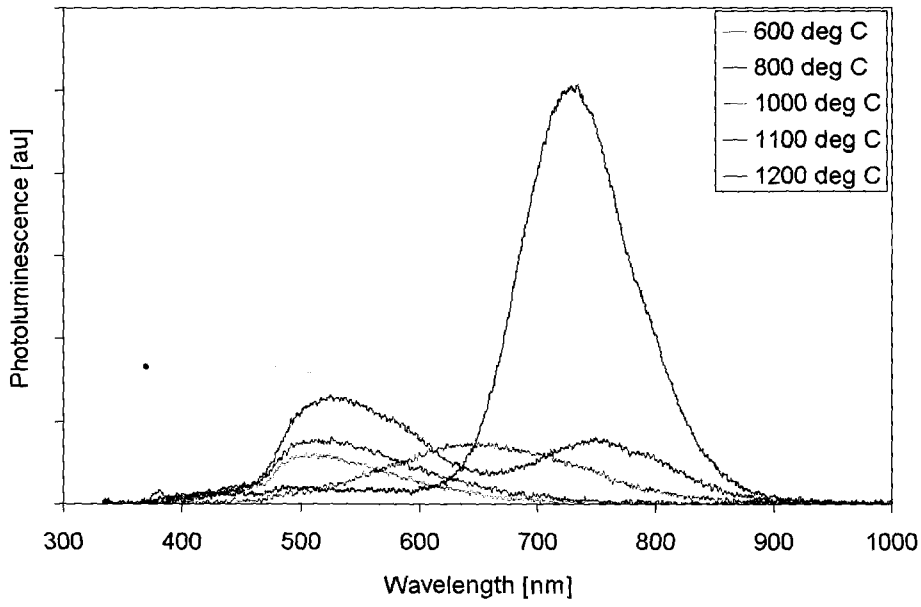

Figure 8.15: PL spectra for a film containing 36% Si after annealing for 60 minutes at the temperatures shown.

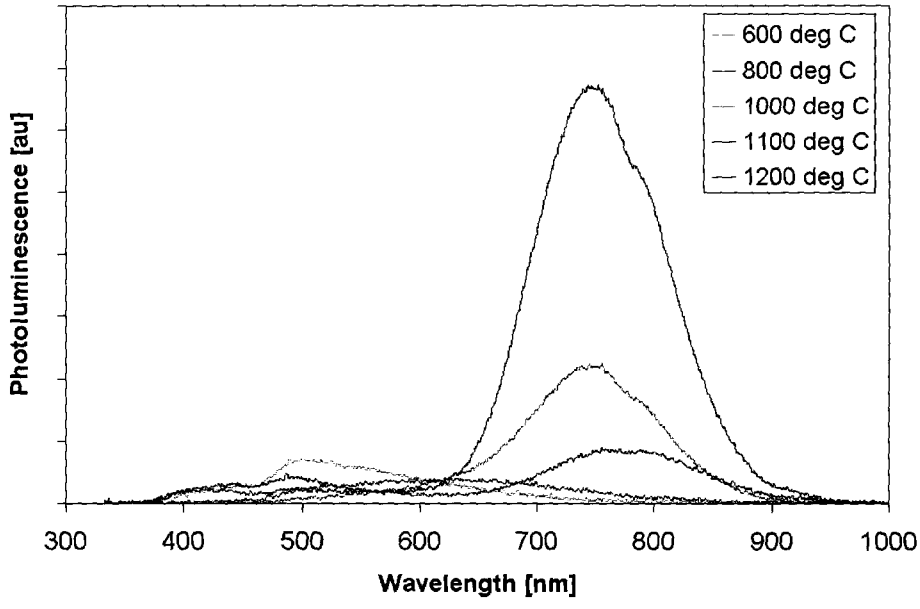

Figure 8.16: PL spectra for a film containing 39% Si after annealing for 60 minutes at the temperatures shown.

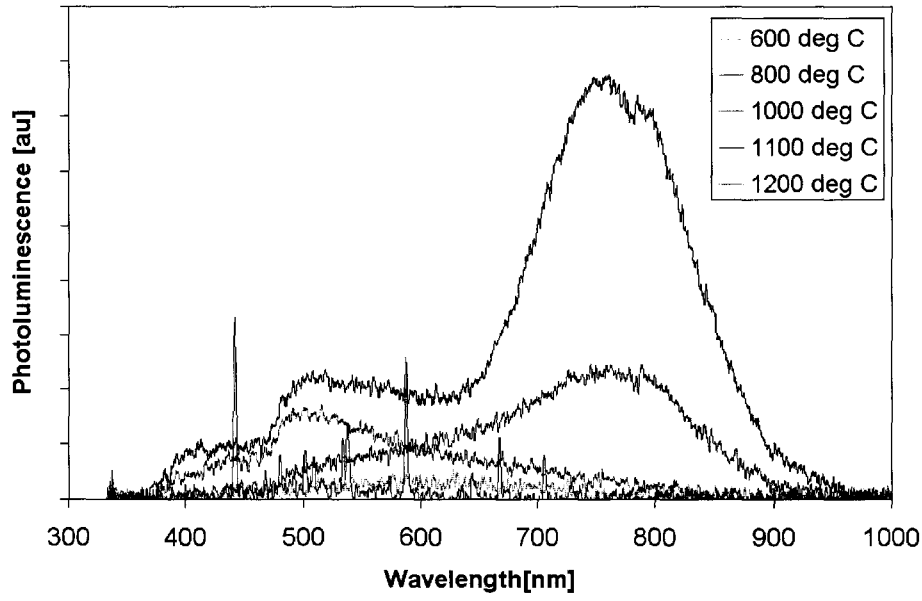

Figure 8.17: PL spectra for a film containing 42% Si after annealing for 60 minutes at the temperatures shown.

localized Si=O states. It is also possible to see a shoulder region on the low energy side of this peak, the exact nature of which is not known. However, as this peak appears in the same vicinity as that of a peak attributed to an Si-O interface it is quite possible that another Si-O related localized state forms in addition to the Si-O state [39]. The observed 540 nm peak may be produced by nanocrystals with another oxide interface state through which the recombination occurs [39]. The potential presence of an a-Si region surrounding the nanocrystals and the interface states this would present for recombination has not been explored but could also play a role in the luminescence process. The interface states play an important role in the recombination process but as of yet their full details have not been thoroughly examined [47]. These results also indicate that there must be additional mechanisms affecting the luminescence from these films, as there is no clear pattern in the growth of one PL emission peak relative to the other. Consider Figure 8.19, which shows how the intensity of these peaks vary as a function of temperature for the PL spectrum shown in Figure 8.15. The peak located at around 540 nm develops at low anneal temperatures. At 1100°C

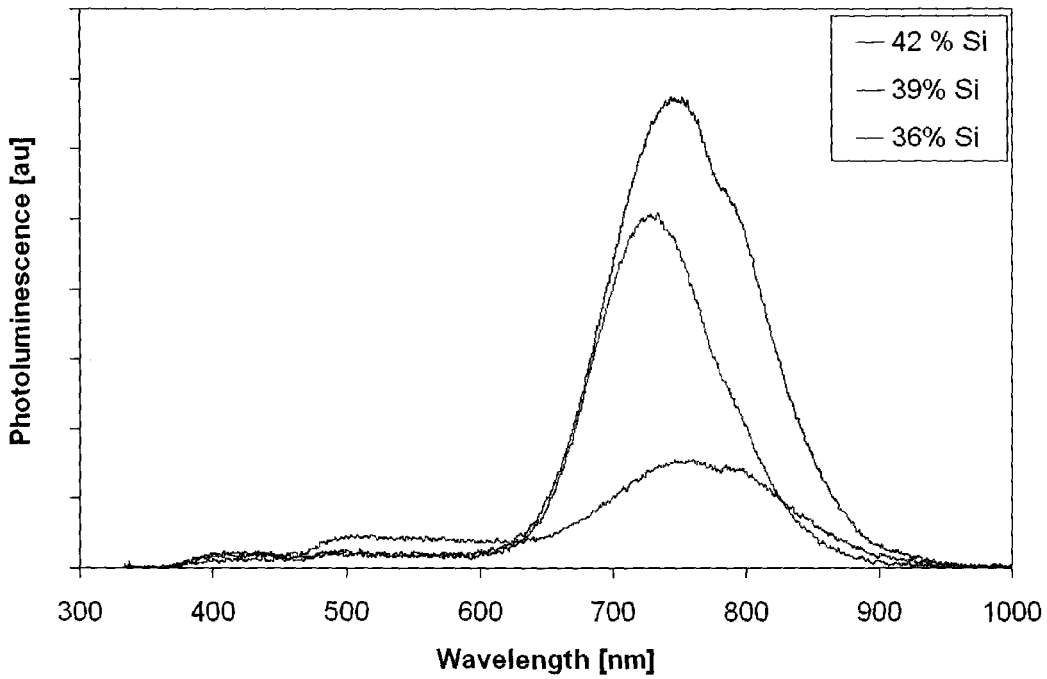

Figure 8.18: PL spectra for a films with 36, 39, and 42% Si annealed at 1100°C for 60 min.

this peak has diminished and the peak at ~750 nm has grown in intensity. At 1200°C the intensity of the 540 nm peak has risen again, while that of the 750 nm peak is greatly diminished. Figure 8.16 shows a similar trend, but the high energy peak has shifted to ~500 nm and does not show the same amount of increase after the 1200°C anneal. For this work the aim was to observe PL within the films and to gain an understanding of how this PL is related to the composition, structure, and annealing treatments of the films. A detailed analysis of the mechanisms affecting the luminescence process is planned as part of the next stage of this project where a joint theoretical and experimental analysis will be done with the aim of applying these nanocrystals in Si-based devices.

The sharp line emissions observed in films containing 42% Si after annealing at a temperature of 1200°C(Fig. 8.17) are similar to those seen after high temperature annealing of *a*-Si films, and are discussed in the final section of this chapter. Because

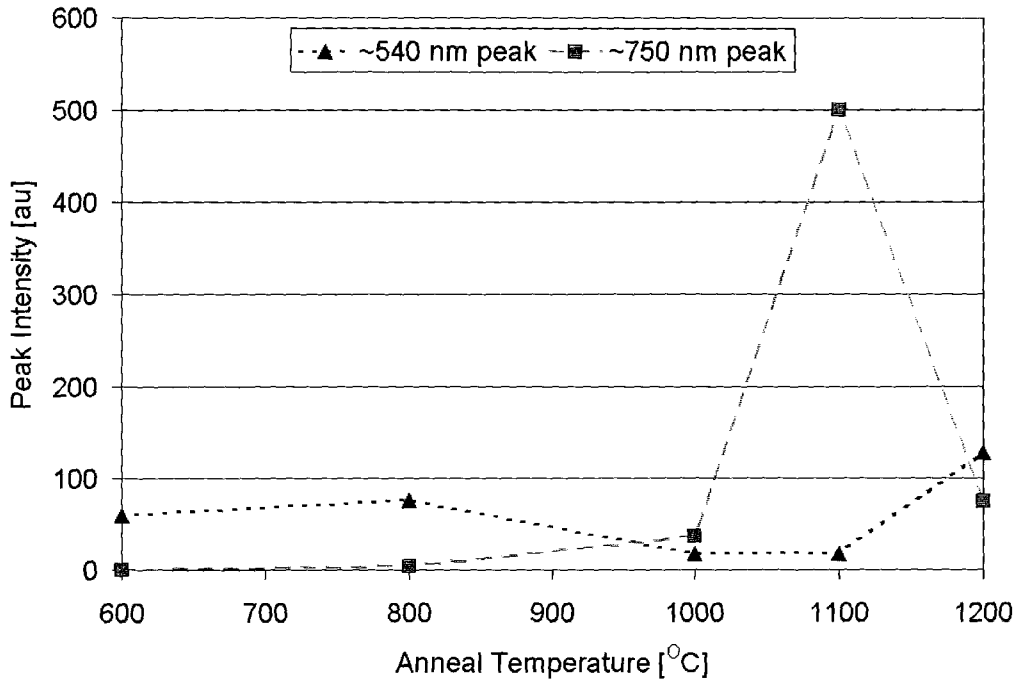

Figure 8.19: The variation of the intensity of the PL Peaks as a function of temperature for a film having 36% Si.

the luminescence from the nanocrystals is completely quenched when these peaks appear the film structure may be suffering a degradation caused by a similar effect to that seen in a-Si, discussed in the next section, inhibiting luminescence. This degradation, in addition to nanocrystals extending beyond the confinement regime, may also play a role in the decreased PL signal from the film with 42% Si.

8.5 Direct Evidence of Si nanocrystals in SRSO Thin Films

Up until this point the presence of Si nanocrystals has been inferred from the results of a number of characterization methods. In order to provide some direct evidence of their existence Figure 8.20 shows a x-ray diffraction (XRD) pattern for a film having 42% Si annealed for 180 min. at 1100°C. These results, showing the

presence of a broad peak related to the a-SiO_2 phase and another related to diffraction from the (111) Si plane in nanocrystals are consistent with XRD results found in the literature [52].

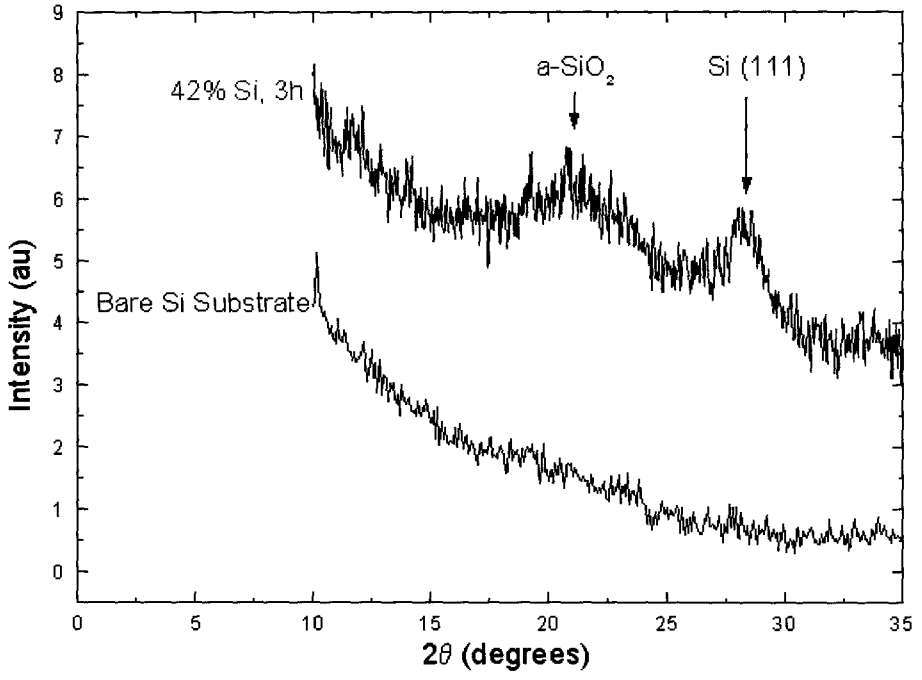

Figure 8.20: A XRD pattern showing evidence of the presence of Si nanocrystals in a film having 42% Si annealed at 1100°C for 180 min. For reference the diffraction pattern of a bare substrate is shown. Patterns have been shifted vertically for clarity.

Further experiments to provide direct evidence of the nanocrystals, including XRD and HRTEM, are in preliminary stages and are the subject of future work.

8.6 The Effects of Annealing on a-Si Films

Annealing of the a-Si films at high temperatures produced an interesting effect, in that pits were observed to form in the films. A similar effect, producing surface roughness but not the deep pits seen for a-Si, was observed in some of the SiO_x films deposited without Ar in the plasma precursor gases. Figure 8.21 shows the optical

microscopy images illustrating the evolution of film structure with increased annealing temperature.

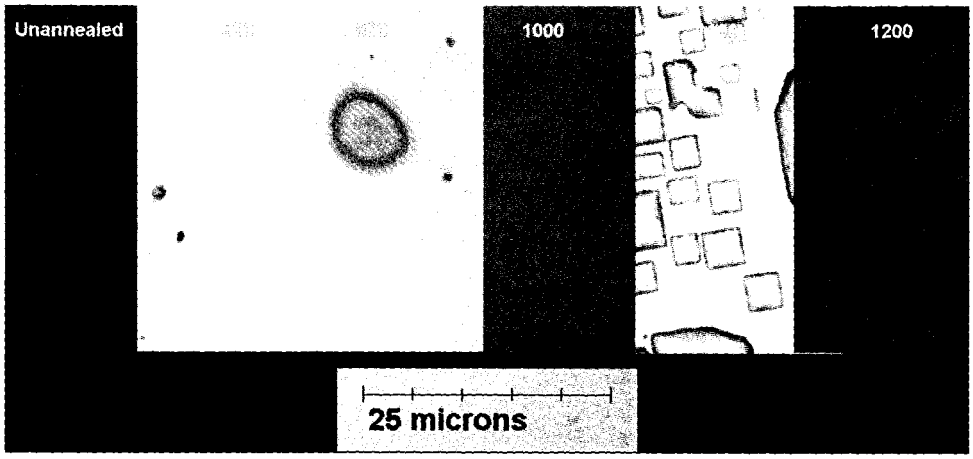

Figure 8.21: Optical microscopy images of a-Si:H annealed for 60 minutes at the temperatures shown. At high anneal temperatures pits have been found to form within the films.

One can clearly see that there are some defined crystal-like, rectangular structures that have formed within these films. From optical microscopy images alone it can be difficult to clearly determine the depth of these structures, and they can appear to be structures formed on the surface. In order to illustrate that these structures are in fact pits, AFM and SEM images of the films annealed at 1100° and 1200°C for 60 min. were obtained. The AFM images are shown in Figure 8.22. A 3 dimensional view of the film annealed at 1200°C is shown in Figure 8.23.

The circular defects seen in the center of the AFM images exist in abundance throughout the film surface. The abundance of both the circular and square defects is also evident in the SEM image shown in Figures 8.24. Figure 8.25 provides a clearer view of the structure of these pits than the previous images.

The defined structure of the pits, combined with the fact that they are all oriented along the same direction, supports the idea that this process is somehow related to crystallization occurring in these films. However, the exact cause of the formation of the pits is still under investigation. To the author's knowledge this effect has not

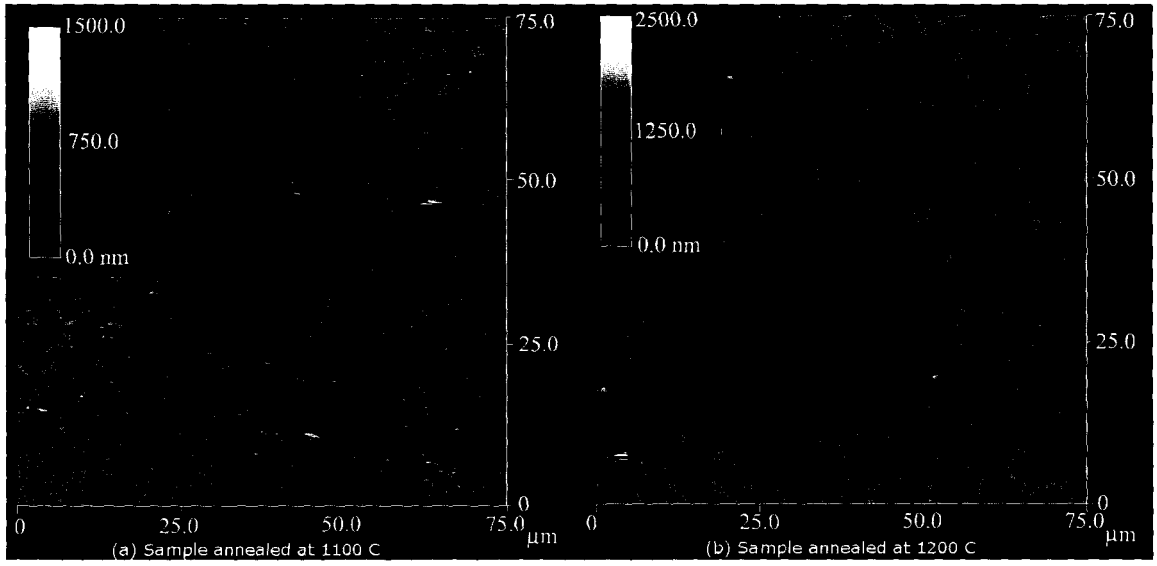

Figure 8.22: AFM images of pits formed in *a*-Si:H after a 60 min. anneal at (a) 1100°C and (b)1200°C.

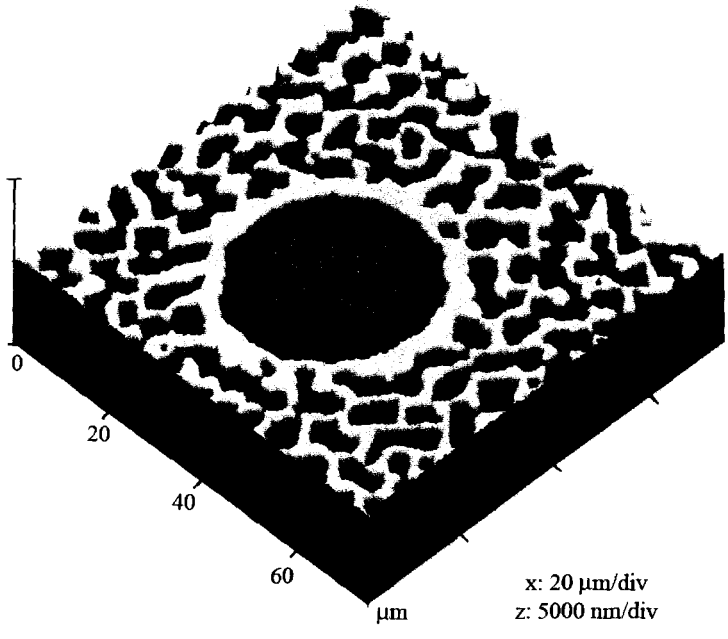

Figure 8.23: A 3-D AFM image of the pit structure for a film annealed at 1200°C for 60 min.

been observed previously in a-Si films. This is not completely unexpected, however, as most annealing studies of Si are performed for microelectronics applications, for which high anneal temperatures are not suitable.

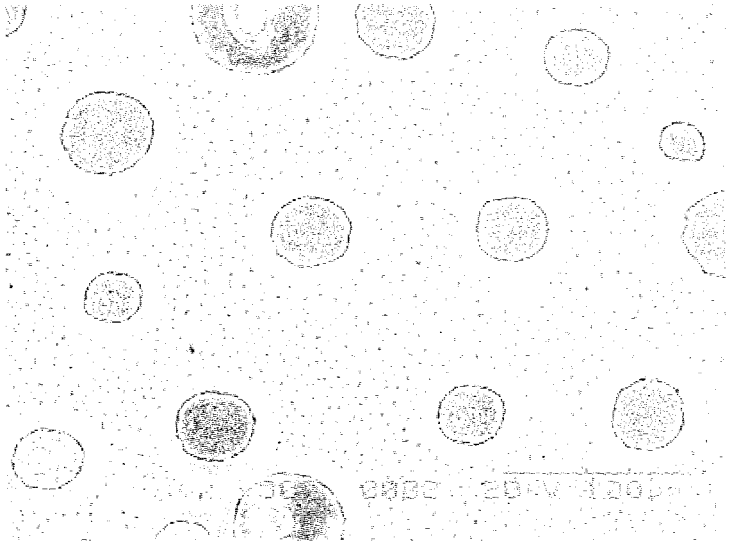

Figure 8.24: A SEM image of an a-Si film annealed at 1100°C for 60 min. The abundance of pits and circular defects in the film surface can be seen.

Figure 8.25: A SEM image showing the structure within the pits.

Figure 8.26 shows a high resolution transmission electron microscopy (HRTEM) image obtained for one of the annealed films in an effort to try and determine the cause of pit formation. While the imaging did not show pits present in the surface of the film it does present some information on film structure that helps in the understanding and initial hypotheses on how these pits form. From the image one can see that three layers are present, including the substrate. Additionally, there is evidence of some large crystallites forming near the substrate surface. These features will become more apparent in the following TEM images where they are examined a little closer.

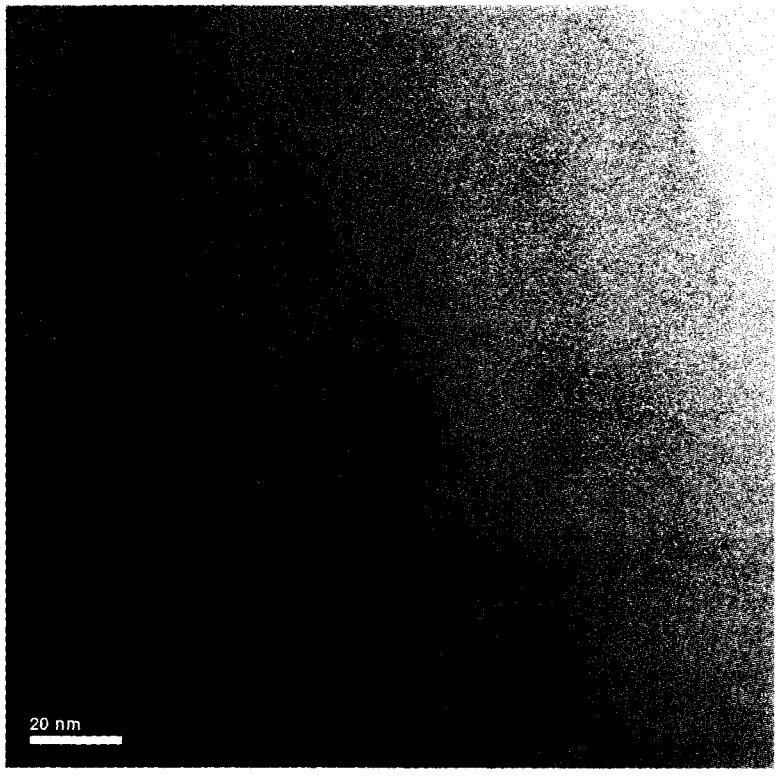

Figure 8.26: A HRTEM image of a high temperature annealed a-Si film. The image shows three distinct layers in the film, including the substrate, as well as some distinct features at the substrate film interface.

Figure 8.27 shows the interface between the upper two layers observed in Figure 8.26. The top layer remains amorphous, with no evidence of structure, while the lower layer shows the distinct presence of crystallites within it. HRTEM actually

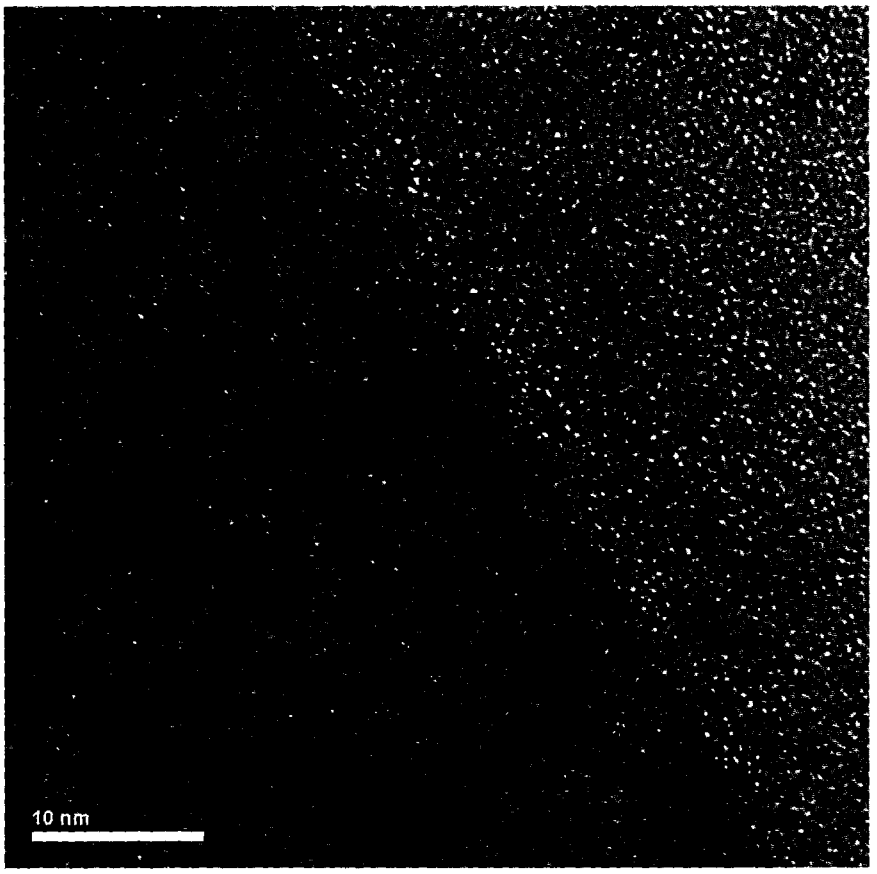

Figure 8.27: A HRTEM image of the two layers that have formed in the film after the anneal process. The upper layer remains amorphous. The lower layer shows the presence of a number of crystallites.

allows for lattice imaging, therefore, when there is crystallinity, it is evidenced in the areas where there is clear alignment of the structure, producing what appear as a series of 'lines'. It can also be seen that there is no particular order to the orientation of these crystallites.

At the interface between the substrate and the film the same polycrystallinity is seen, however, a few distinct areas, which appear darker in the images and were visible in Figure 8.26 as well, are also noted. In these areas a well defined crystallinity, orientated along the same axis as that of the substrate, is seen. Examining the native oxide on the substrate it can be seen that below these crystalline areas the oxide has decreased in width, and even appears to be completely absent at some points. At

these points it then becomes possible for the crystallites to grow aligned with the substrate orientation. Similar to the coalescence processes discussed for thin film growth these crystalline areas would then grow at the expense of other crystallites in the polycrystalline layer.

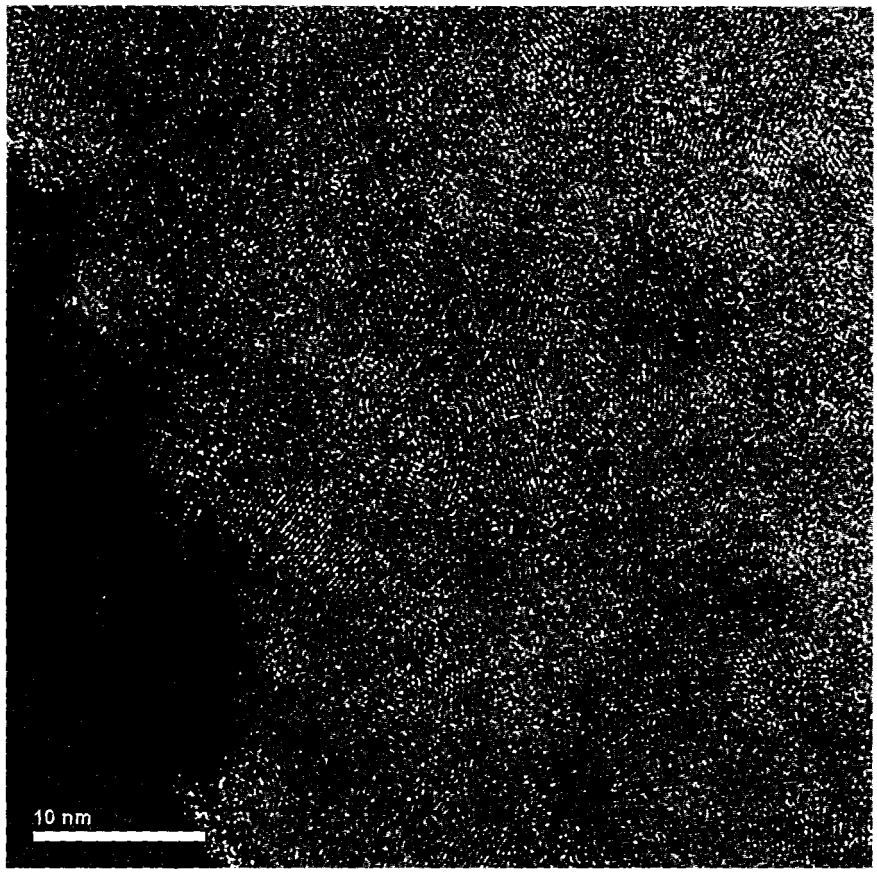

Figure 8.28: A HRTEM image of the film-substrate interface for an a-Si film. A number of crystallites are visible in the deposited layer. Near the substrate a large crystalline area has formed, and, in some areas, is in contact with the substrate.

If the HRTEM images are now considered along with the AFM, and SEM images it is possible to formulate some initial ideas as to how the pits form. The areas where the crystallinity is aligned to that of the substrate may be the initial nucleation sites within the film. As these sites grow the increased order and structure can be expected to create areas of the film with greater densities than those areas which are polycrystalline or amorphous. With a further increase in the anneal temperature

this densification process may occur with parasitic effects on the surface of the film. Restructuring appears to proceed faster with the circular defects than the rest of the film. If one examines the structure of the circular defects in the AFM image at 1100°C the texture appears heavily pitted and trenched, similar in structure to the trenched film formed as the pits grow and merge in the films annealed at 1200°C. At 1200°C the circular defects have planarized. These defects may then possibly lie at the initial crystallization points, or at intrinsic defect sites which cause them to crystallize at a faster rate than the rest of the film, which may be why they pull away from the surrounding film and create deep trenches, isolating themselves. One can clearly see that these defects also become recessed from the film surface. This would seem to support the idea that a densification is occurring in crystalline areas of the film. Of course much more research is needed, and is planned, in order to explore and explain this effect fully.

PL measurements conducted on these films showed an initial peak in the as-deposited films that was quenched even at low anneal temperatures. Therefore, the peak must be caused by defects in the deposited film that are easily suppressed. What is even more interesting is that after high temperature anneals the PL spectra of these films showed very sharp peaks, similar to those seen in the PL spectra of some SRSO films (Figure 8.17). The possible origin of these peaks is discussed in the final section of this chapter.

8.6.1 Characterization Difficulties

Some difficulties presented themselves during the characterization of these films that merit some discussion. Future work related to high Si content SRSO, *a*-Si, and *a*-Si:H thin film materials will need to consider these difficulties and attempt to find methods of characterization that may overcome them.

Problems were encountered during ellipsometric modeling of films with high silicon content for a number of reasons. The first is that these films were deposited on Si substrates, therefore, as the Si content of the films was increased there is less optical contrast between the films, and individual layers are less clearly resolved when fitting

the model parameters. The second, and perhaps greatest difficulty, arose when analyzing films with compositions closest to a-Si, particularly those that were annealed, as the structure of the films is highly modified when large crystallites and pits form. The sizes and depths of the pits were typically large enough that it would not be sufficient to treat them as simple surface roughness and model them as a Si-air effective layer. Additionally, these pits act as scattering centers and the optical analysis of these films, whether by FTIR spectroscopy or ellipsometry, did not yield useful results. As more information is obtained through further TEM imaging it may be possible to develop better models to account for the observed polycrystalline/amorphous layered structure. Scattering from the pits will be more difficult to circumvent.

8.7 PL from a-Si Thin Films and the Observed Sharp Line Emissions

Results of PL measurements for the a-Si films are shown in Figure 8.29. While no significant PL signal is observed several sharp emissions are present, similar to those seen in PL spectra of the SRSO samples annealed at 1200°C shown earlier. The broad PL signal upon which some of these peaks are situated may be the result of recombination within Si-ncs surrounded by an a-Si host, although it is difficult to be certain as the TEM images showed the presence of large crystallites. Another factor which may influence the PL signal is the formation of defects within these films.

The observation of sharp line emissions in multiple films, all annealed at high temperatures, raises the question of their origin. One can see clearly that their line shape is similar to emissions characteristic of atomic transitions. The most intense emission lines are seen at 441, 501, 532, 537, 586, 667, and 706 nm.

Due to another project being researched using the ECR-PECVD system there may be some trace amounts of rare-earth elements within the films. Initial comparisons between the emission spectrum of Erbium (Er), obtained from the NIST spectral database [82], and the lines seen here show some agreement. At the present time, we are not certain that these lines are originating from Er because (i) the relative

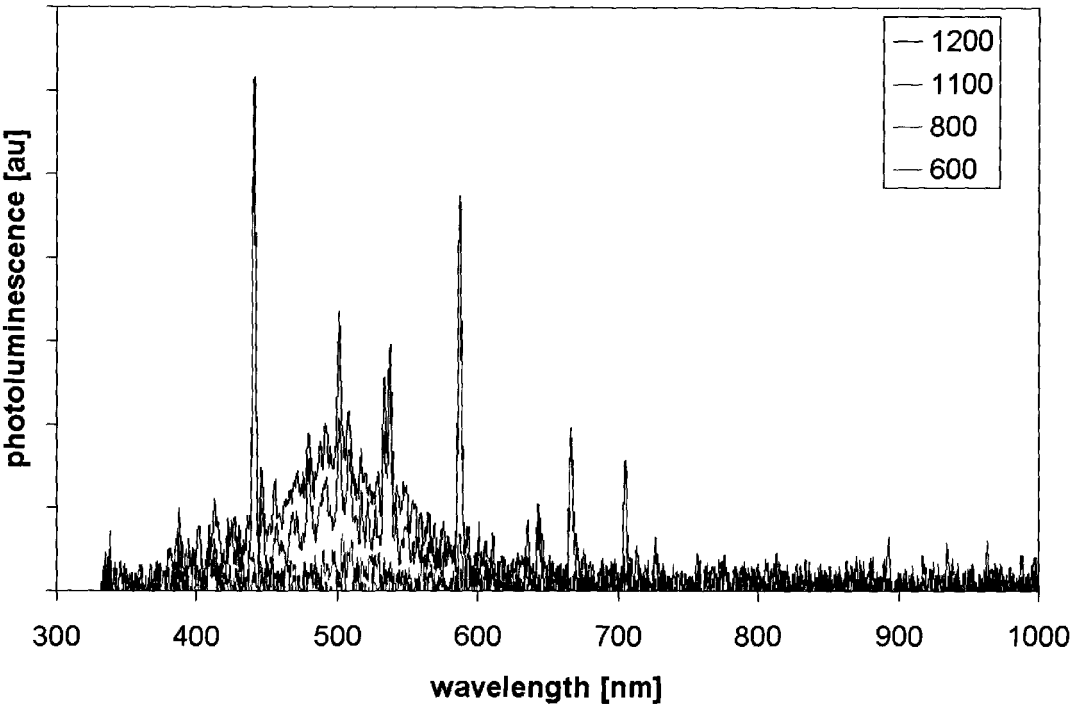

Figure 8.29: Effects of high temperature annealing on the PL spectra of a-Si films. At low anneal temperatures no PL is seen. After annealing at temperatures of 1100°C and greater sharp emission peaks, characteristic of atomic emissions, are present.

intensities of the emissions do not conform exactly to those in the database and (ii) one has to assume that multiple forms of ionized Er are present in the films. Trace analysis of the film composition will be necessary to see if there is any Er present and verify this, it will also provide evidence as to whether any other contaminant species are also contributing to the luminescence.

Chapter 9

Conclusions

Amorphous silicon and silicon oxide films have been grown through ECR-PECVD and been analyzed in terms of their composition, bonding structure, optical, and photoluminescent properties. The ECR-PECVD system allows for the deposition of films that span the entire range of silicon rich silicon oxide films from silicon dioxide to amorphous silicon, which allows for the deposition of films having refractive indices from 1.48 to 4.20 (at $\lambda = 632.8\ nm$). These optical constants have been correlated with the film compositions, obtained through IBA, and the deposition parameters. The very large range of optical constants can readily be exploited for waveguide and optical coating applications, although the non-negligible extinction coefficient in films with higher silicon content could not be ignored in these devices. When films were deposited using a non-constant chamber pressure and without the presence of an Ar gas flow, their refractive indices were seen to decrease, an effect that has been attributed to a decrease in the density of these films, allowing for the presence of more void space within the films.

Analysis of the composition of the films revealed that Ar and H are incorporated during the deposition process. FTIR analysis of the bonding structure indicates that at least some of this hydrogen is bonded within these films, primarily in the form of Si-H bonds, with more bonded H appearing in films having higher Si contents. No significant OH related FTIR peaks were observed. Annealing of the films causes the out-diffusion of Ar and H, decreasing their respective concentrations to values that

approach the detection limits of the IBA systems used for their measurement. RBS measurements did not show a noticeable change in the concentrations of Si and O within the films after annealing.

Analysis of the effects of annealing on the IR absorption spectra of the films revealed that an SiO_2 phase forms. Combined with the compositional analysis of the effects of annealing there must therefore be a phase separation occurring in the films, with the excess Si forming a nanoclustered phase that is able to nucleate at high temperatures and form Si-ncs.

The optical constants of the films have also been seen to be affected by the annealing process. With increased annealing temperatures the refractive index of the films is seen to decrease for films with less than 50% Si, due to the formation of the SiO_2 phase with embedded Si nanocrystals, with the SiO_2 phase dominating the refractive index. The nanocrystals also serve to decrease the refractive index of the films as crystalline Si has a lower refractive index than *a*-Si and *a*-Si:H thin films. The phase separation of Si, however, causes an increase in the extinction coefficient of the films. Once a Si concentration of 50% is achieved little change is seen in the refractive index, while at compositions greater than 50% the opposite evolution of the refractive index is seen, with an increase as the film phase separates forming SiO_2 clusters within an *a*-Si/poly-Si host. These high Si content films also show a decrease in their extinction coefficients with annealing, likely caused by the formation of the SiO_2 phase and the partial crystallization of the *a*-Si phase.

Analysis of the PL spectra from silicon rich films with compositions from 36 to 42% Si revealed that luminescent Si films can be produced using ECR-PECVD. The luminescence is a result of the formation of silicon nanocrystals within the films after high temperature annealing. Due to their small size, quantum confinement effects can occur, allowing one to overcome the poor luminescent nature of Si due to its indirect bandgap. These confinement effects lead to quantized energy levels which produce a blue-shift of PL emission from the bandgap energy of bulk Si. As the silicon content of the films is increased more and larger Si-ncs can form, causing the PL to be redshifted, and eventually the PL is suppressed as the nanocrystals grow beyond the quantum confinement regime. After annealing at 1200°C the PL in these

films has been seen to break down and sharp line emissions are observed, an effect also observed for a-Si films that become pitted at high anneal temperatures. There may, therefore, also be some issues with the thermal stability of some of these films that has not been fully explored. In addition, while luminescence has been observed and understood on a basic level, there is still a need for clarification of the role of interface states and other mechanisms which may be affecting the observed peaks in the emission spectra.

High temperature annealing of a-Si films was seen to induce the abundant formation of pits in their surface. These pits were rectangular in shape and showed defined structure and orientation. Additionally, circular defects were observed in the surface of the films. It is not yet clear what the exact cause of the pit formation is, yet HRTEM images reveal the formation of a polycrystalline layer with areas where the film crystallinity is aligned with that of the substrate. As these crystallites grow the film may be densifying, producing a parasitic effect on the film surface. Because the circular defects planarize at 1200°C they may be related to the initial crystallization sites of the films, with crystallinity extending to the film surface. Future work is planned, as discussed in the next chapter, in order to clarify the processes involved in the pit formation.

Sharp line luminescence was observed in some of the SRSO films after annealing at 1200°C and in the a-Si films after annealing at 1100° and higher. This luminescence is reminiscent of atomic emissions. These lines have been compared to atomic emission spectra and may be the result of erbium incorporation into the films, however, at this time these results remain inconclusive.

This project presents some of the initial work done at McMaster to observe luminescence from ECR-PECVD Si-based materials. The results show promise and the initial data is now available to explore this research further, including efforts to understand the quantum confinement process and implement devices based on these initial results, as discussed in the next chapter. Efficient light emission from Si, and specifically a Si-based laser, are key necessities for the development of monolithically integrated Si photonics, and Si nanocrystals may play a significant role in the development of said devices.

Chapter 10

Suggestions for Future Work

The work presented in this thesis represents only a small portion of the extensive research possible for these materials. Silicon rich silicon oxide materials are currently the subject of much interest in the research world as a potential silicon based emission material and many areas for future research exist. The possibilities for future work related to that discussed in this thesis fall into four broader categories: continued materials research, theoretical development, device implementation, and the joining of results from this work to other related areas of silicon research.

10.1 Continued Materials Research

Unfortunately time constraints make an exhaustive study of the material impossible during the course of a Master's Thesis. Fortunately they leave a number of areas of materials research from this project open for future study.

While it is known that the amorphous materials deposited by ECR-PECVD contain some void space the exact percentage is not known. Estimates may be drawn from the argon concentration in the films as argon is primarily unbonded and must be situated interstitially or within the voids. However, it may be possible to more accurately determine the porosity of these films. Techniques such as positron annihilation spectroscopy (PAS) would allow for the determination of void space which could be correlated with deposition parameters including chamber pressure, gas flows, and

microwave power. A positron annihilation spectroscopy setup exists at McMaster, however, the system works at energies too high for analysis of films with thicknesses as small as those described here. Two possible solutions present themselves, however, only one is truly viable for accurate analysis of these films. The first would be to deposit films with thicknesses of a few microns. Unfortunately this would be extremely time consuming and possibly not of great use as a few microns could be considered closer to a bulk film than those discussed here, causing a change in film properties. The second solution is to use an annihilation spectroscopy setup that works with lower energies. Currently a variable energy PAS system is operating at the UWO.

For the research done in this thesis the exact crystallinity of the nanocrystals was only briefly examined through the use of X-ray diffraction (XRD) experiments. A thorough investigation of the crystallinity of these films should reveal more details on both the nanocrystalline and polycrystalline phases of the films. The results from PL, XRD, and TEM experiments could then be used to correlate the PL to nanocrystal sizes and distributions.

Furthermore, current efforts are already underway to develop ellipsometric models that are Kramers-Kronig consistent and account for nanocrystal formation within these films through effective medium theories. These models will be better suited to analyze film composition and structure based on the extracted optical constants. The setup of another spectroscopic ellipsometer, with a broader wavelength range, will greatly enhance these modeling efforts.

The observation of pit formation in a-Si films is of significant interest. Because microelectronics processing rarely requires thermal treatment of films in the high temperature range explored in this thesis this effect is not of tremendous significance to microelectronics. However, since silicon rich silicon oxides require a high temperature anneal, this effect could pose a significant challenge for optoelectronic integration, and for photonic devices such as waveguides which employ the use of a-Si layers. To the author's knowledge no literature exists on this effect which opens the door for numerous experiments on the exact cause of pit formation and further details on the structure of the films after pits have formed. Additionally, the use of high-temperature annealed a-Si can be explored further for potential photonic applications, particularly

if these pits can be made to form in an ordered manner.

10.2 Theoretical Development

The luminescence of silicon nanocrystals is generally considered to be a result of quantum confinement effects, with recombination being related to the Si-O interface states present within the film. However, there is as of yet no completely satisfactory description of the luminescence process. Issues related to the exact role of quantum confinement and Si-O interface states in the luminescence of these materials could be explored in great detail and better theoretical models could be developed.

10.3 Device Implementation

Evidently, the luminescence of these materials makes them a potential candidate for the implementation of an Si-based emitter. Before devices such as this can be developed the luminescence must be optimized and suitable LED or laser geometries must be designed.

Because a variation in the optical constants of these films is easily achievable through a variation of the deposition parameters, the implementation of silicon rich silicon oxides in waveguide structures could easily be explored. Additionally, the formation of silicon nanocrystals in waveguide devices and their effects upon them could be investigated.

In an area outside of those discussed within this thesis, *a*-Si:H films also have applications in solar cells, as they are absorbing within the visible spectrum. While no one has yet undertaken any research projects involving an analysis of the films produced by this ECR-PECVD system for solar cell applications, the potential does exist to do so.

Appendix A

List of Publications and Presentations

A.1 Journal Publications

T. Roschuk, J. Wojcik, and P. Mascher. *Optical and compositional characterization of SiO_xN_y and SiO_x thin films deposited by electron cyclotron resonance plasma enhanced chemical vapor deposition.* J. Vac. Sci. Technol. A**24**, 883 (2004).

A.2 Conference Proceedings

T. Roschuk, J. Wojcik, M. Flynn, and P. Mascher. *The effects of high temperature thermal annealing on thin amorphous silicon films deposited by electron cyclotron resonance PECVD.* Presented at the 206th Meeting of the Electrochemical Society: 3rd International Symposium on Pits and Pores, article submitted for publication (2004).

T. Roschuk, J. Wojcik, E. A. Irving, M. Flynn, and P. Mascher. *Silicon nanocrystal formation in silicon rich silicon oxide thin films.* Proc. SPIE **5577**, 450 (2004).

M. Flynn, E. Irving, T. Roschuk, J. Wojcik, and P. Mascher. *Compositional and optical characterization of SiO_x films deposited by ECR-PECVD for photonic applications.* Presented at the 1st International Conference on Group IV Photonics, article submitted for publication (2004).

T. Roschuk, J. Wojcik, and P. Mascher. *Optical and compositional analysis of annealed SiO_x thin films deposited by electron cyclotron resonance plasma enhanced chemical vapor deposition.* Proceedings of the SVC 47th Annual Technical Conference, 362 (2004).

A.3 Conference Presentations

T. Roschuk, J. Wojcik, M. Flynn, and P. Mascher. *Analysis of the structure, optical properties, and luminescence of silicon nanocrystals formed in silicon oxide based thin films.* Presented at the 206th Meeting of the Electrochemical Society: Symposium on Nanotechnology (2004).

T. Roschuk, J. Wojcik, M. Flynn, and P. Mascher. *Amorphous Silicon-based Thin Films for Photonic Applications.* Presented at the 206th Meeting of the Electrochemical Society: General Student Poster Session (2004).

T. Roschuk, J. Wojcik, and P. Mascher. *Silicon Nanocrystal Formation in Silicon Rich Silicon Oxide Thin Films.* Presented at the Great Lakes Photonics Symposium (2004).

J. Wojcik, T. Roschuk, X. Tan, and P. Mascher. *On the effect of annealing treatments on the control of the dielectric-cap-induced bandgap shift in 1.55m laser structures.* Presented at the 12th Ontario Photonics Research Alliance Workshop: Temperature Sensitivity in Photonics (2004).

J. Wojcik, T. Roschuk, and P. Mascher. *Formation of silicon nanocrystals in a-Si and silicon rich silicon oxide thin films by high temperature annealing.* Presented at the 12th Ontario Photonics Research Alliance Workshop: Temperature Sensitivity in Photonics (2004).

T. Roschuk, J. Wojcik, and P. Mascher. *Optical and Compositional Characterization of SiO_xN_y and SiO_x Thin Films Deposited by ECR-PECVD.* Poster presentation at the Symposium on Functional Coatings and Surface Engineering (2003).

X. Tan, T. Roschuk, J. Wojcik, and P. Mascher. *Study of the Optical Property of SiO_xN_y Thin Films by Effective Medium Theory.* Poster presentation at the Symposium on Functional Coatings and Surface Engineering (2003).

References

[1] James D. Plummer, Michael D. Deal and Peter B. Griffin, *Silicon VLSI Technology: Fundamentals, Practice and Modeling*, Prentice Hall, Upper Saddle River, NJ., 2000.

[2] G. Kamarinos and P. Felix, "How will physics be involved in silicon microelectronics", *J. Phys. D:Appl. Phys.* **29**, 487 (1996).

[3] D. A. Buchanan, "Scaling the gate dielectric: Materials, integration, and reliability", *IBM J. Res. Develop.* **43**, 245 (1999).

[4] L. Pavesi, "Will silicon be the photonic material of the third millenium?", *J. Phys: Condens. Matter* **15**, R1169 (2003).

[5] International Technology Roadmap for Semiconductors 2003, Available online at public.itrs.net.

[6] L. Canham, "Silicon quantum wire array fabrication by electrochemical and chemical dissolution of wafers", *Appl. Phys. Lett.* **57**, 1046 (1990).

[7] L. Pavesi, L. Dal Negro, C. Mazzoleni, G. Franzò and F. Priolo, "Optical gain in silicon nanocrystals", *Nature* **408**, 440 (2000).

[8] M. G. Boudreau, S. G. Wallace, G. Balcaitus, S. Murugkar, H. K. Haugen and P. Mascher, "Application of *in situ* ellipsometry in the fabrication of thin-film optical coatings on semiconductors", *Appl. Opt.* **39**, 1053 (2000).

[9] Richard A. Soref, "Silicon-Based Optoelectronics", *Proc. IEEE* **81**, 1687 (1993).

[10] Lorenzo Pavesi and David J. Lockwood, *Silicon Photonics*, Springer-Verlag, New York, NY, 2004.

[11] René M. de Ridder, Kerstin Wörhoff, Afred Driessen, Paul V. Lambeck and Hans Albers, "Silicon Oxynitride Planar Waveguiding Structures for Application in Optical Communication", *IEEE J. Select. Topics Quantum Electron.* **4**, 930 (1998).

[12] Ansheng Liu, Richard Jones, Ling Liao, Dean Samara-Rubio, Doron Rubin, Oded Cohen, Remus Nicolaescu and Mario Paniccia, "A high-speed optical modulator based on a metal-oxide-semiconductor capacitor", *Nature* **427**, 615 (2004).

[13] J. Wojcik, B. J. Robinson, D. A. Thompson and P. Mascher, "Control of dielectric cap induced band-gap shift in 1.55 μm laser structures", *J. Vac. Sci. Technol. A* **20**, 1076 (2002).

[14] Graham T. Reed and Andrew P. Knights, *Silicon Photonics: An Introduction*, John Wiley & Sons, Ltd., Etobicoke, ON., 2004.

[15] T. Roschuk, J. Wojcik and P. Mascher, "Optical and compositional characterization of SiO_xN_y and SiO_x thin films deposited by electron cyclotron resonance plasma enhanced chemical vapor deposition", *J. Vac. Sci. Technol.* **A24**, 883 (2004).

[16] M. Boudreau, "SiO_xN_y Waveguides Deposited by ECR-PECVD", Master's thesis, McMaster University, 1993.

[17] M. Boudreau, "Optical Coatings for Improved Semiconductor Diode Laser Performance", Ph.D thesis, McMaster University, 1997.

[18] M. I. Alayo, D. Criado, M. N. P. Carreño and I Pereyra, "Fabrication of PECVD-silicon oxynitride-based optical waveguides", *Mater. Sci. Eng. B* **112**, 154 (2004).

[19] P. Mascher and J. Wojcik, "Electron Cyclotron Resonance Plasma Enhanced Chemical Vapour Deposition (ECR-PECVD): A Versatile Tool in the Fabrication of Optoelectronic Devices", *Electrochem. Soc. Proc.* **4**, 3–22 (2002).

[20] X. Tan, "Study of the Optical Properties of Silicon Oxynitride Thin Films By Effective Medium Theories", Master's thesis, McMaster University, 2004.

[21] C. Simionescu, "Characterization of Silicon Oxynitride Thin Films Deposited by Electron Cyclotron Resonance Plasma Enhanced Chemical Vapour Deposition", Master's thesis, McMaster University, 2000.

[22] Stephen M. Rossnagel, Jerome J. Cuomo and William D. Westwood, *Handbook of Plasma Processing Technology*, Noyes Publications, Park Ridge, NJ., 1990.

[23] Milton Ohring, *The Materials Science of Thin Films*, Academic Press, Inc., New York, NY, 1992.

[24] M. G. Boudreau, M. Boumerzoug, P. Mascher and P. E. Jessop, "Electron cyclotron resonance chemical vapor deposition of silicon oxynitrides using tri(dimethytlamino)silane", *Appl. Phys. Lett.* **63**, 3014 (1993).

[25] Giovani Bruno, Pio Capezzuto and Arun Madan, *Plasma Deposition of Amorphous Silicon-Based Materials*, Academic Press, San Diego, CA., 1995.

[26] K. K. Schuegraf, *Handbook of Thin-Film Deposition Processes and Techniques*, Tylan Corporation, Carson, CA., 1988.

[27] K. Pangal, J. C. Sturm, S. Wagner and T. H. Büyüklimanli, "Hydrogen plasma enhanced crystallization of hydrogenated amorphous silicon films", *J. Appl. Phys.* **85**, 1900 (1999).

[28] D. Mataras, F. Coutelieris, P. Kounavis and D. E. Rapakoulias, "Dilution-enhanced radical generation in silane glow discharges", *J. Phys. D: Appl. Phys.* **29**, 2452 (1996).

[29] Y. Yamamoto, S. Suganuma, M. Ito, M. Hori and T. Goto, "Effects of Dilution Gases on Si Atoms and SiH_x^+ (x = 0-3) Ions in Electron Cyclotron resonance SiH_4 Plasmas", *Jpn. J. Appl. Phys.* **36**, 4664 (1997).

[30] M. J. Kushner, "Plasma chemistry of $He/O_2/SiH_4$ and $He/N_2O/SiH_4$ mixtures for remote plasma activated chemical-vapor deposition of silicon dioxide", *J. Appl. Phys.* **74**, 6538 (1993).

[31] E. Meeks, R. S. Larmon, P. Ho, C. Apblett, S. M. Han, E. Edelberg and E. S. Aydil, "Modeling of SiO_2 deposition in high density plasma reactors and comparison of model predictions with experimental measurements", *J. Vac. Sci. Technol.* **A16**, 544 (1998).

[32] B. Lewis and J. C. Anderson, *Nucleation and Growth of Thin Films*, Academic Press, Inc., New York, NY, 1978.

[33] B. Lewis and D. S. Campbell, "Nucleation and Initial-Growth Behavior of Thin Film Deposits", *J. Vac. Sci. Technol.* **4**, 209 (1967).

[34] J. A. Venables, G. D. T. Spiller and M. Hanbücken, "Nucleation and growth of thin films", *Rep. Prog. Phys.* **47**, 399 (1984).

[35] E. Irving, "Erbium Doped SiO_xN_y Waveguides Produced by ECR-PECVD", Master's thesis, McMaster University, 2003.

[36] N. Kaiser, "Review of the fundamentals of thin-film growth", *Appl. Opt.* **41**, 3053 (2002).

[37] Ludmila Eckertová, *Physics of Thin Films*, Plenum Press, New York, NY, 1986.

[38] Richard J. Borg and G. J. Dienes, *An Introduction to Solid State Diffusion*, Academic Press, San Diego, CA., 1988.

[39] J. Heitmann, D. Kovalev, M. Schmidt, L. X. Yi, R. Scholz, F. Eichhorn and M. Zacharias, "Synthesis and size control of Si nanocrystals by Si/SiO_2 superlattices and Er doping", *Mat. Res. Soc. Symp. Proc.* **737**, F1.6.1 (2003).

[40] S. O. Kasap, *Principals of Electrical Engineering Materials and Devices: Revised Edition*, Mcgraw Hill, Toronto, ON., 2000.

[41] James R. Chelikowski and Marvin L. Cohen, "Nonlocal pseudopotential calculations for the electronic structure of eleven diamond and zinc-blende semiconductors", *Phys. Rev. B* **14**, 556 (1976).

[42] W. P. Dumke, "Interband Transitions and Maser Action", *Phys. Rev.* **127**, 1559 (1962).

[43] D. E. Aspnes and A. A. Studna, "Dielectric functions and optical parameters of Si, Ge, GaP, GaAs, GaSb, InP, InAs, and InSb from 1.5 to 6.0 eV", *Phys. Rev. B* **27**, 985 (1983).

[44] Edward D. Palik, *Handbook of Optical Constants of Solids*, Academic Press, San Diego, CA., 1985.

[45] N. M. Ravindra and J. Narayan, "Optical properties of amorphous silicon and silicon dioxide", *J. Appl. Phys.* **60**, 1139 (1986).

[46] Gwo-Jen Jan and Ying-Shen Huang, "Optical Properties of Hydrogenated Amorphous Silicon", *Chin. J. Phys.* **24**, 19 (1986).

[47] D. J. Lockwood, "Optical and electronic properties of nanostructured silicon", *Electrochem. Soc. Proc.* **2003-01**, 89 (2003).

[48] Yoshihiko Kanemitsu, "Efficient light emission from crystalline and amorphous silicon nanostructures", *J. Lumen.* **100**, 209 (2002).

[49] M. V. Wolkin, J. Jorne, P. M. Fauchet, G. Allan and C. Delerue, "Electronic States and Luminescence in Porous Silicon Quantum Dots: The Role of Oxygen", *Phys. Rev. Lett.* **82**, 197 (1999).

[50] Zhiyong Zhou, Louis Brus and Richard Freisner, "Electronic Structure and Luminescence of 1.1- and 1.4-nm Silicon Nanocrystals: xide Shell versus Hydrogen Passivation", *Nano Lett.* **3**, 163 (2003).

[51] S. M. Prokes, "Surface and optical properties of porous silicon", *J. Mater. Res.* **11**, 305 (1996).

[52] Xiaochun Wu, Ch. Ossadnik, Ch. Eggs, S. Veprek and F. Phillipp, "Structure and photoluminescence features of nanocrystalline Si/SiO_2 films produced by plasma chemical vapor deposition and post-treatment", *J. Vac. Sci. Technol. B* **20**, 1368 (2002).

[53] A. S. Zyubin, Yu D. Glinka, A. M. Mebel, S. H. Lin, L. P. Hwang and Y. T. Chen, "Red and near-infrared photoluminescence from silica-based nanoscale materials: Experimental investigation and quantum-chemical modeling", *J. Chem. Phys.* **116**, 281 (2002).

[54] Fabio Iacona, Giorgia Franzò and Corrado Spinella, "Correlation between luminescence and structural properties of Si nanocrystals", *J. Appl. Phys.* **87**, 1295 (2000).

[55] Sandeep Kohli, Jeremy A. Theil, Rick D. Snyder, Christopher D. Rithner and Peter K. Dorhout, "Fabrication and characterization of silicon nanocrystals by thermal oxidation of a-Si:H in air", *J. Vac. Sci. Technol. B* **21**, 719 (2003).

[56] Philippe M. Fauchet, "Progress Toward Nanoscale Silicon Light Emitters", *IEEE J. Select. Topics Quantum Electron.* **4**, 1020 (1998).

[57] Stefano Ossicini, Lorenzo Pavesi and Franceso Priolo, *Light Emitting Silicon for Microphotonics*, Springer-Verlag, New York, NY, 2003.

[58] Ozdal Boyraz and Bahram Jalali, "Demonstration of a silicon Raman laser", *Opt. Express* **12**, 5269 (2004).

[59] W. N. Lennard, Surface and Microscopy Analysis, , Department of Physics and Astronomy, University of Western Ontario (2003). Available online at publish.uwo.ca/~wlennard/.

[60] Joseph R. Tesmer and Michael Nastasi, *Handbook of Modern Ion Beam Materials Analysis*, Materials Research Society, Pittsburg, PA., 1995.

[61] Wei-Kan Chu, James W. Mayer and Marc-A. Nicolet, *Backscattering Spectrometry*, Academic Press, New York, NY., 1978.

[62] W. H. Bragg and R. Kleeman, "On the alpha particles of radium and their loss of range in passing through various atoms and molecules", *Philos. Mag.* **10**, 318 (1905).

[63] Leonard C. Feldman and James W. Mayer, *Fundamanetals of Surface and Thin Film Analysis*, Elsevier Science Publishing Co., Inc., New York, NY., 1986.

[64] S. Perkowitz, *Optical Characterization of Semiconductors*, Academic Press, San Diego, CA., 1993.

[65] A. Sassella, A. Borghesi, F. Corni, A. Monelli, G. Ottaviana, R. Tonini, B. Pivac, M. Bacchetta and L. Zanotti, "Infrared study of Si-rich silicon oxide films deposited by plasma-enhanced chemical vapor deposition", *J. Vac. Sci. Technol. A* **15**, 377 (1997).

[66] A. A. Langford, M. L. Fleet, B. P. Nelson, W. A. Lanford and N. Maley, "Infrared absorption strength and hydrogen content of hydrogenated amorphous silicon", *Phys. Rev. B* **45**, 13367 (1992).

[67] J. T. Finch, G. Lucovsky, E. Kobeda and E. A. Irene, "Effects of thermal history on stress-related properties of very thin films of thermally grown silicon dioxide", *J. Vac. Sci. Technol. B* **7**, 153 (1989).

[68] Harland G. Tompkins and William A. McGahan, *Spectroscopic Ellipsometry and Reflectometry: A User's Guide*, John Wiley and Sons, Inc., New York, NY., 1999.

[69] R. M. A. Azzam and N. M. Bashara, *Ellipsometry and Polarized Light*, North Holland Publishing Company, New York, NY., 1977.

[70] Harland G. Tompkins, *A User's Guide to Ellipsometry*, Academic Press, Inc., San Diego, CA., 1993.

[71] J. A. Woollam Co., *Guide to Using WVASE32*, J. A. Woollam Co., Inc., pp. 2.1-2.62, Lincoln, NE., 2001.

[72] Blaine Johs, Jeff Hale, N. J. Ianno, Craig M. Herzinger, Tom Tiwald and John A. Woollam, "Recent Developments in Spectroscopic Ellipsometers for in situ Applications", *Proceedings of SPIE* **4449**, 41 (2001).

[73] John A. Woollam, Blaine Johs, Craig M. Herzinger, James Hilfiker, Ron Synowicki and Corey L. Bungay, "Overview of Variable Angle Spectroscopic Ellisometry (VASE), Part I: Basic Theory and Typical Applications", *Critical Reviews of Optical Science and Technology* **CR72**, 3 (1999).

[74] A. Sassella, P. Lucarno, A. Borghesi, F. Corni, S. Rojas and L. Zanotti, "Silicon oxynitride study by the tetrahedron model and by spectroscopic ellipsometry", *J. Non-Crys. Sol.* **187**, 395 (1995).

[75] Irving P. Herman, *Optical Diagnostics For Thin Film Systems*, Academic Press, San Diego, CA., 1996.

[76] R. A. Stradling and P. C. Klipstein, *Growth and Characterisation of Semiconductors*, Adam Hilger, New York, NY., 1990.

[77] S. O. Kasap, *Optoelectronics and Photonics: Principles and Practices*, Prentice-Hall, Upper Saddle River, NJ., 2001.

[78] R. T. Bate, "Nanoelectronics", *Nanotechnology* **1**, 1 (1990).

[79] Ming-Fu Li, *Modern Semiconductor Quantum Physics*, World Scientific, River Edge, NJ., 1994.

[80] J. Wojcik and P. Mascher, "The Influence of the Deposition Conditions on the Optical and Compositional Characteristics of SiO_x Thin Films Deposited by ECR-PECVD", *Proc. SVC Annual Tech. Con.* **47**, 687 (2004).

[81] D. Amans, S. Callard, A. Gagnaire, J. Joseph, G. Ledoux and F. Huisken, "Ellipsometric study of silicon nanocrystal optical constants", *J. Appl. Phys.* **93**, 4173 (2003).

[82] NIST Atomic Spectra Database 2004, Available online at physics.nist.gov/cgi-bin/AtData/main_asd.

[83] G. Franzò, V. Vinciguerra and F. Priolo, "The excitation mechanism of rare-earth ions in silicon nanocrystals", *Appl. Phys. A* **69**, 3 (1999).